Light-matter coupling utilizes quantum fluctuations of electromagnetic fields of the vacuum to shape and control properties of matter excitations and even the vacuum ground state itself. This thesis explores new regimes of ultrastrong and deep-strong light-matter coupling, presenting record coupling strengths and new schemes for controlling the interaction of light and matter modes, on strongly sub-wavelength scales and simultaneously faster than an oscillation cycle of light. These accomplishments are the result of a novel approach of coupling tailor-cut cyclotron resonances of two-dimensional electron gases hosted in semiconductor quantum wells to subwavelength THz modes of a new generation of plasmonic resonator structures.

First, lateral shaping of the quantum wells tailors the spatial overlap of the vacuum electric field and the polarization field of the matter excitation. This allows us, similar to the selection rules in classical optics, to custom-tailor the overlap between multiple matter and cavity modes. The introduction of off-resonant, multi-mode coupling offers a new quality of the vacuum ground state characterized by polaritons spanning over as much as 6 optical octaves, a vacuum population of 1.17 virtual photons and 1.06 virtual magnetoplasmon excitations, resulting in an equivalent light-matter coupling strength of $\Omega_R/\omega_c = 3.19$. Moreover, we drive an ultrastrongly coupled system with strong, coherent THz waveforms competing with the vacuum electromagnetic field and observe strong, non-perturbative nonlinearities up to eight-wave mixing. These nonlinear polariton correlations beyond the normal-mode approximation set the stage for nonlinear optical control of deep-strong coupling. Finally, we demonstrate a highly non-adiabatic switch-off of deep-strong coupling by selective photodoping of a switching element, collapsing the cavity field quasi-instantaneously and decoupling light and matter on time scales ten times faster than a cycle of light. In combination with the record vacuum photon population, this paves the way for the detection of vacuum radiation in a table-top experiment, in similarity to Unruh-Hawking radiation from black holes.

Universität Regensburg
Institut für Experimentelle und Angewandte Physik
Lehrstuhl Prof. Dr. Rupert Huber

Joshua Mornhinweg
TAILORING AND NON-ADIABATIC CONTROL OF DEEP-STRONG LIGHT-MATTER COUPLING

TAILORING AND NON-ADIABATIC CONTROL OF DEEP-STRONG LIGHT-MATTER COUPLING

Joshua Mornhinweg

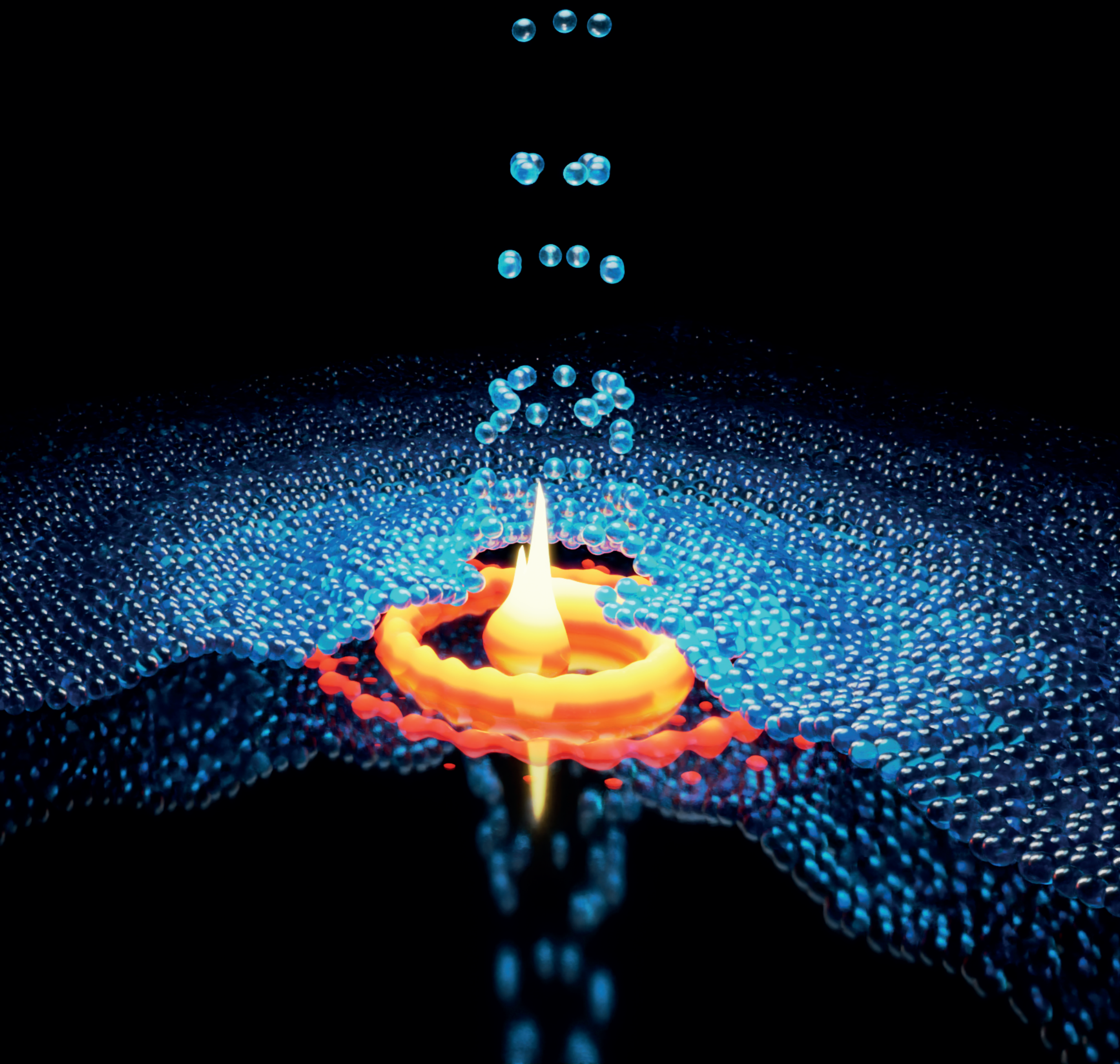

Tailoring and Non-Adiabatic Control of Deep-Strong Light-Matter Coupling

Dissertation
zur Erlangung des Doktorgrades der Naturwissenschaften
(Dr. rer. nat.)
der Fakultät für Physik der Universität Regensburg

vorgelegt von
Joshua Mornhinweg
aus Freiburg im Breisgau
im Jahr 2023

Das Promotionsgesuch wurde eingereicht am: 30.06.2023.

Die Arbeit wurde angeleitet von: Prof. Dr. Rupert Huber.

Prüfungsausschuss:	Vorsitzender:	Prof. Dr. Jaroslav Fabian
	1. Gutachter:	Prof. Dr. Rupert Huber
	2. Gutachter:	Prof. Dr. Christoph Lange
	weiterer Prüfer:	Prof. Dr. Christian Schüller

Contents

Chapter 1

Introduction

> *Success is not the key to happiness.*
> *Happiness is the key to success.*
> *If you love what you are doing, you will be successful.*
>
> — Albert Schweitzer

What is vacuum? This question about the nature of absolute nothingness has been asked again and again over the course of the history of science - with very different answers. Going back in time, Isaac Newton [New18] (and many others) postulated an aether, that surrounds everything, is everywhere, and allows light to travel through space. However, this idea could not be proven even with very sophisticated measurements, such as the Michelson-Morley interferometer [Mic81]. Albert Einstein's theory of special relativity then assumed the vacuum as a completely empty space, where no supporting medium for electromagnetic waves is necessary. In 1916, he described spontaneous emission as one of the three processes that can occur when light and matter are interacting [Ein16]. Building on the work of Dirac [Dir27], and expanding Einstein's work by introducing the concept of second quantization, modern quantum dynamics no longer considers the vacuum as empty and can explain the process of spontaneous emission as stimulated emission by vacuum fluctuations. In fact, a finite ground state energy accompanied by the presence of vacuum fluctuations exists in every system [Dys49, Pes95].

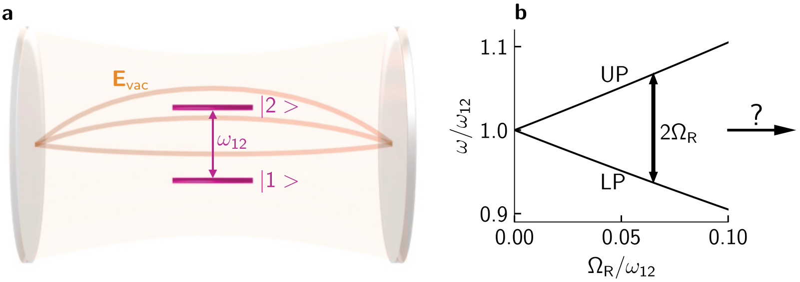

Figure 1.1 | Light-matter coupling. **a**, Illustration of the vacuum field $\mathbf{E}_{\mathrm{vac}}$ of a cavity, coupled to an atomic transition with a frequency of ω_{12}. **b**, Splitting of the lower polariton (LP) and the upper polariton (UP) by $2\Omega_{\mathrm{R}}$ with increasing coupling strength $\Omega_{\mathrm{R}}/\omega_{12}$.

The intriguing fact, that matter can actually interact with this "nothingness", that the quantum vacuum is, has opened up the possibility to modify and tailor this interaction, sprouting the field of *cavity quantum electrodynamics* (cavity-QED). The first example of such a modification of matter properties with vacuum fields is the Purcell effect [Pur46]. Purcell predicted that the rate of spontaneous emission for an atom can be enhanced (or suppressed) by placing it in a resonant cavity (Fig. 1.1**a**). Doing so, the atomic system with a transition frequency of ω_{12} and the cavity vacuum field $\mathbf{E}_{\mathrm{vac}}$ start to exchange energy. When reducing the cavity and the atom loss rates, eventually, the energy exchange rate, called the vacuum Rabi frequency Ω_{R}, exceeds the losses and we enter the regime of strong coupling (SC). In this regime, first observed by Kaluzny et al. [Kal83], the periodic exchange of energy between the vacuum field and the matter system occurs at the frequency Ω_{R}, with

$$\Omega_{\mathrm{R}} \propto \mathbf{d} \times \mathbf{E}_{\mathrm{vac}} \times \sqrt{N}, \tag{1.1}$$

where $\mathbf{d}$ is the dipole moment of the atomic transition (or any other resonance that can be coupled to) and N is the number of equivalent atoms inside the cavity. The coupling results in the formation of new eigenstates of the system, light-matter hybridized states called polaritons (Fig. 1.1**b**). These new eigenstates, the lower (LP) and upper polariton (UP), are separated in frequency by $2\Omega_{\mathrm{R}}$. The strength of the interaction is quantified by the normalized light-matter coupling strength $\eta = \Omega_{\mathrm{R}}/\omega_{12}$, defined as the quotient of the vacuum Rabi frequency and the unperturbed frequency of the coupled matter system at resonance. Coupling to single atoms severely limits the achievable coupling strength as intrinsic atomic dipole moments are very small and the transition frequencies are comparatively high. To reach higher coupling strengths, one has three options (see Equation 1.1): use collective excitations to massively increase N, reduce the cavity mode volume to boost $\mathbf{E}_{\mathrm{vac}}$ or choose other excitations with large dipole moments $\mathbf{d}$. Following this strategy, one can reach the regime of ultrastrong coupling (USC), where Ω_{R} reaches the order of magnitude of ω_{12} [Ana09, Gü09]. Here, the extremely strong coupling profoundly alters the vacuum ground state, giving rise to an intriguing and exotic vacuum ground state characterized by a population of virtual excitations of both light and matter systems. These virtual excitations are called “virtual” because, under usual circumstances, the vacuum ground state and its fluctuations cannot emit radiation.

This fundamental coupling-induced change of the properties of the quantum vacuum [Ciu05, FK19, FD19] is at the centre of a multitude of fascinating and groundbreaking phenomena, such as Bose Einstein condensation of exciton-polaritons in solids [Den10], vacuum-modified transport [Org15, Bar18, PB19, Val21, App22], the vacuum Bloch-Siegert shift [Li18], light-matter decoupling [DL14], nonlinear optics with virtual photons [Koc17], novel light sources [Gar17], single-photon manipulation [Rid12], irregular photon transfer [Fel14], squeezed quantum states of light [Fed16], creation of photon-bound excitons [Cor21], coherent polariton scattering [Kno22], superradiant [Hep73, Wan73] or other phase transitions [Sch19]. This ability to change the vacuum ground state even started the field of cavity chemistry [Hut12, Chi16, Her16, Tho19, Dun22, Sch22]. As the number of virtual excitations scales with the coupling strength, the stronger the coupling, the more pronounced the effect. When Ω_{R} surpasses the eigenfrequencies of the light and matter systems, they exchange one energy quantum faster than one oscillation cycle of the light mode and the deep-strong coupling regime (DSC) is reached. As of now, this regime has only been achieved with a few select material systems: superconducting qubit-oscillator circuits with GHz frequencies [Yos17], followed by Landau polariton systems in the terahertz (THz) regime [Bay17] and plasmonic nanoparticle crystals [Mue20].

While vacuum fluctuations are ubiquitous in quantum mechanics and indirectly manifest in various effects such as the Casimir effect [Cas48] and the Lamb-shift [Lam47], so far, they have not been measured directly. Recently efforts using electro-optic sampling in a nonlinear crystal to measure vacuum noise and correlations of the vacuum [Rie15, BC19] have been made. Hawking [Haw74, Haw75] and Unruh [Unr76] postulated a mechanism at the event horizon of black holes that leads to a photon flux coming from a black hole, as the strong space-time gradient at the event horizon can generate real photons from vacuum fluctuations. Measuring these photons is however illusive due to practical reasons, e.g. travelling to the vicinity of a black hole and the small photon flux. However, a non-adiabatic change of the vacuum ground state of an ultrastrongly or deep-strongly coupled system has been demonstrated [Gü09, Hal20] and is postulated to convert virtual photons to real ones [Lib07, Gü09, Gar13, Hal20], very similarly to the mechanism considered by Hawking and Unruh and the dynamical Casimir effect [Moo70, Lam96, Wil11].

Measuring such a virtual photon emission from an extremely strongly light-matter coupled system poses multiple challenges towards the system of choice and the measurement itself. As a prerequisite, one needs a system with the largest possible number of virtual photons in the ground state to maximize the number of radiated photons. Additionally, one requires a way to modulate the coupling strength with sufficient contrast [DL17] and on a timescale of less than one cycle of the light-matter energy exchange, i.e., non-adiabatically. Lastly, to detect the emission, it is necessary to be able to detect single photons in the respective wavelength range. On a more general note, such a subcycle control mechanism of the coupling also opens up new possibilities for controlling all the aforementioned effects made possible by coupling to vacuum fluctuations, such as the capability to modify transport, manipulate chemical reactions, and induce phase transitions.

In this work, I showcase a series of breakthroughs that not only pave the way for measuring virtual photon emission, but also unveil multiple innovative techniques for shaping and controlling ultrastrong and deep-strong light-matter coupling on nanoscale length- and subcycle (sub-one-oscillation-cycle-of-light) timescales — achieving a new level of precision and control. Chapter 2 gives an introduction to the theory description of deep-strong light-matter coupling, a detailed look into the vacuum ground state and the system of choice to implement deep-strong coupling: cyclotron resonances of two-dimensional electron gases in quantum well stacks coupled to planar metasurface resonator arrays. In chapter 3, I show how one can combine the regimes of light-matter coupling, governed by the vacuum Rabi frequency, with strong-field physics, governed by the Rabi frequency of a coherent classical field, both driving the system simultaneously. This ultrafast control mechanism induces nonlinearities breaking the normal-mode approximation and lets the polaritons, our new eigenstates, interact with each other to create custom-tailored nonlinearities. In chapter 4, an additional degree of freedom for shaping the light-matter coupling is explored - structuring not only the metasurface array, but also the quantum well plane. This method offers precise control over the modal overlap and the possibility to explore the multi-mode coupling regime for multiple cavity modes. Chapter 5 capitalizes on to the concept of multi-mode coupling by introducing multiple matter modes, magneto-plasmons, to establish a new coupling and virtual photon population record, achieving, for the first time, an expectation value of over one whole-photon in the vacuum ground state. In chapter 6, I present a novel and minimally invasive mechanism to switch-off a deep-strongly coupled system on strongly subcycle time scales. Together with the increased number of virtual photons shown in chapter 5 and further developed optimizations, this mechanism paves the way for the detection of virtual photon emission. Chapter 7 concludes this thesis with exciting outlooks for the novel possibilities to control and shape vacuum photon mediated effects, ranging from cavity chemistry to quantum information processing.

Chapter 2

Deep-strong light-matter coupling

Light-matter coupling can be observed in a multitude of systems, ranging from single atoms to organic molecules and semiconductor structures, as long as the transition features a dipole moment **d** that the vacuum field, enhanced by a cavity, can couple to. The strength of the interaction is characterized by the normalized coupling strength, $\eta = \Omega_\mathrm{R}/\omega_{12}$, the quotient of the vacuum Rabi frequency, Ω_R, and the frequency of the matter transition, ω_{12}.

When Ω_R is greater than the loss rates of the cavity and matter systems, γ_cav and γ_mat, strong coupling (SC) is achieved (figure 2.1). Here, a coherent energy exchange between light and matter modes takes place and as a result, polaritons as the new light-matter hybrid eigenstates form. This dynamic can be described with a basis rotation in the rotating-wave approximation (RWA). With $\eta > 0.1$, ultrastrong coupling (USC) is reached. Here, the counter-rotating terms and their faster dynamics no longer contribute only weakly to the overall dynamics. Thus, they can no longer be neglected, and the RWA breaks down. These counter-rotating terms, such as $\hat{a}\hat{b}$

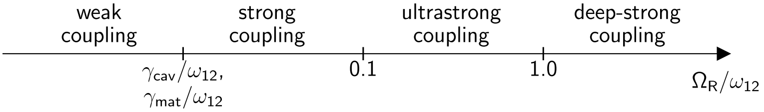

Figure 2.1 | Regimes of light-matter coupling: weak coupling, $\Omega_\mathrm{R}/\omega_{12} > \gamma_\mathrm{cav}/\omega_{12}, \gamma_\mathrm{mat}/\omega_{12}$: strong coupling, > 0.1: ultrastrong coupling, > 1.0: deep-strong coupling.

or $\hat{a}^\dagger \hat{b}^\dagger$ in second quantization, no longer preserve the number of excitations and are responsible for the creation of the characteristic vacuum ground state population. When the coupling strength surpasses one, $\eta > 1$, deep-strong coupling (DSC) is reached. Here, for DSC, the important prerequisite for strong coupling, that the loss rates of both systems are smaller than the vacuum Rabi frequency Ω_R, becomes more and more irrelevant [DL17, FK19], as even over-damped coupled resonances ($\gamma_\mathrm{cav} > \omega_\mathrm{cav}$ or $\gamma_\mathrm{mat} > \omega_{12}$) are able to fulfil the condition $\Omega_\mathrm{R} > \gamma_\mathrm{cav}, \gamma_\mathrm{mat}$.
To accurately describe the wealth of different light-matter coupled systems, several tailored theories are available. Strongly coupled systems with one atomic transition can be described using the *Jaynes-Cummings model* [Jay63] or including non-resonant contributions for USC with the *quantum Rabi model* [Rab37]. These models can be expanded to multi-atom systems with the *Tavis-Cummings model* [Tav68] and the *Dicke model* [Dic54]. These fermion-boson Rabi models can be further generalized to a purely bosonic model, called the *Hopfield model* [Hop58], to describe the coupling to collective excitations such as the cyclotron resonance, or plasmons. Models describing the transition from the fermionic Rabi model to the bosonic Hopfield model have also been developed [Tod14].
Sometimes the additional regimes of very-strong-coupling (VSC) and multi-mode strong-coupling (MMSC) are used to further classify the coupling. VSC is reached, when Ω_R is on the order of the spacing of the levels in the matter system [Bro17, Raj21], while MMSC is reached when Ω_R is comparable to the spacing of the resonator modes [Sun15, Cor21, Bal21]. While SC, USC and DSC are usually studied in the context of light-matter coupling, (ultra-)strong coupling can also be present between other systems, e.g. magnons [Bas21, Mak21]. In the following, our focus centres on the Hopfield model, as our objective is to achieve DSC, wherein the employed cyclotron resonance represents a bosonic, multi-particle excitation. In chapters 4 and 5, we will extend this model to encompass the VSC and MMSC regimes as well.

2.1. Theory of bosonic light-matter coupling

To describe the coupling of a single (bosonic) cavity mode to another bosonic mode (see Fig. 2.2), such as the collective cyclotron resonance of a two-dimensional electron gas, we use Hopfield's model [Hop58, Ciu05, Hag10, Cor23] in second quantization.

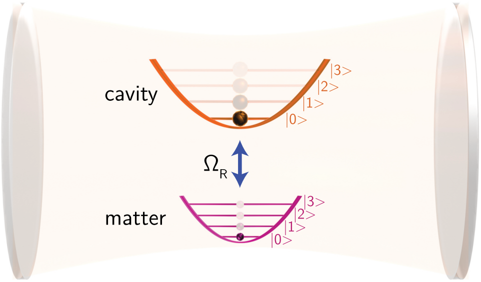

Figure 2.2 | Bosonic ultrastrong coupling. Illustration of resonant ultrastrong coupling of a single cavity mode (upper parabola) to a single matter excitation (bottom parabola) with a vacuum Rabi frequency Ω_{R}. The population by virtual excitations in the vacuum ground state is indicated by semi-transparent spheres. Adapted from [Mor23a].

Let us consider the Hamiltonian describing a two-dimensional electron gas (2DEG) of N electrons of charge $-e$ and effective mass m^* interacting with a photonic field of a resonator in the Coulomb gauge,

$$\hat{H} = \hat{H}_{\mathrm{EM}} + \sum_{j=1}^{N} \frac{\left(\hat{\mathbf{p}}_j + e\hat{\mathbf{A}}\left(\mathbf{r}_j\right)\right)^2}{2m^*} + V(\mathbf{r}), \tag{2.1}$$

expressed in terms of the electric and magnetic field vectors $\hat{\mathbf{E}}(\mathbf{r})$ and $\hat{\mathbf{B}}(\mathbf{r})$ (contained in the electromagnetic field Hamiltonian $\hat{H}_{\mathrm{EM}}$, see appendix E), the potential vector $\hat{\mathbf{A}}(\mathbf{r})$ and the Coulomb potential $V(\mathbf{r})$. Here we employed the minimal coupling substitution ($\hat{\mathbf{p}} \rightarrow \hat{\mathbf{p}} + e\hat{\mathbf{A}}$).

Omitting the possibility of multiple cavity modes and multiple matter modes as well as assuming perfectly bosonic modes, we can simplify the Hamiltonian. The full derivation is featured in appendix E. Models including multiple modes will be discussed in chapter 4 and 5. After multiple rearrangement steps, the Hamiltonian reads:

$$\hat{H} = \hat{H}_{\mathrm{cav}} + \hat{H}_{\mathrm{c}} + \hat{H}_{\mathrm{int}} + \hat{H}_{\mathrm{dia}}. \tag{2.2}$$

Here, the light field of the cavity is described in second quantization with the creation and annihilation operators $\hat{a}^\dagger$ and $\hat{a}$ and a frequency ω_{cav}:

$$\hat{H}_{\mathrm{cav}} = \hbar\omega_{\mathrm{cav}}\left(\hat{a}^\dagger\hat{a} + \frac{1}{2}\right). \tag{2.3}$$

The collective cyclotron resonance of the electrons is described in second quantization with the creation and annihilation operators, $\hat{b}^\dagger$ and $\hat{b}$, and a frequency ω_{c}, and originates from the interaction with the applied static external magnetic field, included in the potential vector $\hat{\mathbf{A}}(\mathbf{r})$:

$$\hat{H}_{\mathrm{c}} = \hbar\omega_{\mathrm{c}}\left(\hat{b}^\dagger\hat{b} + \frac{1}{2}\right). \tag{2.4}$$

The minimal coupling is also responsible for two more terms, the interaction Hamiltonian $\hat{H}_{\mathrm{int}}$ and the so-called self-interaction or diamagnetic term $\hat{H}_{\mathrm{dia}}$, denoted by

$$\hat{H}_{\mathrm{int}} = \hbar\Omega_{\mathrm{R}}\left(\hat{a}^\dagger + \hat{a}\right)\left(\hat{b}^\dagger + \hat{b}\right), \tag{2.5}$$

$$\hat{H}_{\mathrm{dia}} = \frac{\hbar\Omega_{\mathrm{R}}^2}{\omega_{\mathrm{c}}}\left(\hat{a}^\dagger + \hat{a}\right)^2. \tag{2.6}$$

$\hat{H}_{\mathrm{dia}}$ describes a cavity frequency blue shift and originates from squaring $\hat{\mathbf{A}}(\mathbf{r})$ in the minimal substitution. The vacuum Rabi frequency Ω_{R}, describing the strength of the interaction, contains the overlap of the light and matter modes, the dipole moment and the number of electrons N. $\hat{H}_{\mathrm{int}}$ includes anti-resonant interactions, beyond the RWA, not included in the Jaynes-Cummings model and the Tavis-Cummings model. These terms, $\hat{a}^\dagger\hat{b}^\dagger$ or $\hat{a}\hat{b}$ seem to violate energy conservation and are responsible for the modified vacuum ground state and the population of virtual photons.

A Bogoliubov transformation diagonalizes $\hat{H}$ in the new polariton basis of the lower (LP) and upper polariton (UP),

$$\hat{H} = E_{\mathrm{G}} + \sum_{\beta\in\{\mathrm{LP},\mathrm{UP}\}} \hbar\omega_\beta \hat{p}_\beta^\dagger \hat{p}_\beta, \tag{2.7}$$

where E_{G} is the ground state energy and p_β is the annihilation operator of a polariton,

$$\hat{p}_\beta = x_\beta \hat{a} + w_\beta \hat{b} + y_\beta \hat{a}^\dagger + z_\beta \hat{b}^\dagger, \tag{2.8}$$

with $|x_\beta|^2 + |w_\beta|^2 - |y_\beta|^2 - |z_\beta|^2 = 1$. The vectors $v_\beta = (x_\beta, w_\beta, y_\beta, z_\beta)^T$ are the eigenvectors for the Hopfield-matrix M, representing the Hamiltonian $\hat{H}$, such that $Mv_\beta = \omega_\beta v_\beta$:

$$M = \begin{pmatrix} \omega_{\mathrm{cav}} + 2D & \Omega_{\mathrm{R}} & 2D & \Omega_{\mathrm{R}} \\ \Omega_{\mathrm{R}} & \omega_{\mathrm{c}} & \Omega_{\mathrm{R}} & 0 \\ -2D & -\Omega_{\mathrm{R}} & -\omega_{\mathrm{cav}} - 2D & -\Omega_{\mathrm{R}} \\ -\Omega_{\mathrm{R}} & 0 & -\Omega_{\mathrm{R}} & -\omega_{\mathrm{c}} \end{pmatrix}, \tag{2.9}$$

with $D = \frac{\hbar\Omega_{\mathrm{R}}^2}{\omega_{\mathrm{c}}}$. For strong coupling, $\frac{\Omega_{\mathrm{R}}}{\omega_{\mathrm{c}}} \ll 1$, the polariton operator can be approximated in the RWA as

$$\hat{p}_\beta = x_\beta \hat{a} + w_\beta \hat{b}. \tag{2.10}$$

In the case of resonance ($\omega_{\mathrm{cav}} = \omega_{\mathrm{c}}$) and strong coupling, the polariton frequencies are given by

$$\omega_{\mathrm{LP(UP)}} \approx \omega_{\mathrm{c}} \mp \Omega_{\mathrm{R}} \tag{2.11}$$

and thus, the two polaritons are separated in frequency by $2\Omega_{\mathrm{R}}$. For USC or DSC, the diamagnetic shift must be included:

$$\omega_{\mathrm{LP(UP)}} = \sqrt{\omega_{\mathrm{c}}^2 + (\Omega_{\mathrm{R}})^2} \mp \Omega_{\mathrm{R}}. \tag{2.12}$$

The diamagnetic shift inhibits the lower polariton from reaching zero and as such, the polaritons split in frequency asymmetrically (Fig. 2.3**a**). When sweeping the resonance condition $\omega_{\mathrm{c}}/\omega_{\mathrm{cav}}$ (Fig. 2.3**b**), regardless of coupling strength, the lower polariton always starts at a frequency of $\omega/ = 0$ for $\omega_{\mathrm{c}} = 0$. Due to the diamagnetic shift, the upper polariton starts at a finite frequency above the bare cavity frequency ω_{cav}, depending on the coupling strength. With increasing ω_{c}, the LP increases in

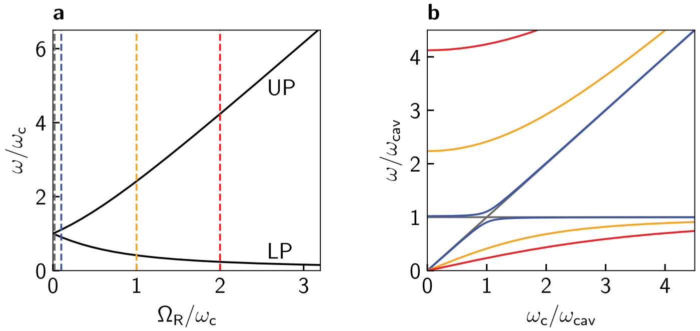

Figure 2.3 | Polariton splitting of bosonic ultrastrong coupling. a, Splitting of the lower polariton (LP) and the upper polariton (UP) with increasing coupling strength Ω_R/ω_c. **b**, Polariton frequencies as a function of ω_c/ω_{cav} for three different coupling strengths: no coupling (grey), $\Omega_R/\omega_c = 0.1$ (blue), $\Omega_R/\omega_c = 1$ (yellow) and $\Omega_R/\omega_c = 2$ (red).

frequency and asymptotically approaches the bare cavity frequency. The UP curves upwards in frequency and asymptotically approaches the cyclotron frequency ω_c. If the LP could reach zero or negative frequencies, a superradiant phase transition, also called the Dicke phase transition, may take place. Whether such transition can take place when the diamagnetic term is absent, was and still is an ongoing debate [Hep73, Wan73, Rza75, BB79, Bak13] and depends on the specific details of the coupled systems. For the coupling to the cyclotron resonance of electrons in QWs with a parabolic dispersion, as considered in this thesis, the diamagnetic terms are present, preventing the Dicke phase transition from occurring.

2.2. Vacuum ground state properties

With the strong light-matter interaction of ultrastrong and deep-strong coupling, the anti-resonant interaction terms in the Hamiltonian become relevant and eventually dominate with increasing coupling strength. This results in a strongly modified vacuum ground state. The quantum vacuum state $|G_0\rangle$ is the quantum state with the lowest possible energy, given by $\hat{a}\,|G_0\rangle = \hat{b}\,|G_0\rangle = 0$ for our uncoupled systems.

For ultrastrong coupling, the ground state $|G_0\rangle$ of the uncoupled system no longer fulfils $\hat{a}\,|G_0\rangle = \hat{b}\,|G_0\rangle = 0$. Its unusual properties and the resulting consequences will be discussed in the following.

The most prevalent change of the vacuum ground state is its finite number of virtual excitations. We calculate the virtual photon number in the system as $\left\langle G \left| \hat{a}^\dagger \hat{a} \right| G \right\rangle$, where the new ground state, dressed by the light-matter interaction, is defined as $\hat{p}_\beta |G\rangle = 0$. By introducing the inverse Bogoliubov transformation,

$$\hat{a} = \sum_{\beta \in \{\mathrm{LP},\mathrm{UP}\}} \left(x^*_\beta \hat{p}_\beta - y_\beta \hat{p}^\dagger_\beta \right), \tag{2.13}$$

and by calculating the expectation value in the ground state we obtain

$$\begin{aligned} N_P = \left\langle G \left| \hat{a}^\dagger \hat{a} \right| G \right\rangle &= \sum_\beta \sum_{\beta'} \left(x_\beta \hat{p}^\dagger_\beta - y^*_\beta \hat{p}_\beta \right) \left(x^*_{\beta'} \hat{p}_{\beta'} - y_{\beta'} \hat{p}^\dagger_{\beta'} \right) \\ &= |y_{\mathrm{LP}}|^2 + |y_{\mathrm{UP}}|^2 . \end{aligned} \tag{2.14}$$

This number of virtual photons in the ground state N_P is displayed in Figure 2.4**a** as a function of the coupling strength. While for low coupling strength the number of photons scales quadratically, in the deep-strong coupling regime N_P scales linearly with the coupling strength.

As a result of the virtual population, the vacuum ground state gets significantly modified. To further explore the properties of this exotic vacuum, we perform calculations with the “quantum toolbox in Python” (QuTiP) [Joh13]. Here we approximate the bosonic harmonic oscillator systems with 30 levels in order to be able to numerically calculate the number state distribution. The calculations reveal that the vacuum ground state features a non-classical Fock state occupation distribution (Fig. 2.4**b**). More precisely, the occupation probability does not diminish monotonically as a function of the photon number for the example of deep-strong coupling with $\eta = \Omega_\mathrm{R}/\omega_\mathrm{c} = 3.0$. Instead, it displays a higher probability for the two-photon state $|2\rangle$ as compared to the single photon state $|1\rangle$. The Wigner function representation for the photonic state, as a function of the complex phase space parameter α, is displayed in Figure 2.4**c-e** for three varying coupling strength. With no coupling, $\Omega_\mathrm{R}/\omega_\mathrm{c} = 0$, (Fig. 2.4**c**), the Wigner function is a (rotational symmetric)

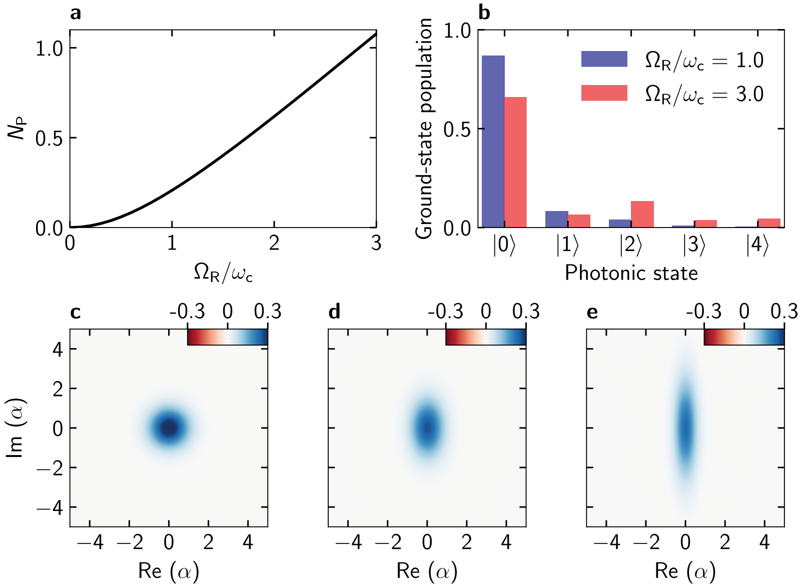

Figure 2.4 | Squeezed vacuum ground state of an ultrastrongly coupled system. a, Mean ground state population of virtual photons N_P as a function of the coupling strength $\Omega_\mathrm{R}/\omega_\mathrm{c}$. **b**, Virtual photon population with $\Omega_\mathrm{R}/\omega_\mathrm{c} = 1$ (blue) and $\Omega_\mathrm{R}/\omega_\mathrm{c} = 3$ (red). **c-e**, Wigner function representation for the photonic state for **c**, $\Omega_\mathrm{R}/\omega_\mathrm{c} = 0$, **d**, $\Omega_\mathrm{R}/\omega_\mathrm{c} = 1$ and **e**, $\Omega_\mathrm{R}/\omega_\mathrm{c} = 3$. Adapted from [Mor23a].

Gaussian function. For a coupled system (Fig. 2.4**d,e**), the Wigner function is compressed in one direction, displaying strong squeezing of the vacuum ground state. The same calculations can be made for the matter part of the coupled system, achieving identical results, as long as a bosonic system is considered. This exotic ground state with its virtual populations is at the core of the many achievements and applications of USC and DSC. Therefore, in these regimes the number of virtual excitations in the ground state provides a more suitable measure for characterising the strength of the coupling, compared to the typically used normalized coupling strength. To further advance the field of USC and DSC, it is critical to increase the virtual excitation numbers to enhance their effects. In chapter 5, we will explore record-breaking, extreme coupling with more than one virtual photon in the vacuum ground state and the corresponding exotic ground state properties. Yet, it is equally important to gain control of the coupling mechanism in space and time, to tailor its region of effect and to be able to switch the coupling on and off on demand.

2.3. Ultrafast 2D THz-magneto-spectroscopy

In order to measure the data presented in this thesis, we use a custom-tailored, ultrafast 2D THz-magneto-spectroscopy setup. Here we employ phase-stable, broadband, single-cycle THz pulses to measure the linear and nonlinear response of our samples in the THz regime. We record the transmitted THz waveform with electro-optic sampling [Wu95, Nah96, Lei99], which allows us to trace the electric field profile $\mathcal{E}(t)$ of the THz pulses with subcycle precision and extract the spectral amplitude and phase via a Fourier transform. Electro-optic sampling also enables us to measure subcycle resolved time dynamics when exciting the samples with strong THz fields or optical pumping. At the same time, we can cool the sample to cryogenic temperatures and apply an external magnetic field bias with a custom magnet-cryostat. The schematic layout of the setup is detailed in Figure 2.5.

We start with femtosecond near-infrared pulses (centre wavelength, 807 nm, pulse energy, 5.5 mJ, pulse duration, 33 fs) from a titanium-sapphire (Ti:Sa) amplifier laser operating at a repetition rate of 3 kHz. The pulses are split by a beam splitter (BS1) into two branches, where the first either drives an optical parametric amplifier (OPA) or a tilted pulse front (TPF) THz source [Ste03, Bai17].

The second pulse is used to generate broadband, single-cycle THz pulses by optical rectification and to detect the transmitted waveforms by electro-optic sampling. For THz generation, we employ an ⟨110⟩-cut ZnTe crystal with a thickness of 1 mm (C1), whereas for detection of the transmitted THz we use a 0.5 mm ZnTe crystal (C2). To increase the bandwidth for measurements in chapter 5, we exchange both crystals to GaP crystals of a thickness of 200 µm. Remaining pump light is separated from the THz pulses by a silicon wafer (W1). Here a mechanical chopper (CH) modulates the THz pulses, allowing for differential detection of the transmitted THz electric field, $\mathcal{E}(t)$. For electro-optic sampling, the gate beam is sent across a delay line (DS2), before being focused by a lens L1 into the electro-optic sampling detection

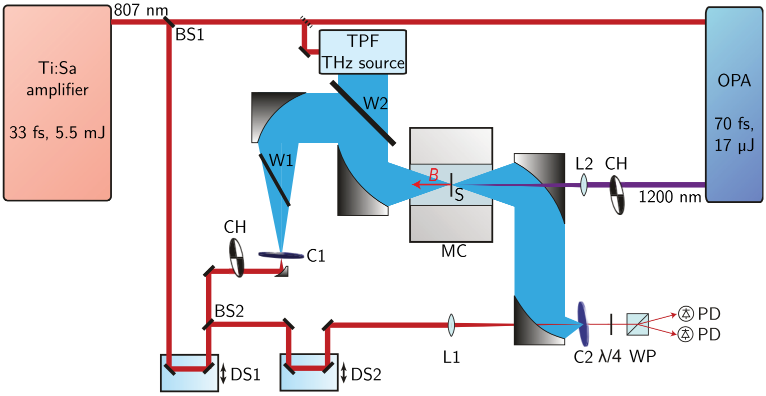

Figure 2.5 | Ultrafast 2D THz-magneto-spectroscopy setup. For a detailed description see the text of chapter 2.3.

crystal (C2). Subsequently, the polarization state of the gate pulses is analysed by a $\lambda/4$-plate, a Wollaston prism (WP), and two balanced photodiodes (PD). The sample (S) is kept at a temperature of $<10\,\mathrm{K}$ in a magneto-cryostat (MC) with a large numerical aperture, with magnetic bias fields (B) of up to $5.5\,\mathrm{T}$ applied perpendicularly to the sample surface. The THz pulses are focused through the sample before the transmitted waveforms are re-collimated and focused onto the detector crystal using off-axis parabolic mirrors. The measurements are referenced to a measurement without a sample in the cryostat to obtain the transmission spectra.

The first branch of the Ti:Sa laser pulses is used to drive THz generation by optical rectification in lithium niobate in a tilted-pulse-front scheme [Ste03, Bai17]. This source can produce THz pulses with up to $1\,\mathrm{MV/cm}$ peak field strength and is introduced into the setup by a Si-beam splitter (W2). These high-field THz pules are used in chapter 3. A second delay line (DS1) changes the time delay t_D between both THz pulses. This experimental configuration for two-dimensional THz spectroscopy provides the capability to simultaneously excite and examine the nonlinear response of multiple resonances, capitalizing on the ultrabroadband frequency spectrum of the THz pulses. A mechanical chopper in each THz generation branch enables the simultaneous recording of both, the linear and nonlinear response of the samples.

For the measurements in chapter 6, the first branch is sent into an optical parametric amplifier (OPA), which generates near-infrared pulses of a duration of 70 fs (FWHM) and a centre photon energy of 1.03 eV. The pulses are modulated by a mechanical chopper (CH) and focused with the lens L2 onto the sample with a spot diameter of 4 mm (FWHM), for homogeneous excitation. This grants us the ability to perform near-infrared pump, THz probe experiments and record both absolute and differential transmission data, with subcycle time resolution.

2.4. Cyclotron resonance of 2D electron gases in quantum wells

So far, only three matter systems have been able to achieve deep-strong coupling: superconducting qubit-oscillator circuits in the GHz range with $\eta = 1.34$ [Yos17], Landau polariton systems with $\eta = 1.43$ [Bay17, Hal20], and plasmonic nanoparticle crystals ($\eta = 1.83$) [Mue20] in the optical regime. To achieve DSC, the utilization of collective excitations proves to be highly advantageous, as the vacuum Rabi frequency Ω_{R} scales with $\sqrt{N}$, where N represents the number of oscillators. This fact renders collective solid-state excitations ideal candidates. Notably, both intersubband transitions [Ana09, Gü09, Tod10] and the cyclotron resonance (CR) of a two-dimensional electron gas (2DEG) [Sca12, Mai14, Bay17, Hal20, Mor21, Mor23a] are well-established systems that facilitate the scaling of the dipole moment with the number of electrons. In this work, we will use Landau polaritons. They feature a greater dipole moment per excitation, and their resonance frequency can be tuned across a wide range through the application of an external magnetic field. In fact, as will be demonstrated in chapter 4, this allows us to achieve the highest coupling strength so far and exceed previous records by almost a factor of two.

To attain a collective cyclotron resonance involving a substantial number of charge carriers, a meticulous design of the platform hosting the two-dimensional electron gas (2DEG) is essential. In this context, semiconductor heterostructures provide precise tailoring capabilities for shaping the energy dispersion of the electrons. A high charge carrier mobility is crucial for the formation of a cyclotron resonance. However, introducing an excessive number of carriers can lead to reduced mobility, which naturally imposes limits on the number of carriers available for potential coupling. Striking the right balance between charge carrier concentration and mobility is pivotal for achieving maximal coupling strengths. In addition, when using quantum wells (QWs) to host the 2DEG, excessive doping also introduces carriers in the second or even higher subbands, which feature different effective masses and do not contribute to a single collective excitation.

We host our 2DEG in GaAs QWs embedded in $\mathrm{Al_{0.3}Ga_{0.7}As}$ barriers. The heterostructures are grown by molecular-beam epitaxy on undoped (100)-oriented GaAs substrates. First these are primed with an GaAs layer of a thickness of 50 nm and a subsequent $\mathrm{Al_{0.3}Ga_{0.7}A}$/GaAs superlattice to achieve a defect-free, atomically flat surface. In order to limit scattering in the QW itself and therefore improve the maximum tolerable doping density, free charge carriers are introduced by symmetrical Si δ-doping in the AlGaAs barriers around the QWs. These carriers then diffuse into the QW. To further overcome the limitation of maximum doping in one QW, we employ a stack of multiple, tightly packed QWs. The QW stack is capped by a protective layer of GaAs with a thickness of 30 nm. Regarding the coupling to a resonator, the multiple 2DEGs effectively still act as one collective system, as long as electronic coupling between QWs can be neglected [Hag10]. The design and fabrication of these QWs has undergone multiple extensive optimizations, including explorations of different semiconductors, to achieve the maximal number of carriers while keeping an acceptable carrier mobility and reducing the thickness of barrier and QW layers [Bay17, Hal21]. The optimized QW structures used in this thesis are grown by the group of Prof. Dominique Bougeard. Unless stated otherwise, the GaAs QWs feature a thickness of 15 nm, each surrounded by barriers of 15 nm, containing the Si δ-doping, targeting a doping density of $\rho = 1.8 \times 10^{12}\,\mathrm{cm^{-2}}$, per QW. The number of QWs in the heterostructures allows us to easily scale the number of carriers for coupling. In this thesis samples with one QW up to 48 QWs will be used.

The QWs confine the free carriers to a quasi two-dimensional plane, quantizing the electron gas in the growth direction. To further quantize the system in the QW plane we induce a cyclotron motion by employing an external static magnetic field, perpendicular to the QW plane. The magnetic field B governs the in-plane dispersion,

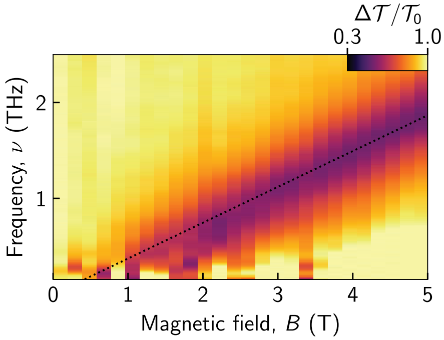

Figure 2.6 | Cyclotron resonance of a 6-QW stack. Change in THz transmission $\Delta\mathcal{T}$, divided by the transmission at $B = 0\,\mathrm{T}$, $\mathcal{T}_0$, as a function of the externally applied perpendicular magnetic field B, showing the absorption of the cyclotron resonance.

giving rise to the formation of Landau levels with an equidistant energy spacing of

$$\hbar\omega_\mathrm{c} = \hbar\frac{eB}{m^*}, \tag{2.15}$$

where m^* is the effective mass of the electrons in the QW. For the employed AlGaAs/GaAs-QWs, $m^* \approx 0.07m_e$, with m_e being the free electron mass. The transition between neighbouring states can be interpreted as the classical cyclotron resonance with frequency ω_c. Only transitions between adjacent Landau levels are dipole allowed. Due to the degeneracy of each Landau level n, as well as spin degeneracy, the filling factor n_ff, up to which Landau level the states are occupied is given by [Hag10]

$$n_\mathrm{ff} = \frac{\rho h}{2eB}, \tag{2.16}$$

where h is the Plank constant. Let's assume low temperatures, as employed for all our measurements at cryogenic temperatures of $< 10\,\mathrm{K}$, where $k_BT \ll \hbar\omega_\mathrm{c}$, with k_B being the Boltzmann constant. Here only the transition from Landau level $n_\mathrm{ff} - 1$ to n_ff is contributing to the accessible dipole moment, as other transitions are Pauli-blocked. The dipole moment of a single QW is then given by

$$d = \sqrt{\frac{\hbar}{m^*\omega_\mathrm{c}}}\sqrt{n_\mathrm{ff}}. \tag{2.17}$$

For weak excitation of the system, Kohn's theorem states that the cyclotron resonance is not affected by Coulomb interactions [Koh61, Maa16]. Consequently, we can consider our system to be bosonic and model it effectively as a harmonic oscillator, as already described in chapter 2.1.

To achieve higher coupling strengths, we can either increase the free carrier density ρ or reduce the effective mass m^* to boost the dipole moment. A full theoretical description in second quantization, including ultrastrong and deep-strong coupling to a metasurface resonator structure, is included in appendix E.

The linear dependence of $\omega_\mathrm{c} = 2\pi\nu_\mathrm{c}$ on the external magnetic field B enables us to continuously tune the cyclotron resonance, as illustrated in Figure 2.6, where the cyclotron resonance of a 6-QW stack results in a reduction in transmission at its resonance frequency ν_c.

2.5. Planar metasurface subwavelength resonator arrays

The photonic modes for USC and DSC are provided by planar, plasmonic resonators, designed for the THz regime. As the vacuum Rabi frequency of a coupled system scales with the electric vacuum field strength, $\Omega_\mathrm{R} \propto \mathbf{E}_\mathrm{vac}$, it is desirable to maximise the field strength of the vacuum field to maximise the coupling strength. This can be achieved by reducing the mode volume of the selected photonic mode.

At first glance, achieving the highest coupling strengths may appear to necessitate the most extreme subwavelength confinement of the vacuum field. However, it is crucial to acknowledge that such extreme confinement poses considerable challenges when attempting to introduce a matter system for coupling into the cavity. At best, the confinement can limit the number of systems N that can be effectively utilized, thereby impacting the potential benefits of scaling the dipole moment with a collective excitation. Similar planar plasmonic resonators as used here can feature effective mode volumes down to $V_\mathrm{eff}/\lambda^3 \approx 6 \times 10^{-10}$, with λ being the free space wavelength [Kel17b]. Utilizing the field enhancement of a scanning tunnelling microscope tip, even effective mode volumes on the order of $V_\mathrm{eff}/\lambda^3 \approx 6 \times 10^{-19}$ are possible [Pel21]. However a thoughtful balance between confinement, practicality and the overlap with the matter system becomes essential in realizing the maximum coupling strength. This balancing act is further complicated by the fact, that for USC and DSC, the coupling itself significantly influences the photonic mode. Here the two systems can no longer be considered as two separate entities, influence each other and even light-matter decoupling might occur [Bay17].

The employed resonator designs are placed directly on top of the QW stack to maximise mode overlap and are derived from a basic plasmonic split ring resonator. The basic split ring resonator design is formed by a capacitive gap, where the field enhancement is concentrated, and a metallic element connects both sides of the capactive element [Pen99]. In the most general simplification, they form an LC-circuit made from an inductor (L, the wire/stripe) and a capacitor (C, the gap). Their folded design makes them generally sub-wavelength in size, rendering the characterization of one single resonator with far-field techniques very inconvenient. Therefore, the resonators are almost always employed on a grid to boost the areal coverage and allow for far-field measurements. These resonators find extensive application in the realm of metamaterials and metasurfaces [Yu13, Che16, Gen17]. In the context of metamaterials, the primary focus revolves around exploring far-field properties under illumination, standing in stark contrast to the near-field optimizations of vacuum fields, as investigated here. The very active field of metasurfaces showcases the immense potential of custom-tailored structures to unlock intricate functionalities, shaping multiple degrees of freedom of light concurrently and manipulating light in unprecedented ways.

While the basic functionality of these planar plasmonic resonators can be understood with equivalent LC-circuit models, much more complicated design optimizations are possible. Here one needs to resort to finite-element simulation of Maxwell's equations for the complete structure, allowing one to extract the full near- and far-field properties with quantitative and predictive accuracy. Details of the employed finite-element frequency-domain (FEFD) simulations, also including the QWs, are included in appendix C. The simulations factor in coupling between neighbouring resonators on the grid and allow for custom-tailoring of the mode spacing, near-field mode profiles and resonance quality factors. In this work, we focus on tailoring the near field to optimize the vacuum field enhancement in the (multiple) QWs as well as the free spectral range of the cavity modes. By expanding the free spectral range

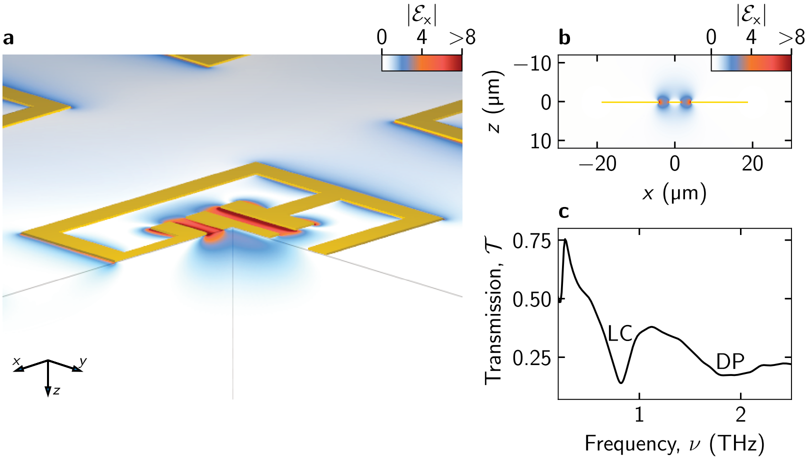

Figure 2.7 | Double gap resonator metasurface. a, Calculated electric near-field enhancement $|\mathcal{E}_x|$ for the LC mode in a plane 150 nm below the resonator. **b**, Near-field enhancement in the xz-plane along $y = 0$. **c**, Measured THz transmission spectrum for the resonator array, with the two lowest modes, the LC and DP mode, marked. Adapted from [Mor21].

of the cavity modes, we create a larger frequency-domain space for the splitting polariton resonances, and simultaneously mitigate the onset of multi-mode strong coupling, as the coupling of one matter resonance to multiple cavity modes can complicate the identification of polariton resonances. The influence of multiple cavity modes on the coupling will be explored in detail in chapter 4.

The first resonator used in this thesis is a mirror symmetric version of a straightforward split ring design (Fig. 2.7**a**), thus suppressing a magnetic field enhancement by design. This resonator will hereafter be referred to as a double gap resonator (DGR). The outer dimensions of the resonators are 37.5 µm by 30 µm, the width of the gold bars is 4 µm. The double capacitive element features two gaps with a width of 2.5 µm and a length of 10 µm. The resonators are deployed as a metasurface in an array with a 60 µm by 60 µm unit cell. In the centre of the gaps the electric near field of the fundamental LC mode is enhanced by more than a factor of 8 with respect to

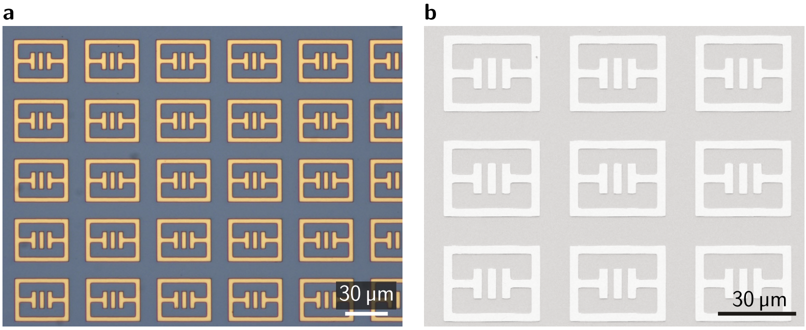

Figure 2.8 | Fabricated double gap resonator metasurface. a, Light microscope picture of an array of resonators. **b**, Scanning electron microscope picture of a sample featuring the double gap resonator.

the far field (Fig. 2.7**b**). The far-field transmission spectrum shows the fundamental LC mode at a frequency of 0.81 THz, and the higher-order, dipolar (DP) mode at a frequency of 1.8 THz (Fig. 2.7**c**). For the DP mode, the field enhancement is localized predominately at the outer edges of the resonator structure.

The resonator array is fabricated on the surface of bare GaAs substrates or the semiconductor structures using electron-beam lithography and wet-chemical processing. Therefore, a gold layer with a thickness of 100 nm is thermally deposited. The finished structures are shown in Figure 2.8. Structuring for all experimentally examined samples shown in this thesis was performed by Maike Halbhuber and Laura Diebel. More details on the sample preparation can be found in appendix A.

2.6. Ultrastrongly coupled Landau-cavity polaritons

A complete sample structure is obtained by integrating the resonator array with a QW stack containing the 2DEG. To interrogate these coupled structures, we place them into a high-numerical aperture magnet-cryostat that keeps the sample at a temperature of $< 10\,\mathrm{K}$ and allows us to apply a perpendicular static magnetic field

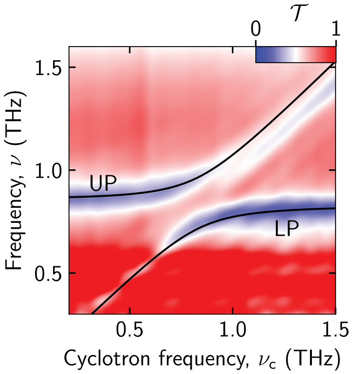

Figure 2.9 | Coupling of a singule QW to the double gap resonator. Measured transmission spectra of a single-QW structure (S1) as a function of the cyclotron frequency, ν_c. The lines mark the lower (LP) and upper (UP) polariton branches with a splitting corresponding to a coupling strength of $\Omega_R/\omega_c = 0.15$. Adapted from [Mor21].

bias to control the cyclotron frequency. In order to measure the THz transmission, we employ THz time-domain spectroscopy (see chapter 2.3).

For our first structure S1 we measure the response of a sample featuring a single quantum well (QW thickness of 10 nm, $\rho = 6.3 \times 10^{11}\,\mathrm{cm}^{-2}$) and a double gap resonator array. The transmission as a function of the cyclotron frequency ν_c (controlled with the external magnetic field bias) is shown in Figure 2.9. Here we observe two main transmission minima. The first resonance starts at a frequency of $\nu \approx 0.9\,\mathrm{THz}$ and slowly starts to curve upwards to asymptotically approach the bare cyclotron resonance for large cyclotron frequencies ν_c with a slope of 1. This mode is the upper polariton resonance (UP). The second mode, the lower polariton (LP) resonance starts at $\nu = 0\,\mathrm{THz}$ for $\nu_c = 0\,\mathrm{THz}$, stays closely located below the cyclotron resonance and becomes visible as a transmission minimum at $\nu_c \approx 0.6\,\mathrm{THz}$, starting to curve downwards, away from the bare cyclotron resonance. The LP then asymptotically approaches the frequency of the bare cavity at 0.81 THz for large ν_c. The two polariton modes are closest in frequency at the anti-crossing point. The third slightly visible minimum emerging below the cyclotron resonance for large ν_c is the lower polariton resonance of the coupling with the second cavity mode. Fitting the full magnetic field dependence of the two polaritons with the Hamiltonian presented in chapter 2.1 yields a coupling strength of $\Omega_R/\omega_c = 0.15$, placing the structure in the USC regime. The procedure also allows us to determine the mixing fractions of

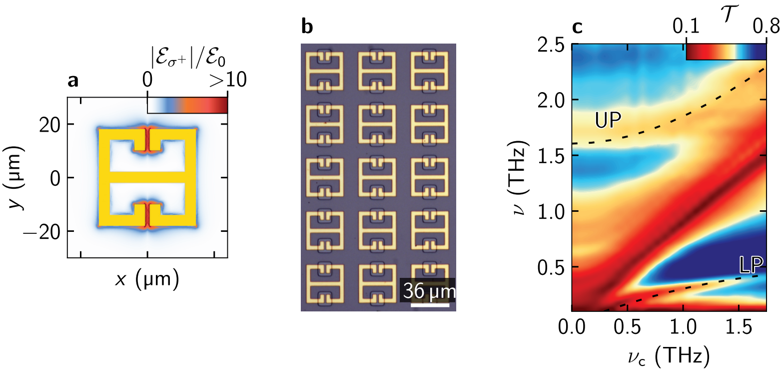

Figure 2.10 | Deep-strong coupling. **a**, Calculated enhancement of the right-circularly polarized near-field component $|\mathcal{E}_{\sigma+}|/\mathcal{E}_0$ of the LC mode of a L-gap resonator, relative to the far-field amplitude, $\mathcal{E}_0$, at a depth of $z = -200\,\mathrm{nm}$ and for $\nu = 0.52\,\mathrm{THz}$. **b**, Light microscope picture of the sample with gold L-gap resonators. The quadratic structures around the capacitive gaps will be discussed in chapter 6. **c**, THz transmission of the sample L6, including the Hopfield fit for the LP and UP with a coupling strength of $\Omega_R/\omega_c = 1.3$. Adapted from [Hal20].

light and matter for each polariton, given by the Hopfield coefficients $(x_\beta, w_\beta, y_\beta, z_\beta)$. At the anti-crossing point, the LP and UP carry equal parts of light and matter contributions ($|x_\beta| \approxeq |w_\beta|$, $|y_\beta| \approxeq |z_\beta|$). However, for higher coupling strength, the anti-resonant coefficients become dominant, and the LP will become more matter-like ($|x_{\mathrm{LP}}| < |w_{\mathrm{LP}}|$, $|y_{\mathrm{LP}}| < |z_{\mathrm{LP}}|$), the UP more light-like ($|x_{\mathrm{UP}}| > |w_{\mathrm{UP}}|$, $|y_{\mathrm{UP}}| > |z_{\mathrm{UP}}|$).

As a next step, we measure the transmission of the structure L6, featuring 6 QWs ($\rho = 1.75 \times 10^{12}\,\mathrm{cm}^{-2}$) and a different resonator structure "L-gap" (Fig. 2.10**a,b**) [Hal20]. This resonator features an LC mode with a frequency of $\nu_{\mathrm{LC}} = 0.52\,\mathrm{THz}$ and a higher DP cavity mode with a frequency of $\nu_{\mathrm{DP}} = 1.95\,\mathrm{THz}$. The vacuum field enhancement of the LC mode is located in two capacitive gaps. Measuring the THz transmission as a function of ν_c shows a LP and UP resonance (Fig. 2.10**c**), alongside the uncoupled cyclotron resonance. Here the UP starts at a frequency of $\nu \approx 1.6\,\mathrm{THz}$ and curves upwards to approach the bare cyclotron resonance. The LP resonance starts to become visible for $\nu_c \approx 0.4\,\mathrm{THz}$ and asymptotically converges toward the bare LC mode frequency of $\nu_{\mathrm{LC}} = 0.52\,\mathrm{THz}$. At the anti-crossing, the two modes are separated in frequency by more than twice their bare frequencies. Fitting the full magnetic field dependence of the LP and UP with the Hopfield Hamiltonian yields a coupling strength of $\Omega_{\mathrm{R}}/\omega_{\mathrm{c}} = 1.3$, placing the structure in the deep-strong coupling regime. Here, the vacuum ground state exhibits significant squeezing (see Fig. 2.4) and hosts a vacuum ground state population of 0.32 virtual photons. This significant change in the vacuum ground state sets the stage for vacuum-induced phenomena such as virtual photon emission from these samples.

Chapter 3

Subcycle nonlinearities of ultrastrong light-matter coupling

As detailed in the introduction and chapter 2, ultrastrong and deep-strong coupling and its modified vacuum ground state give rise to many complex quantum effects and applications. However, most of these effects are studied with linear spectroscopy and under equilibrium conditions. Yet there is a completely separate field of light-matter interaction: strong-field physics, where an electronic resonance is driven by an atomically strong coherent lightwave, resulting in highly non-perturbative dynamics faster than an oscillation cycle of the carrier wave. These dynamics can result in high harmonic and high-order sideband generation as well as other strong-field nonlinearities [Chi01, Cor07, Zak12, Sch14, Lan16, Bor23]. Here, for resonant excitation, the Rabi frequency $\Omega_{\mathrm{R}}^{\mathrm{coh}}$, not the vacuum Rabi frequency $\Omega_{\mathrm{R}}^{\mathrm{vac}}$, quantifies the rate of periodic absorption and stimulated emission. When $\Omega_{\mathrm{R}}^{\mathrm{coh}}$ is greater than the carrier frequency of light, carrier-wave Rabi flopping [Mü01, Raa19] and even extreme subcycle Rabi flopping [Hoh15] can occur. To make a clear differentiation between the Rabi frequency $\Omega_{\mathrm{R}}^{\mathrm{coh}}$ and the vacuum Rabi frequency $\Omega_{\mathrm{R}}^{\mathrm{vac}}$, in this chapter they will feature their respective additional superscript. Yet, in the rest of this thesis, we will suppress the superscript “vac” from the vacuum Rabi frequency to improve readability.

In this chapter, we unify the above fields and establish a new research area at the interface of strong-field and vacuum photonics. By exciting an ultrastrongly coupled light-matter system with intense coherent electromagnetic fields, we tailor a scenario in which the vacuum Rabi frequency, the Rabi frequency of the coherent field, and the carrier frequency of light, all become comparable for the first time. This sets the stage for coherent nonlinearities, where phase transitions in superconductivity [Sch19], cavity chemistry [Hut12, Chi16, Her16, Tho19, Dun22, Sch22], or vacuum-modified electronic transport [Org15, Bar18, PB19, Val21, App22] could be explored. Moreover, it opens up exciting possibilities for novel quantum devices that can leverage parametric nonlinearities to generate coherent light sources or produce squeezed quantum states of light [Rid13]. The results of this chapter are published in an article in *Physical Review Letters* [Mor21].

Two-dimensional THz time-domain spectroscopy

We interrogate and excite the coupled structures with strong THz fields at the same time, using two-dimensional (2D) THz time-domain spectroscopy (Fig. 3.1). Details on the optical setup are given in chapter 2.3. We send two broadband phase-stable singe-cycle THz pulses with a relative delay time τ through our sample structures and record the response as a function of the delay time t with electro-optic sampling. The two strong THz pulses A and B are generated by optical rectification and feature peak field strengths of $1.3\,\mathrm{kV/cm}$ and $2.5\,\mathrm{kV/cm}$, respectively. The ultrabroadband spectra of the pulses allow us to excite and monitor all resonances of our samples simultaneously. Mechanical choppers individually modulate each source and, thus, we can record the individual responses $\mathcal{E}_\mathrm{A}$ and $\mathcal{E}_\mathrm{B}$ of the pulses as well as the response to both pulses $\mathcal{E}_\mathrm{AB}$. Subsequent subtraction allows us to extract the purely nonlinear response $\mathcal{E}_\mathrm{nl} = \mathcal{E}_\mathrm{AB} - \mathcal{E}_\mathrm{A} - \mathcal{E}_\mathrm{B}$ of the sample.

For characterizing the complete nonlinear response, we record $\mathcal{E}_\mathrm{nl}$ as a function of the two delay times t and τ. A subsequent 2D Fourier transform of the dataset allows us to disentangle the nonlinear interaction pathways by a Liouville path analysis based on the pseudo-wave vectors of the two fields, as will be shown in the next subchapter [Kue09, Kue11, Jun12, Maa16, Raa19]. This method offers the powerful capability to separate, e.g., four-wave mixing, pump-probe and higher-order processes, even if they are energy degenerate.

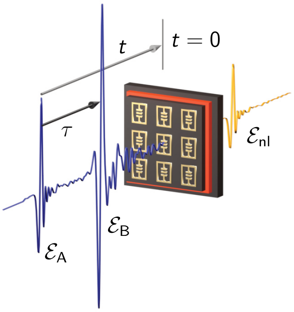

Figure 3.1 | Two-dimensional THz spectroscopy. Schematic of the two THz pules interrogating the sample, and their respective delays: t: electro-optic delay time (real time). τ: relative delay of the two THz waveforms, $\mathcal{E}_{\mathrm{A}}$ and $\mathcal{E}_{\mathrm{B}}$. $\mathcal{E}_{\mathrm{nl}}$: nonlinear signal. Adapted from [Mor21].

3.1. Non-perturbative nonlinearities of Landau polaritons

First, we measure the linear transmission of our structure, S6 (Fig. 3.2**a**). This sample features 6 QWs, each with a doping density of $\rho = 1.75 \times 10^{12}\,\mathrm{cm}^{-2}$ and a double gap resonator array (see chapter 2.5). Coupling of the cyclotron resonance (CR) to the fundamental LC mode at a frequency of $\nu_{\mathrm{LC}} = 0.81\,\mathrm{THz}$, as well as the dipolar mode at $\nu_{\mathrm{DP}} = 1.8\,\mathrm{THz}$ results in multiple transmission minima. At lower frequencies, a lower polariton (LP) branch emerges from the cyclotron resonance, while an upper polariton resonance (UP) is observed at a frequency of 1.5 THz when $\nu_{\mathrm{c}} = 0\,\mathrm{THz}$ (Fig. 3.2**c**). As ν_{c} increases, the polariton frequencies exhibit opposite curvatures, resulting in the distinctive anti-crossing shape. Additionally, off-resonant coupling of the cyclotron resonance with the dipolar cavity mode (DP) generates a third resonance referred to as dipolar polariton (DPP), which is positioned approximately 0.2 THz below the UP branch. The transmission minimum at ν_{c} can be attributed to THz absorption by the cyclotron resonance within the uncoupled regions between the resonator structures. At the anti-crossing point the LP, UP, and DPP resonances are centred at frequencies of 0.4 THz, 1.65 THz, and 1.3 THz, respectively (Fig. 3.2**c**).

To validate our measurements and get a deeper insight into the origins of the coupled modes via their near-field distributions, we extend our finite element simulations to include the gyrotropic response of the cyclotron resonance within the QWs. This

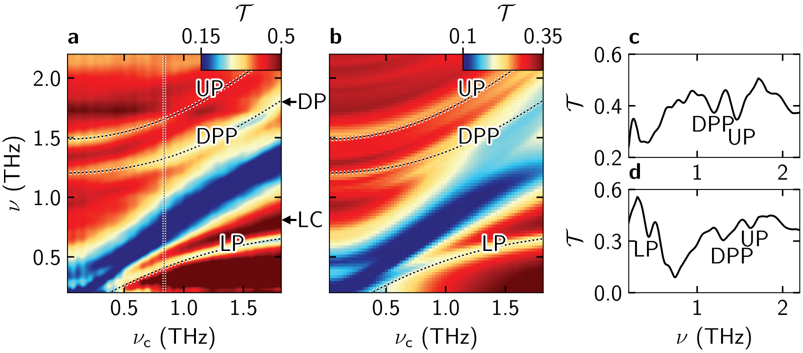

Figure 3.2 | Transmission spectra of the ultrastrongly coupled structure S6. **a**, Measured transmission spectra as a function of the cyclotron frequency ν_c. The dotted curves show the lower (LP) and upper polariton mode (UP) obtained from Hopfield's model for a coupling strength of $\Omega_R^{vac}/\omega_c = 0.77$. DPP: additional polariton mode. The vertical dotted line marks the anticrossing point, $\nu_c = 0.84\,\mathrm{THz}$. The arrows indicate the frequencies of the uncoupled LC and DP cavity modes, respectively. **b**, Calculated transmission spectra including the dashed lines of panel **a**. **c**, Transmission spectrum extracted from the data in **a**, at $\nu_c = 0\,\mathrm{THz}$ and **d**, near the anti-crossing point. Adapted from [Mor21].

enables us to compute the transmission of the ultrastrongly coupled structure without relying on any free fit parameters (see appendix C for more details). By adopting an electron doping density of $\rho = 2.1 \times 10^{12}\,\mathrm{cm}^{-2}$ per quantum well (Fig. 3.2**b**), our calculations yield an excellent agreement with the experimental spectra. Our simulations provide insights into the contributions of the individual bare resonator modes to each of the coupled modes. By comparing the corresponding near-field distributions, it is possible to differentiate their effects. Notably, the near-field distribution of the lower polariton mode (see Fig. 3.3**a**) exhibits a resemblance to the LC mode, primarily due to its concentration of the field within the central gap region. Conversely, the dipolar mode expels most of the field from the gap region, which is evident in the near-field distribution of the DPP mode (shown in 3.3**b**), reflecting its similarity to the DP cavity mode. Lastly, owing to its significant field enhancement within the gap, the upper polariton mode is linked to the LC mode

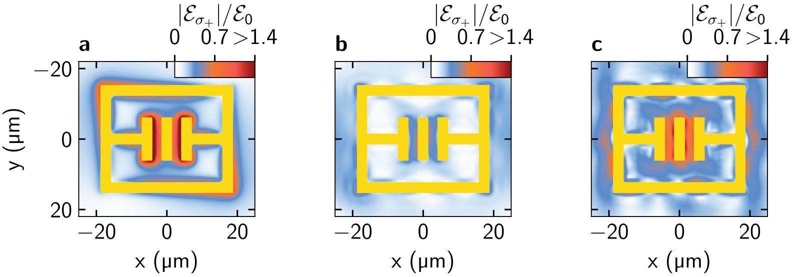

Figure 3.3 | Calculated coupled mode profiles. Right-circularly polarized near-field component $|\mathcal{E}_{\sigma_+}|/\mathcal{E}_0$, to which the cyclotron resonance selectively couples, whereby $\mathcal{E}_0$ is the far-field amplitude at $\nu_c = 0.84\,\mathrm{THz}$, **a**, $\nu = 0.46\,\mathrm{THz}$ for the LP, **b**, $\nu = 1.30\,\mathrm{THz}$ for the DPP and **c**, $\nu = 1.73\,\mathrm{THz}$ for the UP. Adapted from [Mor21].

(3.3**c**). We derive the coupling strength from the frequency dependence of the LP and UP on the magnetic field and obtain $\Omega_R^{\mathrm{vac}}/\omega_c = 0.77$ by diagonalizing the light-matter Hamiltonian.

Nonlinear measurements

With this analysis of the linear properties, we are now equipped to investigate the nonlinear response of our structure by two-dimensional THz spectroscopy. Initially, we deactivate the magnetic field ($\nu_c = 0\,\mathrm{THz}$) to examine the nonlinear characteristics of the cavity interacting with the electron plasma. In this scenario, the UP and DPP modes exhibit frequencies of 1.5 and 1.2 THz, respectively. We record the nonlinear response, $\mathcal{E}_{\mathrm{nl}}$, as a function of the relative delay τ and the electro-optic sampling time t. $\mathcal{E}_{\mathrm{nl}}$ displays a complex time-domain structure featuring multiple oscillation patterns (Fig. 3.4**a**). Here, the fronts of constant phase for pulse A are observed as vertical lines, while those for pulse B appear as diagonal lines along $t - \tau = \mathrm{const.}$ $\mathcal{E}_{\mathrm{nl}}$ exhibits its maximum amplitude around $\tau = 0\,\mathrm{ps}$, where both pulses interfere constructively, resulting in oscillations with frequencies corresponding to the UP and DPP modes. This constructive interference gives rise to prominent oscillatory behaviour along the t axis, periodically modulating the envelope of $\mathcal{E}_{\mathrm{nl}}$ with minima at approximately $t = 3\,\mathrm{ps}$ and 5.5 ps. Conversely, for $\tau = \pm 0.25\,\mathrm{ps}$,

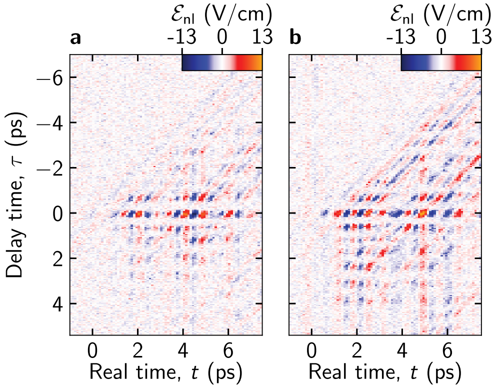

Figure 3.4 | Nonlinear response of sample S6. **a**, Measured nonlinear response $\mathcal{E}_{\rm nl}(t,\tau)$ for $\nu_{\rm c} = 0\,\mathrm{THz}$. **b**, $\mathcal{E}_{\rm nl}(t,\tau)$ at the anti-crossing point, where $\nu_{\rm c} \approx \nu_{\rm LC}$. Adapted from [Mor21].

the pulses undergo destructive interference, leading to a reduction in the THz peak amplitude and consequently diminishing the magnitude of $\mathcal{E}_{\rm nl}$.

Next, we set the external magnetic field bias B to $2.3\,\mathrm{T}$, which corresponds to the anti-crossing point of the cyclotron resonance and the LC mode, $\nu_{\rm c} \approx \nu_{\rm LC}$. Here the overall nonlinear response is similar to the measurement at $B = 2.3\,\mathrm{T}$, yet a higher level of coherence becomes apparent, indicated by the slower decay of $\mathcal{E}_{\rm nl}$ and the persistence of a finite amplitude for delay times up to $\tau = 5\,\mathrm{ps}$ (Fig. 3.4**b**). Furthermore, in this configuration, the beating pattern arises from the interactions of three, rather than two resonances and suggests the presence of a rich structure of nonlinearities. In order to further investigate the nonlinearities for both measurements, we need to perform a two-dimensional Fourier transform (see next section).

For our measurements, the vacuum Rabi frequency of our structure, $\Omega_{\rm R}^{\rm vac}$, can be determined based on the frequencies of the polariton branches measured in equilibrium. However, the Rabi frequency of the coherent drive, $\Omega_{\rm R}^{\rm coh}$, depends on the amplitude of the external field and the coupling of the far field to the light-matter hybridized modes. We determine $\Omega_{\rm R}^{\rm coh}$ by performing finite-element frequency-domain calculations (see appendix C) to calculate the field distribution of the coupled system in the plane of the QWs. By extracting the complex-valued frequency-domain data from the simulation and multiplying it with the spectrum of our THz transient,

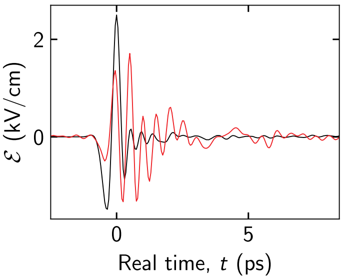

Figure 3.5 | Far-field and near-field electric field waveforms. Black curve: Recorded electric field waveform $\mathcal{E}(t)$ incident on the sample structure. Red curve: Calculated near-field waveform, averaged over the complete gap area of the resonator structure.

we calculate the local near-field frequency response induced by the far-field THz transient. The phases of the near-field components do not vary significantly within the QW plane. Transforming the result back into the time domain, we obtain near-field waveforms that feature a slightly more narrow frequency bandwidth, but the same phase. By averaging these waveforms within the capacitive gap region of our THz resonators, we determine a peak near-field amplitude of 1.7 kV/cm for excitation with a peak far-field amplitude of 2.5 kV/cm (Fig. 3.5). From these data, we obtain a coherent Rabi frequency of $\Omega_{\mathrm{R}}^{\mathrm{coh}} = 2\pi \times 2.7\,\mathrm{THz}$.

Liouville path analysis

For the systematic analysis of all individual nonlinear optical interaction processes, we perform a two-dimensional Fourier transform [Kue09, Kue11, Jun12, Maa16, Raa19] of the time-domain data. This yields the nonlinear amplitude spectrum, $\mathcal{A}_{\mathrm{nl}}(\nu_t, \nu_\tau)$, which depends on the frequencies ν_t and ν_τ associated with the respective delay times.

For our data without the external magnetic field, $\mathcal{A}_{\mathrm{nl}}(\nu_t, \nu_\tau)$ shows distinct resonances at frequencies $\nu_t = \nu_{\mathrm{UP}}, \nu_{\mathrm{DPP}}$ and multiple frequencies ν_τ (Fig. 3.6**a**). Here, each maximum of $\mathcal{A}_{\mathrm{nl}}$ represents a unique multi-photon process, which is a linear combination of any number ≥ 1 of pseudo-wave vectors of the incident fields, $\mathbf{k}_{\mathrm{A}} = (\nu_\beta, 0)$ and $\mathbf{k}_{\mathrm{B}} = (\nu_\beta, \nu_\beta)$, where ν_β with $\beta \in$ (LP,UP,DPP) denotes the polariton frequencies.

Pump-probe (PP) processes resulting from third-order nonlinearities lie along the

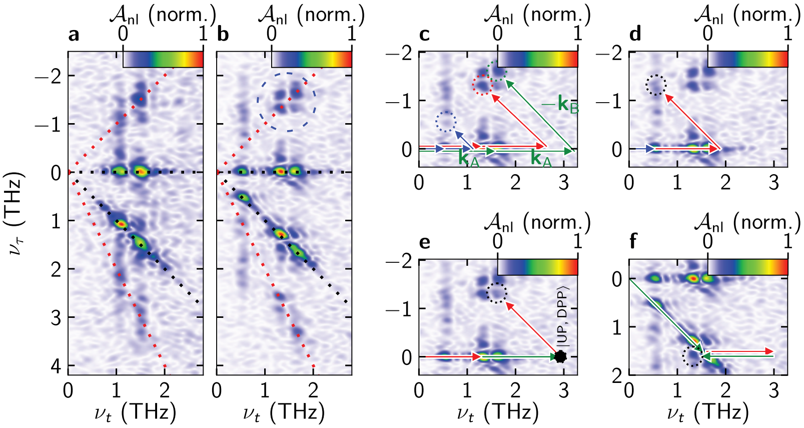

Figure 3.6 | Experimental amplitude spectra $\mathcal{A}_{\text{nl}}(\nu_t, \nu_\tau)$ **a**, of the time-domain data of Figure 3.4**a**, at 0 T, normalized to its peak value. Dashed lines as guides to the eye: third-order processes with only one resonance. **b**, of the time-domain data of Figure 3.4**b**, at 2.3 T. Dashed circle: four-wave-mixing processes of the UP and DPP. **c-f**, Liouville path analysis of nonlinear interactions: **c**, decomposition of the four-wave mixing processes of the LP (blue arrows), DPP (red arrows) and UP resonance (green arrows), individually. **d**, Liouville path for a four-wave mixing process combining the nonlinear polarization of the LP and DPP. **e,f**, Four-wave mixing processes mixing the UP and DPP resonances. Black dot: virtual level |UP,DPP⟩. Adapted from [Mor21].

black dashed lines and are formed by the process

$$P^{(3)}_{\text{PP}}(\nu_\beta) = \chi^{(3)}(\nu_\beta, \nu_\beta, -\nu_\beta)\mathcal{A}_m(\nu_\beta)\mathcal{A}_n(\nu_\beta)\mathcal{A}_n(-\nu_\beta), \tag{3.1}$$

where $\chi^{(3)}$ represents the corresponding nonlinear susceptibility, and $\mathcal{A}_m$ with $m, n \in$ (A,B), $m \neq n$ are the spectral amplitudes of the incident fields. Positive frequencies ν_β indicate an energy transfer from the field into the polarization of polariton states. In contrast, negative frequencies represent the opposite process. The wave vectors for the PP processes, $\mathbf{k}_{\text{PP1}} = \mathbf{k}_\text{A} + \mathbf{k}_\text{B} - \mathbf{k}_\text{B}$ and $\mathbf{k}_{\text{PP2}} = \mathbf{k}_\text{B} + \mathbf{k}_\text{A} - \mathbf{k}_\text{A}$, result in a phase cancellation of one of the incident field components, indicating that the PP processes probe the (incoherent) population response. Contrary, the four-wave mixing (4WM) signals marked by the red dashed lines are functions of the phases of both fields and probe the nonlinear polarization,

$$P^{(3)}_{\mathrm{4WM}}(\nu_\beta) = \chi^{(3)}(\nu_\beta, \nu_\beta, -\nu_\beta)\mathcal{A}_m(\nu_\beta)\mathcal{A}_m(\nu_\beta)\mathcal{A}_n(-\nu_\beta). \tag{3.2}$$

The spectra extracted from the data recorded at the anticrossing point (Fig. 3.6**b**), feature additional resonances at the frequency on the LP resonance.

We further illustrate these processes with a Liouville wave vector decomposition. As an example, the decomposition of the 4WM signals located at $(\nu_\beta, -\nu_\beta)$ is illustrated in Figure 3.6**c**, where these signals for the LP, DPP, and UP resonances are highlighted with blue, red, and green arrows, respectively, representing the Liouville paths. In each case, $P^{(3)}_{\mathrm{4WM}}(\nu_\beta)$ requires the coherent mixing of two photons from $\mathcal{E}_\mathrm{A}$ (horizontal arrows) and one photon from $\mathcal{E}_\mathrm{B}$ (diagonal arrows), resulting in a polarization at a frequency of ν_β. This emitted polarization is subsequently detected. Notably, all photons involved in this process are resonant with their respective polaritons.

Interestingly, $\mathcal{A}_\mathrm{nl}$ exhibits additional peaks at frequencies such as $(\nu_\mathrm{LP}, -\nu_\mathrm{DPP})$, which arise from nonlinear polarization mixing between different polariton resonances (Fig. 3.6**d**). In this scenario, $\mathcal{E}_\mathrm{A}$ contributes a photon resonant with the LP (blue arrow) and another resonant with the DPP (red horizontal arrow), while a photon resonant with the DPP is emitted into $\mathcal{E}_\mathrm{B}$ (red diagonal arrow). This process corresponds to the nonlinear polarization

$$P^{(3)}_{\mathrm{4WM}}(\nu_\mathrm{LP}) = \chi^{(3)}(\nu_\mathrm{LP}, \nu_\mathrm{DPP}, -\nu_\mathrm{DPP})\mathcal{A}_\mathrm{A}(\nu_\mathrm{LP})\mathcal{A}_\mathrm{A}(\nu_\mathrm{DPP})\mathcal{A}_\mathrm{B}(-\nu_\mathrm{DPP}). \tag{3.3}$$

Equivalent maxima for 4WM and PP processes involving the mixing of polarizations between the UP and the DPP are displayed in panels **e** und **f**, respectively. These signatures of inter-polariton mixing are indicative of a strongly nonlinear regime where the normal-mode approximation of the polariton resonances is violated.

To investigate the expected and potential nonlinear resonances, we systematically scan the 2D frequency space, considering all possible third-order nonlinearities of the three polariton branches. These arise from the various combinations of their corresponding wave vectors, accounting for both fields (A and B) and mixing processes with positive and negative frequencies. Figure 3.7 illustrates all the pump-probe

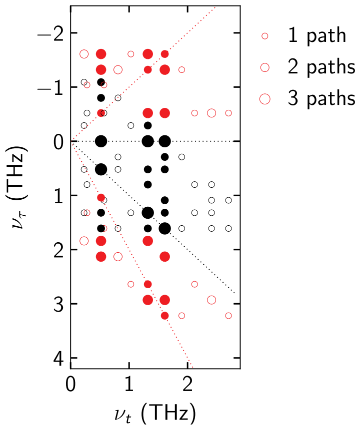

Figure 3.7 | All combinatorially possible nonlinear resonances of $\mathcal{A}_{\mathrm{nl}}(\nu_t, \nu_\tau)$ for third-order nonlinear interactions between the LP, the UP and the DPP resonances, colored black and red for pump-probe and four-wave-mixing processes, respectively. The size of the dots scales with the number of Liouville paths leading to the center position of the dot. Adapted from [Mor21].

processes (black circles) and four-wave-mixing processes (red circles). Filled circles represent processes that yield a nonlinear polarization oscillating at the frequency of one of the polariton resonances, resulting in strong emission into the far field. Conversely, open circles correspond to off-resonant polarization components that do not significantly contribute to the total emission [Boy08]. Additionally, as certain locations in frequency space can be accessed through multiple Liouville paths, the degeneracy is depicted by the size of each circle.

3.2. Subcycle quantum model

The plethora of measured and possible nonlinear resonances calls for a quantitative theoretical description for strongly nonlinear excitation of ultrastrongly coupled structures. Thus, we develop a theory extending the description of light-matter coupling beyond the scope of chapter 2.1, including non-perturbative nonlinear phenomena and the full Landau fan with its individual levels.

First, we extend the Hamiltonian to include not only the first cavity mode, at a frequency of $\nu_{\mathrm{LC}} = 0.81\,\mathrm{THz}$, but also the dipolar mode at $\nu_{\mathrm{DP}} = 1.8\,\mathrm{THz}$. The

Hamiltonian is then given by

$$\begin{aligned}\hat{H} =& \sum_j \hbar\omega_j \hat{a}_j^\dagger \hat{a}_j + \hbar\omega_\mathrm{c}\hat{b}^\dagger\hat{b} \\ &+ \sum_j \Omega_{\mathrm{R},j}^{\mathrm{vac}} \left(\hat{a}_j^\dagger + \hat{a}_j\right)\left(\hat{b}^\dagger + \hat{b}\right) + \sum_j \hbar D_j \left(\hat{a}_j^\dagger + \hat{a}_j\right)^2 + \hat{H}_\mathrm{ext}.\end{aligned} \tag{3.4}$$

Here, $j \in$ (LC,DP), $D_j = \left(\Omega_{\mathrm{R},j}^{\mathrm{vac}}\right)^2/\omega_\mathrm{c}$, and $\hat{H}_\mathrm{ext}$ contains the coupling of the cavity modes to the THz far field. We calculate the dynamics of the system by using Heisenberg's equation of motion for each of the operators,

$$\frac{d\hat{A}(t)}{dt} = -\frac{i}{\hbar}[\hat{A}(t), \hat{H}], \tag{3.5}$$

where $\hat{A}(t)$ is a bosonic operator. Now we derive the time-dependent differential equations by applying the corresponding bosonic commutation relations, resulting in

$$\begin{aligned}\frac{d\hat{a}_j(t)}{dt} =& - i\omega_j\hat{a}_j(t) - i\Omega_{\mathrm{R},j}^{\mathrm{vac}}\left[\hat{b}(t) + \hat{b}^\dagger(t)\right] - i2D_j\left[\hat{a}_j(t) + \hat{a}_j^\dagger(t)\right] \\ &- \frac{i}{\hbar}\left[\hat{a}_j(t), \hat{H}_\mathrm{ext}\right],\end{aligned} \tag{3.6}$$

$$\frac{d\hat{b}(t)}{dt} = - i\omega_\mathrm{c}\hat{b}(t) - i\sum_j \Omega_{\mathrm{R},j}^{\mathrm{vac}}\left[\hat{a}_j(t) + \hat{a}_j^\dagger(t)\right]. \tag{3.7}$$

In order to derive differential equations for the simulation, we adopt a mean-field approach by introducing the mean values $\alpha_j \equiv \langle\hat{a}_j\rangle(t)$ and $\beta \equiv \left\langle\hat{b}\right\rangle(t)$, where we omit the explicit temporal dependence, for simplicity. Additionally, we incorporate phenomenological dephasing rates γ_j for each mode.

$$\frac{d}{dt}\alpha_j = -i\omega_j\alpha_j - \gamma_j\alpha_j - i\Omega_{\mathrm{R},j}^{\mathrm{vac}}\left[\beta + \beta^*\right] - i2D_j\left[\alpha_j + \alpha_j^*\right] + \kappa_j\sqrt{\gamma_j}\mathcal{E}_\mathrm{THz}(t), \tag{3.8}$$

$$\frac{d}{dt}\beta = -i\omega_\mathrm{c}\beta - i\sum_j \Omega_{\mathrm{R},j}^{\mathrm{vac}}\left[\alpha_j + \alpha_j^*\right]. \tag{3.9}$$

Coupling to the external THz field $\mathcal{E}_\mathrm{THz}(t)$ is accounted for by the respective dipole moment of the cavity mode through a coupling constant κ_j. Additionally, a factor of $\sqrt{\gamma_j}$ is included, arising from the fluctuation-dissipation theorem [Kub66].

Under the strong external THz field, the description of the electronic system as an infinitely bosonic harmonic oscillator is no longer applicable even for a perfectly parabolic potential. Here, electrons are no longer merely excited from the highest occupied Landau level to the lowest unoccupied Landau level, and the resulting interactions of excited electrons, no longer covered by Kohn's theorem, affect the cyclotron resonance [Koh61, Maa16]. In fact, as the model will show, charge carriers will be excited multiple rungs over the highest occupied Landau level. Therefore, we extend our model by introducing the full multi-level structure of the Landau fan to the model, and include the nonequidistant energy progression originating from the GaAs band structure with a density matrix approach [Maa16]:

$$\hat{\mathcal{H}}_\rho = \begin{pmatrix} \hbar\omega_1 & \mu_{12}e^{-i\omega_{12}t} & \dots & 0 \\ \mu_{12}e^{i\omega_{12}t} & \ddots & \ddots & \vdots \\ \vdots & \ddots & \ddots & \vdots \\ 0 & \dots & \dots & \hbar\omega_N \end{pmatrix}. \tag{3.10}$$

Here $N = 100$ denotes the number of implemented Landau levels. The Hamiltonian of the subsystem in matrix form, $\hat{\mathcal{H}}_\rho$, consists of the eigenenergies of the n-th Landau level, $\hbar\omega_n$, on the diagonal. The neighbouring minor diagonal is populated by coupling terms between adjacent Landau levels, governed by the selection rules of Landau electrons and the driving field:

$$\mu_{mn} = d_{mn} \times \sum_j \left(\alpha_j + \alpha_j^*\right) \Omega_{\mathrm{R},j}^{\mathrm{vac}}. \tag{3.11}$$

Here, the driving term for the transition is obtained by multiplying the dipole moment d_{mn} with the sum of the real parts of the cavity fields, scaled by their respective vacuum Rabi frequency. Whereas the RWA commonly employed for perturbative nonlinearities couples the electronic excitations by a complex-valued field that neglects counter-rotating wave components, here, we are required to include these terms and employ the real-valued electric field. The dipole moments follow the scaling relation $d_{mn} = el_0\sqrt{m}$ for the transition between adjacent Landau levels m and n, where e represents the elementary charge, $l_0 = \sqrt{\hbar/eB}$ denotes the magnetic length, and B represents the static magnetic bias field (see also subchapter 2.4).

The resulting density matrix ρ includes the population density of the Landau levels on its diagonal, while the off-diagonal entries $\rho_{mn} = \rho^*_{nm}$ describe the coherent polarization between Landau levels m and n. In addition, coherences also exist between states which are not connected via a dipole moment, as population can be transferred from Landau level $n = 1$ to, e.g., Landau level $n = 3$, via intermittently exciting Landau level $n = 2$.

$$\rho = \begin{pmatrix} \rho_{11} & \cdots & \rho_{1N} \\ \vdots & \ddots & \vdots \\ \rho_{N1} & \cdots & \rho_{NN} \end{pmatrix}. \tag{3.12}$$

The temporal evolution of the density matrix is determined by solving the von Neumann equation,

$$-i\hbar \frac{\partial \rho}{\partial t} = [\hat{\mathcal{H}}, \rho] - i\gamma \circ \rho, \tag{3.13}$$

where γ is the damping matrix. Here dephasing is phenomenologically implemented for each element of ρ individually, by the element-wise product, $\circ$. We will adopt this description of our Landau ladder and substitute the polarization term of Equation 3.8, $\beta(t) + \beta^*(t)$, with the polarization field of the multi-level Landau system,

$$P_{\mathrm{L}}(t) = \sum_{m,n} \rho_{mn}(t) d_{mn}. \tag{3.14}$$

This results in our final form of the differential Equation 3.8:

$$\frac{d}{dt}\alpha_j = -i\omega_j\alpha_j - \gamma_j\alpha_j - i\Omega^{\mathrm{vac}}_{\mathrm{R},j} P_{\mathrm{L}} - i2D_j \left[\alpha_j + \alpha_j^*\right] + \sqrt{\gamma_j}\kappa_j \mathcal{E}_{\mathrm{THz}}(t). \tag{3.15}$$

We model our coupled system by solving the system of differential equations, from which we obtain the cavity fields $\alpha_j(t)$ and the time-dependent density matrix, ρ. By adding the fields of both cavity modes as well as the incident THz field $\mathcal{E}_{\mathrm{THz}}$ according to

$$\mathcal{E}_{\mathrm{measured}}(t) = \mathcal{E}_{\mathrm{THz}}(t) - \sum_j \sqrt{\gamma_{\mathrm{cav},j}}\alpha_j, \tag{3.16}$$

we obtain the total field corresponding to the field measured in the experiment. By calculating $\mathcal{E}_{\text{measured}}(t)$ for all combinations of the two THz pulses analogously to the experiment, we get the nonlinear response $\mathcal{E}_{\text{nl}}$.

Including the nonlinearities

The inclusion of a perfectly equidistant ladder of Landau levels into our model alone does not produce a nonlinear response $\mathcal{E}_{\text{nl}}$. However, this step is a crucial prerequisite for incorporating the nonlinearities present in the sample structure. The nonlinearities depend on the distribution of excited Landau electrons along the Landau fan as well as the precise energy dispersion of the conduction band of the host semiconductor. To account for the observed behaviour, we consider multiple potential sources of nonlinearities.

Firstly, we acknowledge that the conduction band of the GaAs quantum wells does not exhibit a perfectly parabolic shape and results in a non-equidistant progression of the Landau level frequencies. Such a non-equidistant Landau ladder has been shown to produce significant nonlinearities in GaAs quantum wells [Maa16] and in graphene [KO17]. An effective model for the Landau level frequencies ω_n is given by

$$\omega_n = -\omega_{np}/2 + \sqrt{\omega_{\text{np}}^2/4 + \omega_{\text{np}} eB/m^*(n+0.5)}. \tag{3.17}$$

In the above equation, n represents the Landau level index, m^* is the effective mass given by $m^* = 0.066 m_e$, where m_e is the electron mass. The elementary charge is denoted by e, B is the static magnetic bias field, and $\omega_{np} = 2\pi \times 237\,\text{THz}$ is a fitting parameter for GaAs [Zaw94]. For our sample with a doping density of $\rho = 1.75 \times 10^{12}\,\text{cm}^{-2}$ per QW and a magnetic field of 2.3 T, the filling factor at the anticrossing point is $n_{\text{ff}} = 15.7$. In this configuration, the transition frequency in the vicinity of the Fermi level is $\omega_{\text{c}} = 0.868\,\text{THz}$, while the adjacent higher and lower transitions are centred at 0.874 THz and 0.862 THz, respectively. As we will see, these small deviations of the cyclotron frequency of less than 1%, only account for a small part of the observed nonlinearities, pointing at the presence of other nonlinear effects.

While the gold resonators should respond linearly up to much stronger fields [Lan14], it has been shown, that strong-field, non-perturbative excitation of Landau electrons can lead to sizeable nonlinearities beyond Kohn's theorem, due to dynamical Coulomb correlations [Maa16]. Kohn's theorem establishes that the purely repulsive electron-electron Coulomb interaction, in isolation, cannot give rise to observable nonlinear effects in a two-dimensional electron gas. Nonetheless, in real-world scenarios, a 2DEG invariably exists together with a positive background charge. The electron-ion interaction is not subject to the limitations posed by Kohn's theorem and induces nonlinearities under excitation, namely a softening of the cyclotron resonance. To appropriately account for these effects in the model, we introduce a measure for the instantaneous degree of excitation of the electronic system, $\rho_{\text{exc}}(t)$, and dynamically change the Landau level eigenenergies and dipole moments in the non-equilibrium situation:

$$\rho_{\text{exc}}(t) = \sum \frac{1}{2} \left|\text{diag}(\rho(t)) - \text{diag}\left(\rho_0\right)\right|_m h_m, \tag{3.18}$$

$$h_m = \begin{cases} m - l_f & \text{for} \quad m < l_f \\ m - l_f + 1 & \text{for} \quad m \geq l_f'. \end{cases} \tag{3.19}$$

The degree of excitation, $\rho_{\text{exc}}(t)$, considers the number of excited Landau electrons as well as their distance in Landau level space relative to the equilibrium distribution, ρ_0, and equilibrium Landau level index at the Fermi level, $l_f = 16 \approx n_{\text{ff}}$. For the case of a perfectly parabolic conduction band, the Landau fan behaves as a harmonic oscillator and ρ_{exc} is equal to $|\beta|^2$ of our bosonic theory. With ρ_{exc} we can now introduce an effective, dynamical scaling of the Landau level energies by the scaling factor U_e:

$$\omega_n \to \omega_n \times \left(1 + U_e \rho_{\text{exc}}\right)^{-1}, \tag{3.20}$$

and a rescaling of all dipole moments d_{mn} by a scaling factor U_d:

$$d_{mn} \to d_{mn} \times \left(1 + U_d \rho_{\text{exc}}\right)^{-1}. \tag{3.21}$$

Calibration of the model

As our model does not fully capture the coupling of an external THz field into the cavity mode and its field enhancement by the cavity, we have to calibrate the

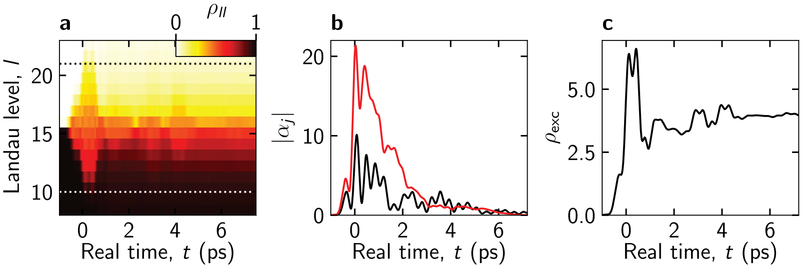

Figure 3.8 | Simulated internal dynamics. a, Population of each Landau level for the setting of Figure 3.10. Dashed lines: threshold energy for longitudinal optical phonon scattering (see text). **b**, Population of the LC (black) and DP (red) cavity modes for $\tau = 0\,\mathrm{ps}$. **c**, Electronic excitation ρ_{exc}. Adapted from [Mor21].

model to accurately match the experimental conditions. The field strength of the driving pulses is quantified by measurements of the power from our tilted-pulse-front THz source (pulse B). We calculate the corresponding peak amplitude by using the THz waveform obtained through electro-optic sampling, as well as the beam profile measured with a pinhole at the sample position. The model parameters scaling the field amplitudes are then adjusted to match the density of electronic excitations in theory and experiment. To this end, we calculate the absorption of the THz pulses based on the linear transmission spectra of our structure within the spectral range of the three polariton resonances, as well as the corresponding spectral power density of the incident THz pulses. Considering the gap area of our THz resonators, where the strongest contribution to the light-matter interaction occurs, we obtain an excitation density of $6.95 \times 10^{11}\,\mathrm{cm}^{-2}$ Landau electrons per QW. The density of excitations in the simulations is given by $\rho_{\mathrm{exc}} \times \frac{2eB}{h}$. Here the excitation parameter ρ_{exc} is multiplied by the constant density of states per Landau cylinder, $\frac{2eB}{h}$. Additionally, one has to account for different coupling strengths of the two cavity modes to the incident far field by introducing individual coupling factors κ_j, where $\kappa_{\mathrm{LC}} = 1$ and $\kappa_{\mathrm{DP}} = 1.5$ for the LC and DP cavity modes, respectively.

Finally, we utilize the theory to model the nonlinear subcycle dynamics observed in the experiment. First, we observe the population dynamics of each Landau level upon excitation (Fig. 3.8**a**). Within the full width at half maximum (FWHM) of pulse $\mathcal{E}_{\mathrm{B}}(t)$ of 2 ps around $t = 0$ ps, Landau electrons are coherently excited from up to 5 levels below to 5 levels above the Fermi level. The maximum energy separation is still just below the energy of the longitudinal optical phonon of GaAs, which would lead to electron-phonon scattering and strong dephasing. The degree of excitation of the electrons, ρ_{exc}, condenses the electron dynamic into one parameter. After the initial fast excitation, the electron distribution displays some trailing oscillations and slowly relaxes into its new equilibrium distribution (Fig. 3.8**c**). The population of the LC and DP cavity modes, $|\alpha_j|$, experience a steep increase at $t = 0$ ps and decay exponentially afterwards with superimposed oscillations. As expected for ultrastrong light-matter coupling, the cavity and the Landau electrons periodically exchange energy, which results in the observed oscillations with alternating local maxima of ρ_{exc} and $|\alpha_j|$ (Fig. 3.8**b,c**).

Comparison of theory and experiment

After fitting the resonance frequencies, damping factors and the field calibration to the experimental data, we are left with the two values of U_e and U_d as free fitting parameters. First, we investigate the situation for $U_d = U_e = 0$, where only the non-parabolic band structure is responsible for the nonlinear response. Here the calculated nonlinear field $\mathcal{E}_{\mathrm{nl}}$ displays coherent oscillations that qualitatively resemble the experimental data (Fig. 3.9**a**). However, the calculated modulation amplitude is significantly lower (only 0.6 V/cm) compared to the measured amplitude of 13 V/cm (Fig. 3.4). Additionally, the calculated modulation is slower, resulting in most of the spectral weight being concentrated on the LP resonance (compare Fig. 3.6**b** and Fig. 3.9**b**).

Next, we incorporate the Landau energy rescaling due to dynamical Coulomb correlations with $U_e = 0.016$ (Fig. 3.9**c,d**). Now the nonlinear amplitude of the calculated data matches the amplitude of the experiment, but the low-frequency components are still overestimated. Likewise, when including both non-parabolic effects and rescaling of the transition dipole moments (with $U_d = 0.064$), similar results are obtained with a nonlinear amplitude matching the experimental data, yet with a focus on low-frequency components (Fig. 3.9**e,f**). Including both rescaling effects due to dynamical Coulomb correlations, but not the non-parabolic conduction band

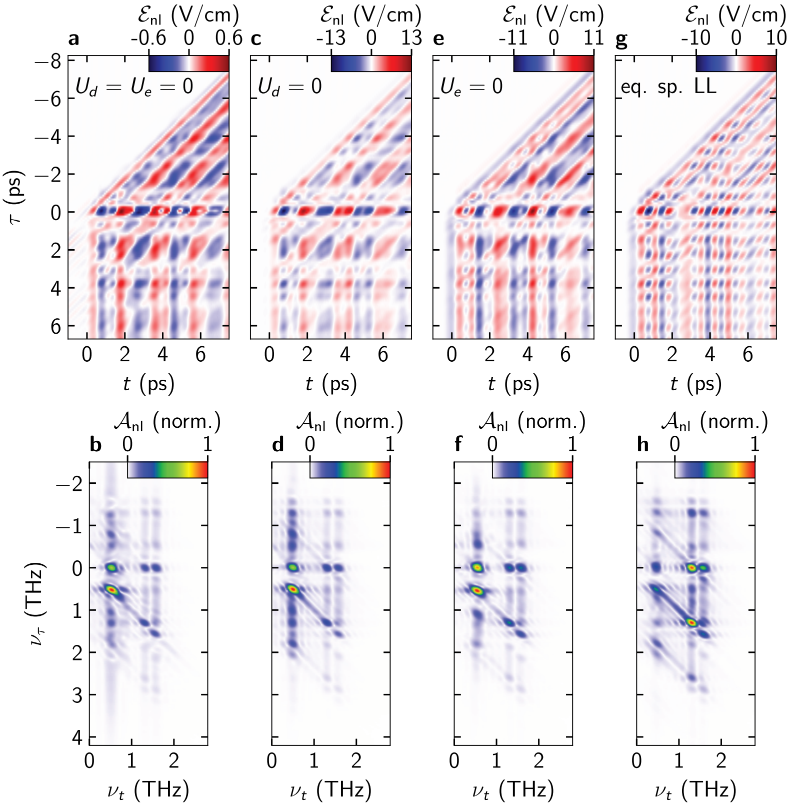

Figure 3.9 | Switch-off analysis of different nonlinearities. a, b, Time-domain calculation and amplitude spectra, normalized to its peak value, for $U_d = U_e = 0$. **c,d**, Calculation for $U_d = 0$. **e, f**, Calculation for $U_e = 0$. **g, h**, Calculation for equally spaced Landau levels. Adapted from [Mor21].

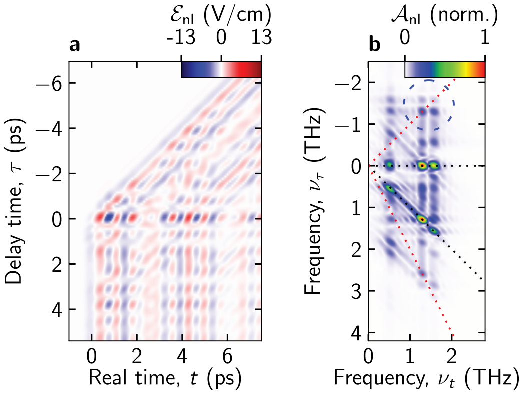

Figure 3.10 | Simulation results. **a**, Calculated response $\mathcal{E}_{\mathrm{nl}}(t, \tau)$ for the sample and excitation scenario in Figure 3.6. **b**, Amplitude spectrum of the data of panel **a**, normalized to its peak value. Adapted from [Mor21].

of GaAs, we obtain a very good match with the experimental data, displaying the same nonlinear field amplitude as well as the spectral weight between the polaritons (Fig. 3.9**g,h**). However, as the slight nonlinearity of the Landau level spacing is known to exist, we include all effects in the simulation for the best match (Fig. 3.10).

In the full calculation including all three nonlinearities (Fig. 3.10), the fast oscillations originating from the UP and DPP resonances as well as the slower modulation induced by the LP resonance are accurately reproduced (compare to Fig. 3.4 and 3.6). Furthermore, the relative and absolute spectral amplitudes of pump-probe and four-wave mixing signals are adequately captured for the individual polaritons, as well as for the nonlinear correlations between separate polariton resonances. The good agreement between theory and experiment is even more evident, when comparing cuts of the datasets for different frequencies ν_t and ν_τ (Fig. 3.11).

For the case of $\nu_\tau = 0$ (Fig. 3.11**b**), the frequencies and amplitudes of the pump-probe responses for the three polariton resonances exhibit a close match between the experimental and theoretical results. Similarly, for the cut along $\nu_\tau = \nu_t$ (Fig. 3.11**c**), the resonances align well, with some deviation caused by spectral broadening of the UP resonance. The cuts along $\nu_\tau = 1.3\,\mathrm{THz}$ and $\nu_\tau = 1.6\,\mathrm{THz}$ (Fig. 3.11**d,e**) once again demonstrate a good agreement in the resonance frequencies between the measured and calculated data. Finally, for completeness, cuts along $\nu_\tau = 0.55\,\mathrm{THz}, 1.3\,\mathrm{THz}$ and $1.6\,\mathrm{THz}$ are shown in Figure 3.11**f-h**.

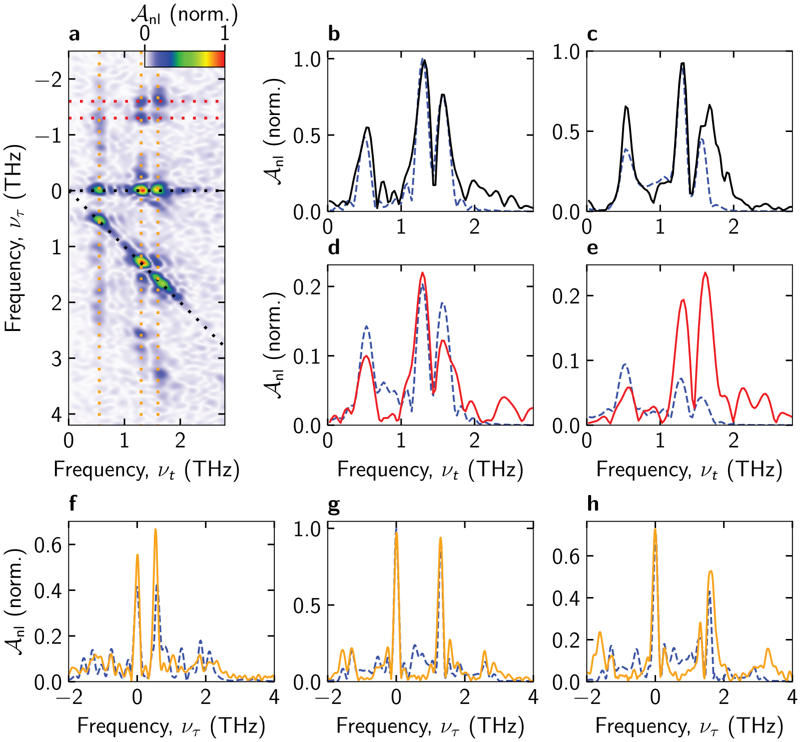

Figure 3.11 | Detailed comparison of experiment and simulation. **a**, Amplitude spectrum $\mathcal{A}_{\rm nl}(\nu_t, \nu_\tau)$ of the time-domain data of Figure 3.6, normalized to its peak value. **b-h**, Amplitude spectra comparing the experimental data (solid curves) and theoretical calculations (dashed blue curves, see also Fig. 3.10), extracted along the dashed lines shown in panel **a** of the same colour. **b**, Spectrum extracted for $\nu_\tau = 0\,\mathrm{THz}$, **c** for $\nu_\tau = \nu_t$, **d** for $\nu_\tau = 1.3\,\mathrm{THz}$, **e** for $\nu_\tau = 1.6\,\mathrm{THz}$, **f** for $\nu_t = 0.55\,\mathrm{THz}$, **g** for $\nu_t = 1.3\,\mathrm{THz}$ and **h** for $\nu_t = 1.6\,\mathrm{THz}$. Adapted from [Mor21].

3.3. Field strength and coupling strength scaling

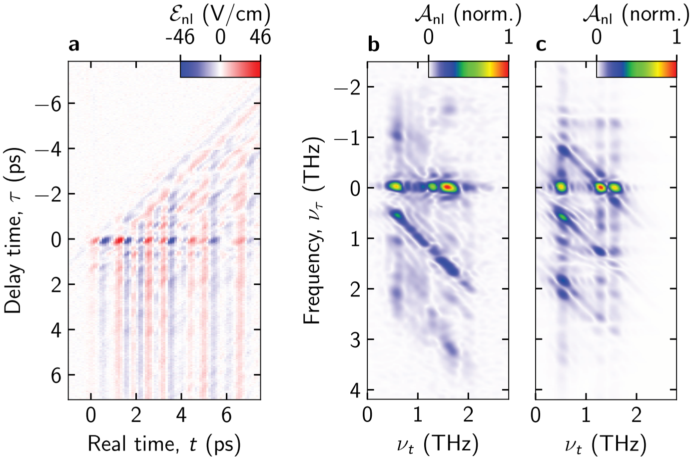

Figure 3.12 | Excitation with a peak field amplitude of pulse B of 5.6 kV/cm. **a**, Experimental response $\mathcal{E}_{\mathrm{nl}}(t,\tau)$. **b**, Amplitude spectrum of the data of panel **a**, normalized to its peak value. **c**, Simulated amplitude spectrum for the excitation scenario of **a** and **b**, normalized to its peak value. Adapted from [Mor21].

Our comprehensive theory successfully describes the creation of distinct resonances through strongly nonlinear interactions of light-matter hybrid modes and significantly expands the parameter space for tailoring deep-strong coupling, a regime that was previously limited to linear interactions with weak probe fields. We further explore the limits of driving our ultrastrongly coupled system with strong coherent fields and conduct additional measurements by doubling the field amplitude of pulse B to approximately 5.6 kV/cm, while keeping the characteristics of pulse A unchanged. Here, the time-domain data show a noticeable reduction in the amplitude of the oscillations of $\mathcal{E}_{\mathrm{nl}}$ along the τ axis (Fig. 3.12**a**), as compared to the data presented in Figure 3.4. The corresponding spectral amplitude $\mathcal{A}_{\mathrm{nl}}$ (Fig. 3.12**b**) exhibits predominantly pump-probe signatures at frequencies $(\nu_\beta, 0)$ and (ν_β, ν_β), where $\beta \in \{\mathrm{LP}, \mathrm{UP}, \mathrm{DPP}\}$. Four-wave mixing signals at $(\nu_\beta, -\nu_\beta)$ and $(\nu_\beta, 2\nu_\beta)$ contribute only weakly to the overall signal. Due to the significantly larger amplitude of pulse B

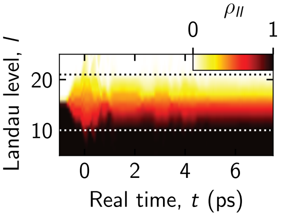

Figure 3.13 | Simulated population with a peak field amplitude of pulse B of 5.6 kV/cm. Population of each Landau level for the setting of Figure 3.12. Dashed lines: threshold energy for longitudinal optical phonon scattering (see text). Adapted from [Mor21].

compared to pulse A, third-order processes involving two photons from pulse B are dominant, which is especially evident when comparing the pump-probe signatures at frequencies of $(\nu_\beta, 0)$ with the signatures at (ν_β, ν_β).

While for the case of excitation with $\mathcal{E}_\mathrm{B} = 2.5\,\mathrm{kV/cm}$, the distribution of excited electrons along the Landau fan covers an energy range slightly below the threshold at which scattering between Landau electrons and longitudinal optical phonons of GaAs becomes possible [Maa16], this is no longer the case for excitation with 5.6 kV/cm. Therefore it is necessary to account for the phonon scattering of these electrons in the simulation and we introduce an additional dephasing time of $T_2 = 100\,\mathrm{fs}$ for Landau electrons excited to Landau levels outside the energy range of $E_\mathrm{F} \pm \hbar\omega_\mathrm{LO}/2$, as indicated by the dashed lines in Figure 3.8**a** and Figure 3.13. Here, E_F represents the Fermi level in equilibrium, and $\hbar\omega_\mathrm{LO} = 36\,\mathrm{meV}$ denotes the energy of the LO phonon [Maa16]. For sufficiently strong excitation, empty Landau states are simultaneously available at $E_\mathrm{F} - \frac{\hbar\omega_\mathrm{LO}}{2}$ and occupied states at $E_\mathrm{F} + \frac{\hbar\omega_\mathrm{LO}}{2}$, allowing for electron-phonon scattering. Including this additional scattering channel, the calculated results, presented in Figure 3.12**c**, accurately reproduce the predominantly incoherent pump-probe nonlinearities observed in the experimental data and reveal that a significant fraction of the total population is excited beyond the threshold for phonon scattering (Fig. 3.13).

To investigate the impact of the coupling strength on the nonlinear response, we additionally measure the nonlinear response of sample S1 (Fig. 2.9). This sample features a lower coupling strength of $\Omega_\mathrm{R}^\mathrm{vac}/\omega_\mathrm{c} = 0.15$. The nonlinear response in the time domain is dominated by long-lived oscillations, modulated by multiple frequencies along the τ axis (Fig. 3.14**a**). Employing a two-dimensional Fourier transform results in the nonlinear amplitude spectrum, as depicted in Figure 3.14**b**.

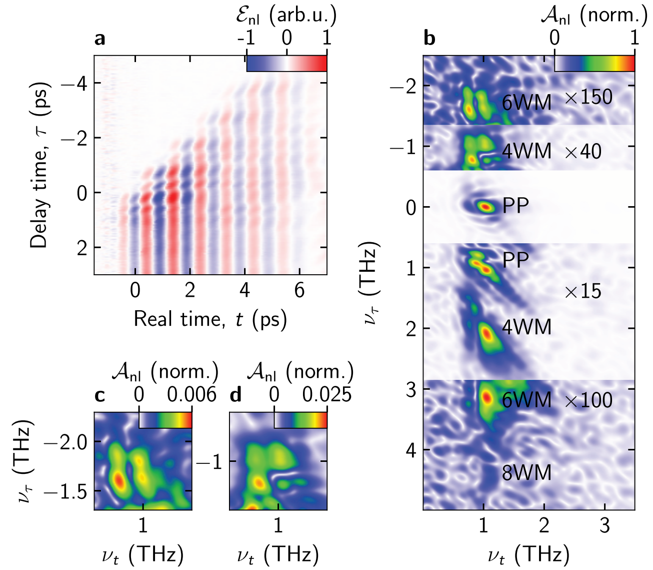

Figure 3.14 | Experimental nonlinear polarization response of the single-QW sample S1, for a peak field amplitude of 9 kV/cm, normalized to its peak value. **a**, Time-domain data $\mathcal{E}_{\mathrm{nl}}(t, \tau)$. **b**, Spectral amplitudes $\mathcal{A}_{\mathrm{nl}}(\nu_t, \nu_\tau)$ obtained from the time-domain data of panel **a**. For each vertical segment, the data are scaled by the specified factor, for better visibility. **c**, Close-up of a group of six-wave and **d**, four-wave mixing signatures. Adapted from [Mor21].

$\mathcal{A}_{\mathrm{nl}}$ again shows pump-probe (PP) signatures at $\nu_\tau = 0\,\mathrm{THz}$, corresponding to the frequencies of the two polariton resonances. In the vicinity of $\nu_\tau = -0.8\,\mathrm{THz}$ and $-1.6\,\mathrm{THz}$, groups of four-wave mixing (4WM) and six-wave mixing (6WM) signatures, respectively, are visible (see Fig. 3.14**c**, **d** for a magnified view). Additionally, around $\nu_\tau = 2.2\,\mathrm{THz}$, $3.2\,\mathrm{THz}$, and $4.6\,\mathrm{THz}$, 4WM, 6WM, and even a faint eight-wave mixing (8WM) signature emerge, respectively. Again, strong nonlinearities mixing the LP and the UP resonances emerge for the 4WM and 6WM signal. Despite the significantly higher driving field amplitude of 9 kV/cm, this structure S1 seems to offer a higher degree of coherence, resulting in the visibility of higher order nonlinearities.

Conclusion

In summary, the presented data explore a novel regime of ultrastrong light-matter coupling, where the subcycle polarization dynamics of the electronic system are not only driven by vacuum fluctuations, but at the same time by a strong coherent external field. This non-perturbative excitation results in the emergence of new pump-probe and coherent multi-wave mixing nonlinearities, connecting the polarization of different, individual polaritons. These nonlinearites, inaccessible through linear spectroscopy, provide evidence of the dynamical breaking of the normal-mode approximation in a strongly out-of-equilibrium situation. The large design space for ultrastrong light-matter coupling allows us to custom-tailor and resonantly enhance these nonlinearities, where neither the light nor the matter subsystem has resonances. Access to these previously unexplored degrees of freedom within cavity-QED has the potential to unveil quantum phenomena akin to the strong coupling regime of cavity-QED, where Bose-Einstein condensates or quantum fluids of light have been successfully generated [Car13]. Controlling the nonlinear response of an ultrastrongly coupled system can aid in the generation of squeezed quantum states of light, as well as enhancing ground-state instabilities and phase transitions in superconductivity [Sch19], control cavity chemistry [Hut12, Chi16, Tho19, Dun22], and vacuum-modified electronic transport [Org15, PB19, Val21, App22]. Furthermore, if improving the nonlinear response is possible and results in significant modulation of the coupling strength, even the detection of quantum vacuum radiation from periodic modulation is feasible [Lib07].

Chapter 4

Tailoring light-matter coupling through spatial matter design

With the pursuit of larger and larger coupling strengths extending into the deep-strong coupling regime, the splitting of the polariton doublet, $2\Omega_{\mathrm{R}}$, occupies a larger and larger spectral bandwidth. Consequently, as already evident in the previous chapter, coupling to other light or matter modes comes into play. Yet usually the theoretical models to describe the coupling (except the one used in the previous chapter) only consider the interaction between a single optical mode and a single matter excitation.

However, the interactions with off-resonant light and matter modes are often significant and cannot be neglected, even for modest coupling strengths. Moreover, as will be shown in this chapter, these additional interactions offer novel routes for tailoring light-matter coupling, allowing us to suppress or enhance specific coupling pathways, establish coupling of formerly orthogonal modes, and reshape the polariton modes. The regime of multi-mode coupling is called multi-mode strong-coupling (MMSC) or very strong coupling (VSC) regime. While we already included coupling to a second cavity mode into our description of the system in the previous chapter, we will now explore the parameter space offered by multi-mode coupling systematically.

The coupling of multiple matter modes to a single cavity mode (VSC) will be analysed in the next chapter 5. In this chapter we will explore the coupling of two different cavity modes to one matter resonance (MMSC). Theory support for the results described in this chapter was provided by Erika Cortese and Simone De Liberato. The theoretical findings are published in *Optica* [Cor23]. A second publication, focussing on the experimental data is submitted [Mor23b].

While both, the VSC and MMSC multi-mode regimes have been reached by multiple systems already [Sun15, Bay17, Bro17, Cor21, Raj21, Bal21], their potential to tailor the properties of light-matter coupling has been largely neglected. Every light-matter coupled system and its properties are fundamentally defined by the overlap integrals of the electric field modes and the matter polarization fields. Multi-mode coupling allows one to advance beyond simply maximising the overlap of two fields and offers a large accessible design space to shape the coupling by taking the specific subwavelength spatial structure of each mode into account. In similarity to selection rules of classical optics, one can now select specific coupling pathways, establish coupling of formerly orthogonal modes, and shape the frequency response and magnetic tuning of the polariton modes.

4.1. Light-matter coupling with non-orthogonal light modes

In order to examine the effects of multi-mode coupling, we first have to extend the description of light-matter coupling given in chapter 2.1 to include multiple light and matter modes, as well as the (fractional) overlap of all these modes. While one can generally assume, that the modes of a cavity are orthogonal within the full three-dimensional space, this does not generally hold true in a limited sub-volume (Fig. 4.1). This fact is important for our coupled samples, as for the coupling we only consider the cavity fields in the limited volume of the QW stack. Therefore, generally, cavity modes can become non-orthogonal in the QW subspace, and we have to include this fractional overlap in our theory description of the coupled system. The full detailed deviation of the Hamiltonian including these effects by Erika Cortese and Simone De Liberato will be included in appendix E. The resulting bosonic Hamiltonian (in Coulomb gauge) then reads:

$$\hat{H} = \hat{H}_{\mathrm{c}} + \hat{H}_{\mathrm{cyc}} + \hat{H}_{\mathrm{int}} + \hat{H}_{\mathrm{dia}}, \tag{4.1}$$

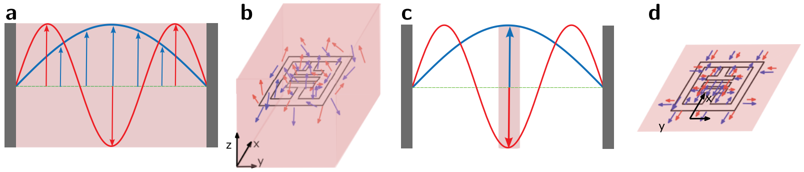

Figure 4.1 | Orthogonal and non-orthogonal modes. **a**, Two lowest modes of a resonator (red, blue), orthogonal respective to the complete mode volume. **b**, Two modes of a planar microresonator, orthogonal respective to the complete 3D space. **c, d**, Identical modes from panels **a** and **b** overlap respective to a limited volume. Adapted from [Cor23].

with

$$\hat{H}_{\mathrm{c}} = \sum_j \hbar\omega_j \left(\hat{a}_j^\dagger \hat{a}_j + \frac{1}{2}\right), \tag{4.2}$$

$$\hat{H}_{\mathrm{cyc}} = \sum_\alpha \hbar\omega_c \left(\hat{b}_\alpha^\dagger \hat{b}_\alpha + \frac{1}{2}\right), \tag{4.3}$$

$$\hat{H}_{\mathrm{int}} = \sum_j \sum_{\alpha \leq j} \hbar \left[\left(\Omega_{\mathrm{R},j,\alpha} b_\alpha + \Omega^*_{\mathrm{R},j,\alpha} b^\dagger_\alpha\right)\left(\hat{a}_j^\dagger + \hat{a}_j\right)\right], \tag{4.4}$$

$$\hat{H}_{\mathrm{dia}} = \sum_j \sum_{j'} h_{j,j'} \left(\hat{a}_j^\dagger + \hat{a}_j\right)\left(\hat{a}_{j'}^\dagger + \hat{a}_{j'}\right), \tag{4.5}$$

and coupling parameters

$$\Omega_{\mathrm{R},j,\alpha} = \sqrt{\frac{\omega_c N_{\mathrm{QW}} \rho e^2}{2m^* \epsilon_0 \bar{\epsilon} \omega_j \mathbb{V}_j}}\,\alpha_{j,\alpha}, \tag{4.6}$$

$$h_{j,j'} = \sum_{\gamma \leq j,j'} \frac{\hbar \Omega^*_{\mathrm{R},j,\gamma} \Omega_{\mathrm{R},j',\gamma}}{\omega_c}. \tag{4.7}$$

Here the Hamiltonian features the same four parts as in chapter 2.1, $\hat{H}_{\mathrm{c}}$, $\hat{H}_{\mathrm{cyc}}$, $\hat{H}_{\mathrm{int}}$ and $\hat{H}_{\mathrm{dia}}$. Now we describe j cavity modes with individual frequencies ω_j in $\hat{H}_{\mathrm{c}}$ and α frequency degenerate matter modes with frequency ω_{c} in $\hat{H}_{\mathrm{cyc}}$. The interaction and diamagnetic parts of the Hamiltonian, $\hat{H}_{\mathrm{int}}$ and $\hat{H}_{\mathrm{dia}}$, then describe interactions between all j cavity and α matter modes.

The coupling is characterized by the vacuum Rabi frequencies, $\Omega_{\mathrm{R},j,\alpha}$, which quantify the spatial mode overlap and represent the mutual interaction between modes j and α. They also take into account the interactions resulting from the non-orthogonality of modes within the limited subspace of the interaction, specifically the quantum well plane. $\mathbb{V}_j$ represents an effective mode length in the z-direction, which is determined by dividing the mode volume in the three-dimensional domain by the mode integral over the two-dimensional plane of the electron gas. The background dielectric constant in the quantum well plane is denoted by $\bar{\epsilon}$, m^* is the effective mass of the electrons and $N_{\mathrm{QW}}\rho$ denotes the number of QWs times their individual 2D density. The overlap matrix is contained in $\alpha_{j,\alpha}$. Note that the approximation of multiple degenerate matter modes with frequency ν_{c} does not hold true for systems, which have ultra-narrow features in the resonator or QW structure. Here one has to incorporate the dispersion of the matter system and as such multiple different matter resonances.

For two photonic modes, we consider, generally, two different spatial mode distributions in the QW plane. Thus, we also need to account for two degenerate matter modes and obtain three parameters, containing the overlap parameter $\tilde{\eta}_{2,1}$, which assumes values between 0 and 1:

$$\Omega_{\mathrm{R},1,1} = \sqrt{\frac{\omega_c \rho e^2}{2m^* \epsilon_0 \epsilon_r \omega_1 \tilde{\mathbb{V}}_1}}, \tag{4.8}$$

$$\Omega_{\mathrm{R},2,1} = \sqrt{\frac{\omega_c \rho e^2}{2m^* \epsilon_0 \epsilon_r \omega_2 \tilde{\mathbb{V}}_2}} \tilde{\eta}_{2,1}, \tag{4.9}$$

$$\Omega_{\mathrm{R},2,2} = \sqrt{\frac{\omega_c \rho e^2}{2m^* \epsilon_0 \epsilon_r \omega_2 \tilde{\mathbb{V}}_2}} \sqrt{1 - |\tilde{\eta}_{2,1}|^2}. \tag{4.10}$$

Here the photonic mode $j = 1$ is coupled exclusively to the matter mode $\alpha = 1$ and the coupling of the second photonic mode $\alpha = 2$ is shared between both matter modes. For $\tilde{\eta}_{2,1} = 0$, the coupled system separates into two non-interacting subsystems, each described by the Hamiltonian introduced in chapter 2.1.

The change in cavity overlap manifests in multiple distinct changes in the spectral response of the polaritons. In Figure 4.2 we illustrate three characteristic cases for two photonic modes with frequencies of 1 THz and 2 THz, respectively: no overlap ($\tilde{\eta}_{21} = 0$, Fig. 4.2**a**,**b**), medium overlap ($\tilde{\eta}_{21} = 0.5$, Fig. 4.2**c**,**d**), and full overlap ($\tilde{\eta}_{21} = 1$, Fig. 4.2**e**,**f**). In each panel, the data on the left displays the polariton

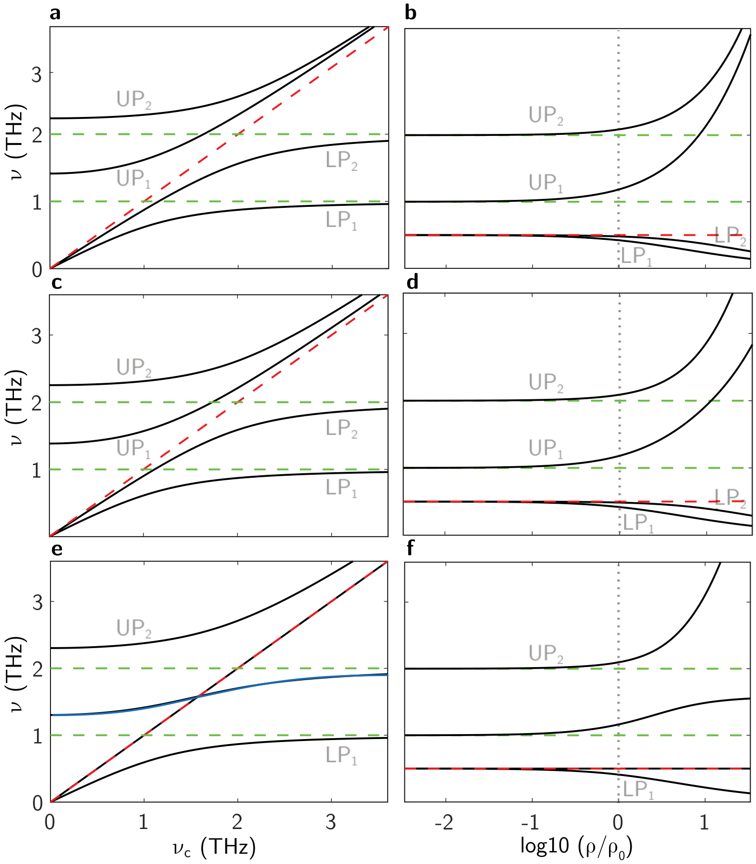

Figure 4.2 | Polariton frequencies with overlapping cavity modes, a, as a function of the cyclotron frequency ν_c and **b**, as a function of the relative QW doping density ρ/ρ_0 for no overlap, **c, d**, partial overlap and **e, f**, full overlap. Bare cavity frequencies are marked with green and the cyclotron frequency with a red dashed line. The grey dashed lines in **b, d, f** mark the doping density ρ_0, used in **a, c, e**. Adapted from [Cor23].

frequencies as a function of the cyclotron frequency ω_c and on the right as a function of the relative QW doping density ρ/ρ_0, whereby the latter shows the frequencies as a function of coupling strength.

Looking at the cyclotron frequency plots on the left, for the case of no or partial overlap (Fig. 4.2**a,c**), we observe four modes, which we identify as a two pairs of a lower polariton and an upper polariton, each with their distinct polariton splitting. However, when $\tilde{\eta}_{21} = 1$, an S-shaped resonance appears instead of the LP_2 and the UP_1 resonance. This S-shape is a manifestation of the fundamental change of the character of the coupling, as now a single matter excitation mode ($j = 1$) simultaneously couples to both photonic modes ($\alpha = 1, 2$), reducing the number of participating modes from four to three. Consequently, this results in three polariton branches in total, where the middle-energy branch is confined between the frequencies of both cavity modes, ω_1 and ω_2 and exhibits a double-mode nature. Additionally, the panels showing the polariton frequencies, as a function of the electron density ρ (Fig. 4.2**b,d,f**), highlight the effects of the overlap on the diamagnetic contributions. For no overlap (Fig. 4.2**b**), two modes, the two upper polaritons, UP_1 and UP_2, experience the blue-shift from the respective diamagnetic term with increasing electron density. This behaviour is also still present for the case of partial overlap (Fig. 4.2**d**), yet the diamagnetic term causes the two upper polaritons to slightly repel each other. The two lower polaritons do not change significantly. For perfect overlap (Fig. 4.2**f**), this repellence between the two UPs dominates, resulting even in an anticrossing behaviour of the UPs above a critical value of the electron density. This behaviour also assures that the S-shaped mode never crosses its bare components. As a result of the reduced number of coupled modes, the LP_2 mode is replaced by an uncoupled mode representing the bare cyclotron resonance.

4.2. Mode-shaping via subwavelength structuring of the electronic medium

In order to explore the implications of light-matter coupling with multiple and non-orthogonal cavity modes, we utilize our established Landau-polariton structures. This will allow us to demonstrate the additional tailoring capabilities, allowing for

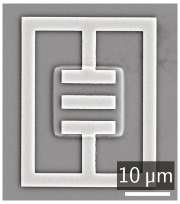

Figure 4.3 | Subwavelength structuring of the QWs. Scanning electron microscope picture of a single double gap resonator fabricated on top of the GaAs substrate, and the QW patch hosting the cyclotron resonances.

control of the spectral shape of multiple polariton resonances as well as boosting or suppressing coupling of certain modes. In order to change the spatial overlap of the cavity modes and the electronic system, we perform subwavelength structuring of the electronic medium. We again use the double gap resonators coupled to the cyclotron resonances of Landau-quantized 2DEGs in our QWs, but in two different configurations. A reference sample implements a planar quantum well stack covering the whole unit cell area, as introduced in chapter 2.4 and is referred to as *unstructured* (S3unstr). A second sample, referred to as *structured* (S3str), features laterally etched, quadratic QW patches, resulting in additional lateral confinement (Fig. 4.3). The reduced QW area then controls the spatial overlap with the resonator modes. Both sample structures feature 3 QWs with a thickness of 20 nm, AlGaAs barriers of 25 nm and a doping density of $\rho = 1 \times 10^{12}\,\mathrm{cm}^{-2}$, per QW. The patches of the *structured* sample are fabricated by wet-etching with a temporary mask before the resonators are added to the structure and feature a side length of 15 µm. Hereby the central gap region of the resonators is aligned with the etched patches (Fig. 4.3).

THz transmission of the samples is recorded as a function of the cyclotron frequency ν_c using the same setup utilized in previous experiments and outlined in chapter 2.3. The spectra for the *unstructured* sample are shown in Figure 4.4**a** and exhibit five resonances. The diagonal resonance at $\nu = \nu_\mathrm{c}$ (red dashed line) corresponds to the cyclotron resonance in the uncoupled regions of the structure between the resonators. The remaining four modes arise from the coupling between the different light and matter modes, displaying the characteristics of one-to-one coupling of photonic modes to matter excitations, which are orthogonal to each other. The coupling to the LC mode at $\nu_\mathrm{LC} = 0.8\,\mathrm{THz}$ results in the LP_1 mode and a UP_1 mode, which start at frequencies of 0 THz and 0.9 THz for $\nu_\mathrm{c} = 0\,\mathrm{THz}$, respectively. With increasing cyclotron frequency, they exhibit the expected anti-crossing shape. Similar,

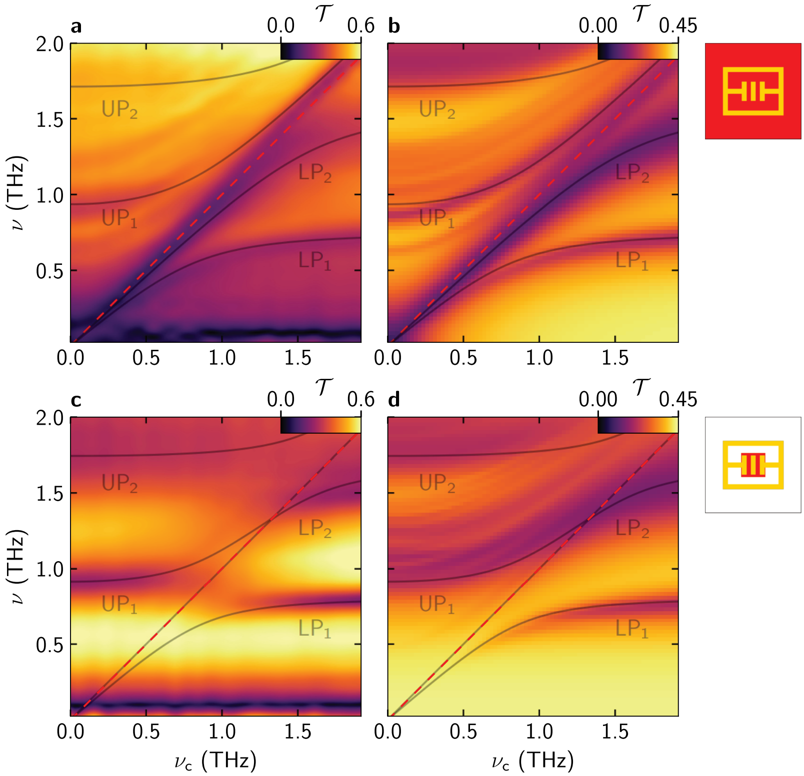

Figure 4.4 | Tailoring of the modal overlap. **a**, Experimental transmission of structure S3unstr, featuring a complete QW film, as a function of the cyclotron frequency, ν_c. Dashed red line: bare cyclotron resonance. transparent lines: polariton modes fitted with the multimode Hamiltonian. **b**, Respective finite-element frequency-domain simulation of the structure with an adjusted doping density of $\rho = 1.25 \times 10^{12}\,\mathrm{cm}^{-2}$, per QW. Pictogram on right: double gap resonator in unit cell and unstructured QW (red). **c**, Experimental transmission of sample S3str, featuring the quadratic QW patches. **d**, Respective simulation. Pictogram on right: double gap resonator in unit cell and structured QW patch (red).

for the coupling to the second resonator mode with a frequency of $\nu_{\mathrm{DP}} = 1.6\,\mathrm{THz}$, the corresponding LP_2 mode branches off from the cyclotron resonance near $\nu_\mathrm{c} \approx 1.2\,\mathrm{THz}$, while the associated UP_2 mode resides at $\nu = 1.75\,\mathrm{THz}$ for $\nu_\mathrm{c} = 0\,\mathrm{THz}$.

Subsequently, the *structured* sample is measured (Fig. 4.4**c**). Here the resonator can only couple to the QW patch in the central gap region of the resonators (see Fig. 4.4 right). In stark contrast, the resonances previously associated with the upper polariton of the LC mode (UP_1) and the lower polariton of the DP mode (LP_2) merge into one S-shaped mode, predicted for a strong overlap of both photonic modes. Thus, we only observe three coupled modes instead of four. This mode starts at a frequency of $0.92\,\mathrm{THz}$ for $\nu_\mathrm{c} = 0\,\mathrm{THz}$ and stays approximately constant up to $\nu_\mathrm{c} = 0.7\,\mathrm{THz}$, beyond which the frequency increases until reaching an inflection point at $\nu_\mathrm{c} = 1.25\,\mathrm{THz}$. A further increase in ν_c leads to the convergence towards $\nu = 1.6\,\mathrm{THz}$. Due to the modified spatial overlap, the frequencies of the other coupled resonances (LP_1, UP_2) differ as well. We confirm the measurements with our fit-free finite-element frequency-domain simulations (see appendix C). The resulting transmission spectra match the experimental data and validate the results (Fig. 4.4**b,d**).

To extract the coupling parameters, we use the multi-mode Hamiltonian to fit both the experimental and simulated datasets with the effective mode lengths $\tilde{\mathbb{V}}_j$ as free fit parameters (black curves in Fig. 4.4). The overlap parameter $\tilde{\eta}_{2,1}$ is calculated from the electric near-field distribution of the resonator modes. The fits match the observed polariton modes and confirm the main difference of our datasets - the S-shaped mode is only present for the *structured* sample. Comparing the resulting overlap factors, for the *unstructured* sample we obtain $\tilde{\eta}_{2,1} = 0.15$ and for the *structured* one $\tilde{\eta}_{2,1} \approx 1$, respectively. While both structures feature a large overlap of the photonic modes, only the almost perfect overlap for the *structured* sample results in an S-shaped mode. This increase in overlap of the photonic modes is expected, as reducing the QWs to the patch in the central resonator area eliminates coupling opportunities elsewhere. Specifically, the DP cavity mode features significant field enhancement at the edges of the double gap resonator. For the structured sample, there is no QW present, and hence, coupling to the DP mode is no longer possible at the outer edges of the resonator.

Furthermore, this change of the shape of the magnetic field dependence of the polaritons is accompanied by a reduction in the polariton splitting and the diamagnetic shifts. Here the fit shows reduced normalized coupling strengths. For the first cavity mode, the normalized coupling strength $\Omega_{\mathrm{R},1,1}/\omega_1$, evaluated at resonance $\omega_j = \omega_\mathrm{c}$, is reduced to 0.28, while for the second cavity mode, $\Omega_{\mathrm{R},2,2}/\omega_2$ is decreased to 6×10^{-3} and $\Omega_{\mathrm{R},2,1}/\omega_1$ is increased to 0.27. In comparison, the unstructured case exhibits larger overall normalized coupling strengths of $\Omega_{\mathrm{R},1,1}/\omega_1 = 0.37$, $\Omega_{\mathrm{R},2,2}/\omega_2 = 0.21$, and $\Omega_{\mathrm{R},2,1}/\omega_1 = 0.07$. This overall reduction can be attributed to the decrease in the integration area for the photonic modes, which results in a larger normalized mode length $\mathbb{V}_j$ and consequently leads to a smaller coupling strength. At the same time, the negligible value of $\Omega_{\mathrm{R},2,2}/\omega_2$ for the structured sample is a direct consequence of an almost perfect overlap factor. Surprisingly, structuring the QW leads to an increase in the ratio between the coupling strengths of the DP and LC cavity modes from 0.19 to 0.96, thereby increasing the weight of the DP coupling. This change in coupling strengths demonstrates our capability to take back control of the selection of modes that couple to each other and suppress or enhance specific coupling pathways by near-field structuring of the electronic medium. Additionally, we can utilize this ultrastrong coupling of two cavity modes to the same matter mode to mediate coupling of the formerly non-interacting cavity modes.

4.3. Plasmon formation in structured quantum wells

Spatial structuring of the electronic medium allows for shaping the interacting modes and thus opens up new pathways for tailoring light-matter coupling. However, our assumption of degenerate matter modes with frequency ω_c, independent of the spatial distribution, is only accurate for structures that do not contain features significantly smaller than the wavelength in the resonator geometry or the QW structuring. When subwavelength structures are present, a thorough analysis of the matter system is required as additional confinement can require taking plasmonic resonances into consideration.

The simplest case for additional confinement of our QW stack is the structuring into stripes. Here the confinement of the 2DEG in one additional direction, given by the stripe width L, creates a plasmon resonance in the structured direction. The

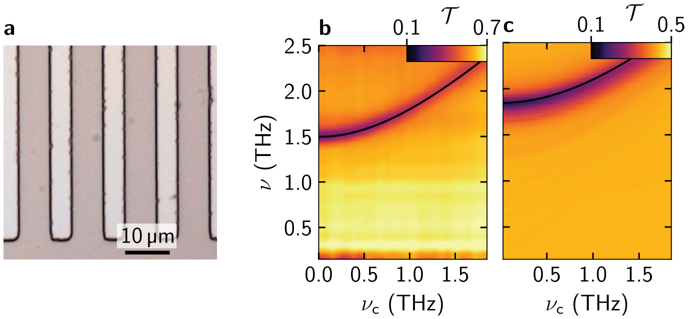

Figure 4.5 | Stripes of a 6 QW sample Str6. **a**, Light microscope picture of the stripes with a width of $L = 4.8\,\mu\mathrm{m}$ and spaced $7\,\mu\mathrm{m}$ apart. **b**, THz transmission of the sample as a function of the cyclotron resonance, ν_c. Black line: Fit of the resonance with the Equation 5.2, for $\boldsymbol{q}_\parallel = \frac{2\pi}{L}$ adjusted with $\epsilon_\mathrm{eff} = 9.7$ and $\rho = 1.15 \times 10^{12}\,\mathrm{cm}^{-1}$ for the experiment and **c**, simulation with $\rho = 1.75 \times 10^{12}\,\mathrm{cm}^{-1}$.

frequency of the resonance scales according to $\nu_\mathrm{plasmon} \propto \sqrt{\rho L^{-1}}$ [Mur20]. When applying the external magnetic field, the plasmon resonance will hybridize with the cyclotron resonance ν_c, forming a magnetoplasmon resonance with frequency $\nu_\mathrm{MP} = \sqrt{\nu_\mathrm{plasmon}^2 + \nu_\mathrm{c}^2}$ [Kus01, Mur20]. Further details on plasmons in 2DEGs will also be discussed in the next chapter.

To experimentally verify the formation of a plasmon resonance in QW stripes we structure a sample featuring 6 QWs (sample Str6), each with a doping density of $\rho = 1.15 \times 10^{12}\,\mathrm{cm}^{-2}$, into stripes with a width of $L = 4.8\,\mu\mathrm{m}$ and a spacing of $7\,\mu\mathrm{m}$ (Fig. 4.5**a**). Figure 4.5**b,c** shows the resulting experimental and simulated transmission as a function of ν_c, whereby the sample is probed with THz pulses polarized perpendicular to the stripes. For $\nu_\mathrm{c} = 0\,\mathrm{THz}$, the bare plasmon mode features a frequency of $\nu_\mathrm{plasmon} = 1.5\,\mathrm{THz}$, subsequent hybridisation with the cyclotron resonance results in an increase in frequency, asymptomatically approaching the cyclotron resonance with increasing ν_c. This change shifts the accessible matter frequency range from $\geq 0\,\mathrm{THz}$ to $\geq 1.5\,\mathrm{THz}$ and consequently does not allow for resonant coupling to the LC mode of the double gap resonator (see Fig. 2.7).

For the case of light-matter coupling with structured QW patches, as employed for controlling the modal overlap (see Fig. 4.4 and Fig. 4.6**a**), the situation is further

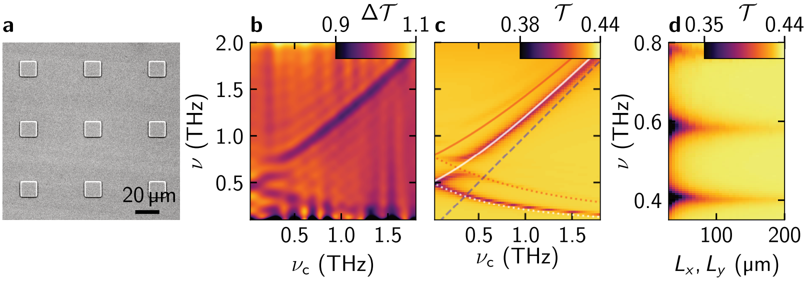

Figure 4.6 | Square patches with a side length of 15 µm with 3 QWs, each with $\rho = 1 \times 10^{12}\,\mathrm{cm}^{-1}$ (sample S3pat). **a**, Scanning electron microscope picture of the patches. **b**, Experimental differential THz transmission. **c**, Simulated transmission, with marked cyclotron resonance (dashed line), bulk (solid lines) and edge (dotted lines) magnetoplasmon modes for the first two plasmon modes. **d**, Sweep of the simulation unit cell size L_x, L_y at a frequency of $\nu_c = 0.25\,\mathrm{THz}$.

complicated by additional confinement in both directions of the QW plane. The transmission spectra of the bare square patches with a side length of 15 µm (S3pat, as used for sample S3str) as a function of the cyclotron resonance (Fig. 4.6**b**) display a rich structure with multiple anti-crossing modes. The finite-element frequency-domain simulations of the structure match the experimental results (Fig. 4.6**c**). For $\nu_c = 0\,\mathrm{THz}$, the plasmon modes for both confinement directions are degenerate and orthogonal, resulting in a fundamental plasma mode with a frequency of 0.5 THz. Higher plasmon modes are present, even though they feature a much lower oscillator strength. Upon activating the external magnetic field, hybridization with the cyclotron resonance occurs. Due to the confinement in two dimensions, each plasmon splits into two modes, a bulk magnetoplasmon and an edge magnetoplasmon. With increasing cyclotron frequency, the bulk magnetoplasmon rises in frequency and asymptotically approaches the bare cyclotron frequency, whereas the edge magnetoplasmon asymptotically approaches zero frequency. This phenomenon has been first observed in disk geometries [All83, Mas85] and has been studied and theoretically modelled for a variety of 2DEG systems [Gla85, Fet86, Mur20]. For the length scales and 2DEG properties employed here, the magnetic field dependence of the bulk and

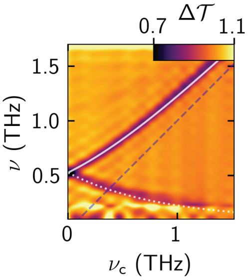

Figure 4.7 | QW disks with a diameter of 15 µm with 3 QWs, each with $\rho = 1 \times 10^{12}\,\mathrm{cm}^{-1}$. Experimental differential THz transmission, with marked cyclotron resonance (dashed line), bulk (solid line) and edge (dotted line) magnetoplasmon mode for the first plasmon mode.

edge magnetoplasmon modes is given by [Mur20]

$$\omega_{\mathrm{MP}\pm} = \frac{\omega_c}{2} \pm \sqrt{\frac{\omega_c^2}{4} + \omega_{\mathrm{plasma}}^2} \tag{4.11}$$

The bare cyclotron resonance (dashed blue line) as well as the bulk magnetoplasmon (solid lines) and edge magnetoplasmon (dotted lines) modes for the first two plasmon modes with bare frequencies of $\omega_{\mathrm{plasma}} = 0.5\,\mathrm{THz}$ (white lines) and $\omega_{\mathrm{plasma}} = 0.78\,\mathrm{THz}$ (red lines), are plotted in Figure 4.6**b**, respectively. Yet, this magnetic field dependence does not include the observed pronounced anti-crossing of the first bulk magnetoplasmon mode and the second edge magnetoplasmon mode at $\nu_c \approx 0.25\,\mathrm{THz}$. While there is a plethora of studies on disk geometries, none of them observes the anti-crossing of the modes, as the edege and bulk magnetoplasmon modes are normal modes, which do not interact. This absence of the anti-crossing in disk geometries is also confirmed by a measurement of a QW disk with a diameter of 15 µm and otherwise identical parameters as our QW patches (Fig. 4.7). Only one study [Dem90] observes a similar anti-crossing in smaller, but rectangular structures. Here matching theory suggests two possible explanations: many-body effects and coupling of adjacent patches [Hua91]. Conducting a systematic sweep of the unit cell side length of the patch simulations, ranging from 30 µm to 200 µm in an additional simulation, shows no observable change of the splitting (Fig. 4.6**d**). In conjunction with the absence of an anti-crossing point in the matching disk geometry, it seems that the coupling of the modes is introduced by the geometry of the patch itself.

Certainly, the influence of these effects on the matter system must be taken into account to achieve a precise characterization of the *structured* samples. As implied by its name, the edge magnetoplasmon mode primarily localizes at the edge of the QW patch, where the field enhancement of the resonator is considerably diminished and thus the coupling to the edge magnetoplasmon mode is minimal and can be neglected. Consequently, the spectrum in the frequency range utilized for coupling is predominantly governed by a solitary mode, namely the first bulk magnetoplasmon mode. The strong deviation of the bulk magnetoplasmon resonance from the bare cyclotron resonance is limited to the region $\nu_\mathrm{c} < 0.5\,\mathrm{THz}$, while for $\nu_\mathrm{c} > 0.5\,\mathrm{THz}$ the increase in frequency shifts the polaritons modes slightly.

Conclusion

In summary, the exploration of multi-mode coupling offers a largely uncharted parameter space for controlling light-matter interactions. The developed, comprehensive theory allows for the incorporation of the non-orthogonality of multiple confined THz resonator modes, coupled to the cyclotron resonance of a 2DEG. Through lateral confinement of the QW, we gain the ability to manipulate spatial overlap factors, thereby customizing the characteristics of the polariton modes. Surprisingly, the alterations in the overlap exert a substantial influence on the polariton properties, including their frequencies, magnetic field dependence, coupling strength, and even spatial field distribution, all without modifying the cavity itself (see also [Cor23]). This capability facilitates the suppression or enhancement of specific coupling pathways of certain cavity or matter modes, similar to the selection rules in classical optics. Furthermore, shaping the QWs enables tailoring the coupling between former non-interacting cavity modes, through a common matter resonance. This versatile toolkit for manipulating the coupling between multiple photonic and electronic modes opens up more possibilities for tuning the polaritons of polariton-based devices for a wide range of applications in areas such as optoelectronics and nanophotonics.

Chapter 5

Deep-strong multi-mode, multi-octave coupling

Increasingly stronger light-matter coupling and the consequent rise in vacuum photon populations have opened exciting possibilities for exotic effects of cavity QED. Thus far, the primary focus has been on optimizing resonant light-matter interactions. While previous investigations have showcased remarkable progress in this direction, they also discovered fundamental barriers arising from light-matter decoupling [DL14] or dissipation [Raj21]. With increasing coupling strengths pushing into deep-strong coupling, the very strong coupling regime will almost invariably come into play, rendering the single-mode approximation inadequate.

In chapter 4, we explored the influence of multiple cavity modes coupling to the same matter resonance in a setting featuring modest coupling strengths within the USC regime. However, as illustrated in chapter 4.3, as electron densities in the 2DEG increase and the coupling strength grows, multiple non-degenerate matter modes may also be involved. While the dipole moment of a solitary resonant excitation can only be augmented to a certain extent, thereby setting a limit to the attainable coupling strength, this barrier can be overcome by coupling to multiple strong dipole moments with differing frequencies and even of different resonance types. This chapter will show how coupling multiple matter modes to one photonic mode enables us to exceed previous coupling strength records and achieve coupling strengths deep in the DSC regime, while providing novel opportunities for customising light-matter coupling.

The concept of off-resonant, multi-mode coupling exploits the fact that when there is a sufficiently strong spatial overlap between light and matter polarization fields, even matter resonances, considerably detuned from the optical resonance, can substantially boost the vacuum ground state population (discussed in this chapter later). Consequently, multiple non-resonant plasmon modes can be cooperatively coupled to a shared resonator mode, leading even to the mixing of formerly orthogonal electronic excitations. By harnessing this principle of non-resonant multi-mode coupling, this chapter will demonstrate how an ultrabroadband spectrum of more than 10 cavity polaritons spanning 6 optical octaves and a vacuum ground state population exceeding 1 photon can be created, surpassing previous records almost threefold. The results presented in this chapter were submitted as an article to a peer-review journal and are available as a preprint (see [Mor23a]).

5.1. Irreducible compact resonator array

We begin our design process of the coupled structures by reevaluating the resonator geometry to enhance its performance. Our strategy involves not only capitalizing on coupling to multiple non-resonant plasmon modes to amplify the virtual photon number per resonator structure but also focusing on optimizing the metasurface resonator geometry to achieve a higher density of individual resonators. By increasing the density of resonators, we effectively boost the overall virtual photon density in the system. The resulting metasurface eliminates the excess spacing between adjacent resonators, resulting in a four-fold increase in the areal resonator density, while maintaining the oscillator strength, well-separated optical modes, linewidths, high near-field enhancement factors, and low mode volumes of the original design. To achieve this optimization, we revisit the established design principles for our resonator structures and discard the design rule of generously spaced resonators to avoid nearest-neighbour couplings. We start with a well-established inverted resonator structure [Che07, Sca12, Bay17, Die20], featuring a square shape with an outer extension of 30 µm, embedded in a unit cell size that is twice as large as the outer dimensions of the resonator (Fig. 5.1**a**). The design features two symmetric current paths feeding a central capacitive gap with a width of 2.5 µm. The structure features five optical modes with centre frequencies at 0.52, 1.95, 3.75, 4.6, and

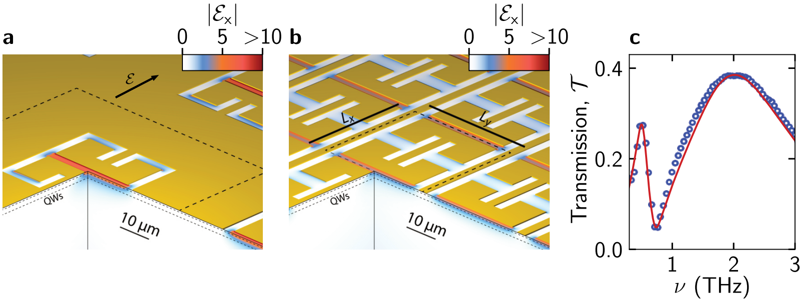

Figure 5.1 | Ultracompact metasurface. **a**, Three-dimensional cut-away illustration of a conventional metasurface structure (gold shape) and its electric near-field distribution $|\mathcal{E}_x|$ for the fundamental LC mode at $\nu = 0.5\,\mathrm{THz}$. The unit cell (size: $60\,\mu\mathrm{m} \times 60\,\mu\mathrm{m}$) is indicated by the dashed line. QWs: quantum well stack. **b**, Highly compacted metasurface with a unit cell size of $L_x \times L_y = 30\,\mu\mathrm{m} \times 32.5\,\mu\mathrm{m}$ (butterfly). **c**, Measured THz transmission of the bare resonator array (blue circles), and calculation (red curve). Adapted from [Mor23a].

6 THz (see Fig. 5.1**c** and 5.4**b**) for the excitation by THz radiation linearly polarized perpendicular to the capacitive gap.

Exciting the fundamental mode at 0.52 THz, an oscillating current flows along the paths indicated in Figure 5.2**a**. Charge carriers on the right inner metal plate are transported to the outside of the structure (turquoise right arrow) while a current, identical in both magnitude and direction, drives charges into the corresponding mirrored plate on the left side (left turquoise arrow), as dictated by symmetry. The current paths are closed to a loop by currents on the outer metal plane in the y- (yellow arrows) and x-directions (blue arrows), respectively. Overall, here the current phase lags behind the driving field phase by $\pi/2$.

To compact this resonator structure, we will remove areas of low current density, which are not necessary for the resonator functionality and merge adjacent current paths of opposite phase, allowing us to eliminate the affected elements completely. We start with reducing the unit cell size in x-direction. When reducing the spacing, the y-oriented currents along the left and right edges of the outer metal plane (yellow arrows) will start to overlap. However, since they feature opposite phases, they cancel out. Yet this change does not affect the current flow into and out of the

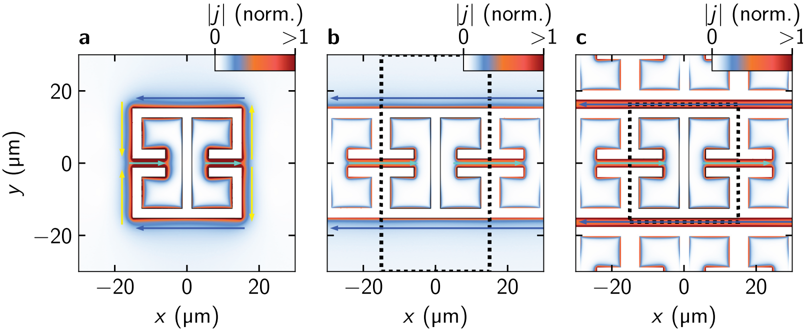

Figure 5.2 | Ultracompact resonator design and current distributions. **a**, Resonator layout featuring a conventional, large unit cell. Arrows: current flow of the fundamental optical mode. **b**, Resonator design compacted in x-direction, and current flow. The unit cell is indicated by the dashed rectangle. **c**, Butterfly resonator design, compacted in x- and y-direction, and current flow. Adapted from [Mor23a].

internal resonator area (turquoise arrows), as the currents continue on their path into the neighbouring resonator (Fig. 5.2**b**). Consequently, the optical mode remains unaffected, even when the spacing between resonators in x-direction is eliminated completely. In this configuration, the y-polarized current paths are now absent and no longer necessary, as the x-polarized currents flowing along the outer perimeter of the structure are also connected between adjacent resonators (blue arrows).

Next, we examine the reduction of the spacing between resonators in the y-direction. Here, the outer currents of adjacent unit cells in the y-direction share the same phase (blue arrows). Thus, the cancellation mechanism described for the x-direction cannot be used. However, as the currents favour the shortest paths, they concentrate near the edges of the metallized layer and as we move away from the edge, the current density quickly diminishes, falling off within a short distance of approximately 3 µm perpendicular to the edge. Thus, as long as the remaining metal strip is sufficiently wide to support the currents in x-direction, we can still compact the structure. We choose a spacing of 2.5 µm, resulting in an overall almost four-fold reduction in the unit cell's area (Fig. 5.1**b**, 5.2**c**).

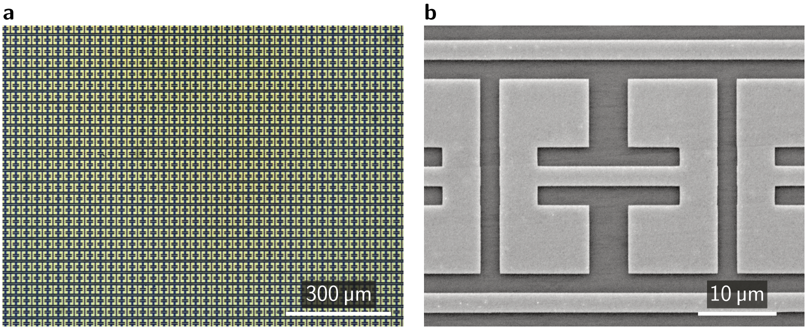

Figure 5.3 | Fabricated butterfly metasurface. a, Light microscope picture of a part of a metasurface array. **a**, Scanning electron microscope picture of a resonator.

The resulting metasurface is maximally compact and can no longer be separated into individual resonators. Yet, the near-field distribution of this compacted structure closely resembles that of the original design (Fig. 5.1**b**). Due to the shape loosely resembling a butterfly, we will call this resonator design from now on "butterfly". Examples of the fabricated resonator metasurfaces are displayed in Figure 5.3.
As the arguments of symmetry and current localization can be applied equally to all resonator modes, also the spectrum of the compacted structure does not differ significantly from that of the separated structures across the entire spectral range. Here the most prominent remaining differences result from the overall increase in transmission resulting from the reduction in unit cell size and coupling to surface plasmons at the gold/GaAs interface, which will be discussed in the next subsection.

Resonator spacing and coupling to surface plasmons

Metasurface resonator arrays are usually designed by starting with a single resonator and then scaling to an array. Thus, in the array, individual resonators are spaced far apart to minimise coupling between resonators, potentially changing the careful design of the individual resonators. Yet coupling effects are always present to a certain degree. Additionally, a low resonator density imposes the challenge of reduced overall transmission for measuring a negative resonator structure and increases computational complexity in the finite-element frequency-domain simulations due to the increased unit cell size.

Coupling between individual resonators in a negative resonator array is mediated by surface plasmons at the gold/substrate interface [Kel17a]. Their frequency ν_{SP} is given by

$$\nu_{\mathrm{SP}} = \frac{c}{2\pi}\sqrt{i^2\left(\frac{2\pi}{L_x n}\right)^2 + j^2\left(\frac{2\pi}{L_y n}\right)^2}, \tag{5.1}$$

where c is the speed of light in vacuum, n an effective refractive index, L_x and L_y the unit cell size of the metasurface in x- and y-direction, respectively and $i, j \in \mathbb{N}$. Here, $n = \frac{n_{\mathrm{GaAs}} n_{\mathrm{gold}}}{n_{\mathrm{GaAs}} + n_{\mathrm{gold}}}$ [Gha98, Kel17a] and can be approximated by the THz refractive index for GaAs, as $n_{\mathrm{GaAs}} \ll n_{\mathrm{gold}}$. A careful look at the surface plasmon frequency dependence reveals an alternative route to limit their influence on our resonances, as for small unit cells, all their frequencies increase, shifting out of our relevant frequency region.

The finite-element frequency-domain simulation for the employed resonator design, varying the quadratic unit cell size $L_x = L_y$ displays the main resonator modes, crossed by multiple surface plasmon modes with increasing unit cell size (Fig. 5.4**a**). For the maximally compacted butterfly structure and thus smallest possible unit cell, the lowest surface plasmon mode is shifted to a frequency above the second dipolar resonator mode. As a result, the two lowest resonator modes are no longer being affected by surface plasmon resonances. Increasing the unit cell, not only decreases the overall transmission, but also introduces coupling to multiple surface plasmons. Whereas the isolated transmission spectrum for the butterfly resonator (Fig. 5.4**b** black curve) displays only the main resonator resonances, the spectrum for a unit cell of 60 µm features multiple additional resonances, already for the bare resonator (Fig. 5.4**b** red curve). These additional resonances will make identifying polariton resonances in the structures with QWs much more difficult.

Plasmon excitation of resonator arrays

So far, we mostly treated the matter system as a single collective cyclotron resonance, neglecting any effects that arise from the electron plasma in the QWs itself (except in chapter 4.3). However, with increasing doping densities and QW number, these

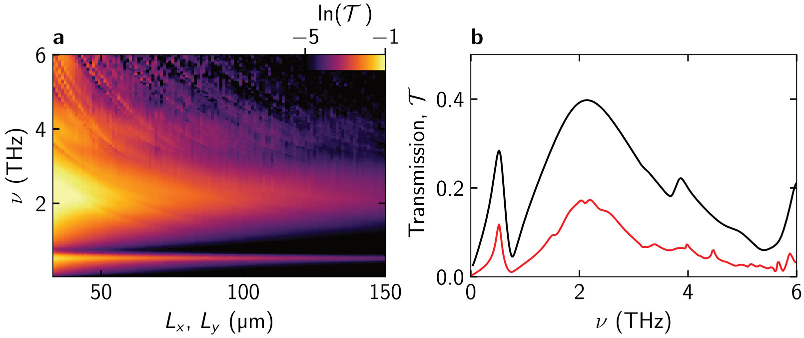

Figure 5.4 | Surface plasmon coupling of the resonator array a, Calculated THz transmission of the inverted resonator array as a function of the lattice spacing L_x, L_y. **b**, Calculated THz transmission for a unit cell of 60 µm (red) and the maximally compacted butterfly structure (black).

effects can no longer be neglected. Note that these are distinct from the surface plasmon effects we covered in the previous section. As discussed in chapter 4, the near-field enhancement of the metasurface resonators is not uniform in the QW plane and can differ between different resonator modes. Consequently, this implies that our coupling is not confined solely to an in-plane wave vector of $\boldsymbol{q}_{\|} = 0$, but rather extends to multiple wave vectors. Additionally, the periodicity of the metasurface, and thus of the field localization, quantizes the wave vectors of the light field that can couple to the electrons in the QWs. Therefore, to fully include effects from the plasma itself, we have to take its dispersion into account.

5.2. Plasmons of 2D electron gases

In absence of the external magnetic field, plasma excitations of a 2D electron gas obey the dispersion relation [Ste67, Pop05]

$$\omega_{\text{plasma}}\left(\boldsymbol{q}_{\|}\right) = \sqrt{\frac{\rho e^2}{2m^*\epsilon_0\epsilon_{\text{eff}}\left(\boldsymbol{q}_{\|}\right)}|\boldsymbol{q}_{\|}|}. \tag{5.2}$$

Here $\boldsymbol{q}_{\|}$ denotes the in-plane wave vector, ρ is the 2D electron density, m^* is the effective electron mass and $\epsilon_{\text{eff}}(\boldsymbol{q}_{\|})$ is the effective dielectric constant for the electron gas. When adding the static magnetic bias field oriented perpendicular to the QW plane, we again introduce Landau quantization and the plasmon excitations hybridize with the cyclotron resonance, ω_{c}, resulting in the formation of magnetoplasmons (MPs) [Kus01] with a frequency of

$$\omega_{\text{MP}} = \sqrt{\omega_{\text{c}}^2 + \omega_{\text{plasma}}^2}. \tag{5.3}$$

In order to calculate our plasma dispersion, we have to determine the effective dielectric constant $\epsilon_{\text{eff}}(\boldsymbol{q}_{\|})$, which is given by the dielectric environment of the 2DEG. Therefore, we have to consider all dielectric constants for the surrounding layers of the QWs. The dielectric constant of the GaAs substrate below the QWs is given by $\epsilon_{\text{sub}} = 12.9$. The capping layer on top of the QWs features a thickness of d and a dielectric constant of $\epsilon_{\text{barrier}}$. The dielectric function of the top interface depends on whether it is in contact with vacuum or the gold layer of the resonator structure. Previous studies [Egu75, Pop05] have provided effective dielectric functions for these cases, denoted as $\epsilon_{\text{ungated}}(\boldsymbol{q}_{\|})$ for the vacuum interface and $\epsilon_{\text{gated}}(\boldsymbol{q}_{\|})$ for a top-metallized 2DEG. For the latter two cases $\epsilon_{\text{eff}}(\boldsymbol{q}_{\|})$ is given by either

$$\epsilon_{\text{ungated}}\left(\boldsymbol{q}_{\|}\right) = \frac{\epsilon_{\text{sub}}}{2} + \frac{\epsilon_{\text{barrier}}}{2} \times \frac{1 + \epsilon_{\text{barrier}} \tanh(|\boldsymbol{q}_{\|}|d)}{\epsilon_{\text{barrier}} + \tanh(|\boldsymbol{q}_{\|}|d)}, \text{or} \tag{5.4}$$

$$\epsilon_{\text{gated}}\left(\boldsymbol{q}_{\|}\right) = \frac{\epsilon_{\text{sub}} + \epsilon_{\text{barrier}} \coth(|\boldsymbol{q}_{\|}|d)}{2}. \tag{5.5}$$

In more complex situations involving laterally structured samples like planar metal resonators or gratings, we construct an averaged effective dielectric function, taking into account both scenarios. This averaging is valid as long as the size of the structure is smaller than the plasmon wavelength. The constructed average dielectric function incorporates a factor δ that represents the relative metal coverage of the surface and is denoted by

$$\epsilon_{\text{eff,mix}}\left(\boldsymbol{q}_{\|}\right) = \delta\epsilon_{\text{gated}}\left(\boldsymbol{q}_{\|}\right) + (1-\delta)\,\epsilon_{\text{ungated}}\left(\boldsymbol{q}_{\|}\right). \tag{5.6}$$

Furthermore, in the case of a multi-quantum well (QW) stack composed of multiple layers with varying dielectric properties, an additional averaging of the effective dielectric function is necessary along the growth direction. Previous studies have shown that the response of densely packed QWs can be well approximated using an effective-medium approach [Bay17]. Additionally, it should be noted that the charge carriers within the QW stack do not exhibit the characteristics of an ideal two-dimensional electron gas due to the finite extension of the QWs in the growth direction. As the thickness of the QWs increases, their plasma frequency approaches the three-dimensional plasma frequency as an asymptotic upper limit for large wave vectors. In contrast, the dispersion of an ideal two-dimensional plasma has no such upper bound. We account for this effect by including a correction depending on the QW stack thickness d_{QW}. The effective dielectric function ϵ_{eff} for a thick stack of QWs can then be expressed as [Bon17]:

$$\epsilon_{\mathrm{eff}} = \epsilon_{\mathrm{eff,mix}} + \frac{\epsilon_{\mathrm{sub}}\ |\boldsymbol{q}_{\parallel}| d_{\mathrm{QW}}}{2}. \tag{5.7}$$

The description provided allows for a plasmon mode dispersion that approaches the three-dimensional (3D) plasma frequency as $|\boldsymbol{q}_{\parallel}|$ tends to infinity. However, it is important to consider the limitations imposed by Landau damping on the frequency and wave vector range of plasmon and magnetoplasmon excitations [Bac92, Kus01]. Landau damping becomes effective when single-particle excitations start to play a significant role. An upper bound for the frequency of these single-particle excitations can be determined by the expression $\nu < v_{\mathrm{F}}|\boldsymbol{q}_{\parallel}|$, with the Fermi velocity $v_{\mathrm{F}} = \frac{\hbar\sqrt{2\pi\rho}}{m^*}$.

The resulting plasmon dispersion for samples featuring 1, 3, 6, 12, 24 and 48 QWs is displayed in Figure 5.5. For samples featuring comparably low doping densities, such as the 1 and 3 QW samples, the plasmon dispersion is almost linear and the plasma frequencies $\nu_{\mathrm{p}} = \omega_{\mathrm{plasma}}/(2\pi)$ do not reach 1 THz for wavevectors $|\boldsymbol{q}_{\parallel}| < 2\,(\mu\mathrm{m})^{-1}$. For QW stacks with more QWs, the plasma frequencies reach up to 5 THz. For the stack with 48 QWs, even the frequency of the first plasmon mode with $|\boldsymbol{q}_{\parallel}| \neq 0$, that couples to the resonator array (see next section), supersedes the bare resonator frequency by three times. As a result, this significantly alters the nature of the coupling and cannot be disregarded.

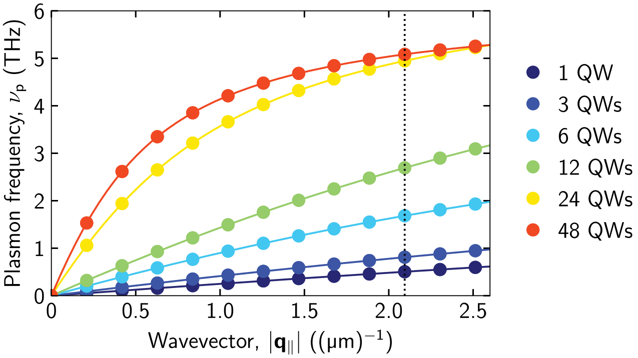

Figure 5.5 | Plasmon dispersion for all samples. The dots mark the plasmon frequencies which fulfil the diffraction condition. The black dashed line indicates the cut-off wavevector up to which plasmon modes were considered in the quantum model. Adapted from [Mor23a].

Resonator field enhancement in reciprocal space

The vacuum near fields of our resonator structures are not spatially homogenous over the complete QW plane. This fact and especially the effect of different spatial mode profiles of multiple resonator modes have already been discussed in real space in chapter 4. A non-homogenous mode profile in real space results in the resonator structure exciting in-plane vectors of $\boldsymbol{q}_\parallel \neq 0$. Up to now, we neglected effects of the plasma itself and assumed the cyclotron resonance being the only resonance in our matter system. As we can no longer neglect the plasma itself for samples featuring a high effective doping density, the wavevector decomposition of the resonator vacuum field plays a crucial role in determining coupling strength and polariton frequencies [Raj21]. Moreover, the periodic nature of our metasurfaces leads to a discretization of the plasmon wave vectors which can be excited by the cavity modes. As the dominant modes of the resonator structure mostly enhance the vacuum field in x-direction (see Fig. 5.1), we consider from now on only the x-component of $\boldsymbol{q}_\parallel$. The condition for the in-plane wave vector q_x is given by

$$q_x\left(\alpha\right) = \frac{2\pi}{L_x}\alpha. \tag{5.8}$$

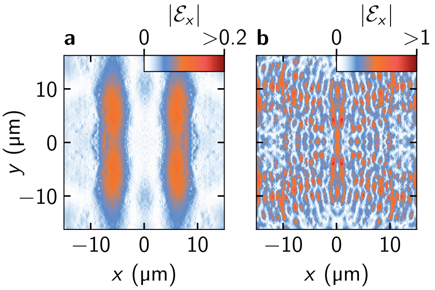

Figure 5.6 | Plasma wave excitation of the butterfly resonator in the 48 QW sample. Finite-element frequency-domain simulation of the electric field distribution $|\mathcal{E}_x|$ in the QW stack, 300 nm below the resonator **a**, for a frequency of 0.275 THz and **b**, for 0.925 THz. Note that coupling effects are included in the calculation, as they cannot be excluded.

Here, $\alpha \in \mathbb{Z}$ is the plasmon mode index. The small value of $L_x = 30\,\mu\text{m}$ increases the energy spacing of the now distinct magnetoplasmon modes we can couple to, when compared to previously investigated structures with larger unit cells. Bright and dark standing waves, given as $\Psi_\text{b} \propto \exp(-iq_x x) + \exp(iq_x x)$ and $\Psi_\text{d} \propto \exp(-iq_x x) - \exp(iq_x x)$, respectively, can be formed by linear combinations of plasmon waves with wave vectors $-q_x$ and q_x. In the context of coupling to cavities, only the bright modes couple to the cavity modes, since their dipole moments add constructively, and we therefore focus our attention on these. We disregard the dark standing waves, as their dipole moments cancel out. We can use the finite-element frequency-domain simulations to observe the plasmon waves excited in the QWs by the butterfly resonator structure for our sample featuring 48 QWs (Fig. 5.6). In the simulations the effect of light-matter coupling cannot be switched off, so the modes reflect their coupled state. For a frequency of $\nu = 0.275\,\text{THz}$ we observe two electric field maxima on the left and right side of the central gap (Fig. 5.6**a**), corresponding to the coupled low frequency upper plasmon polariton mode $\text{UP}_{1,0}$ (see Fig. 5.12**b**). At a higher frequency of $\nu = 0.925\,\text{THz}$, the field distribution in the whole unit cell is filled with oscillations with a higher spatial frequency of $\approx 0.9\,\mu\text{m}$ (Fig. 5.6**b**). This mode corresponds to the $\text{UP}_{2,0}$ plasmon polariton mode (see Fig. 5.12**b**).

To analyse the effect of coupling to (magneto-)plasmons with $q_x \neq 0$ systematically, we calculate the 2D Fourier transform of the x-polarized electric near-field component, $\mathcal{E}_x$, for the first two cavity modes (Fig. 5.7), using finite-element frequency-domain simulations (appendix C). This calculation is performed using undoped QWs to obtain the modes of the bare cavity (Fig. 5.7 insets) and evaluated within xy-oriented

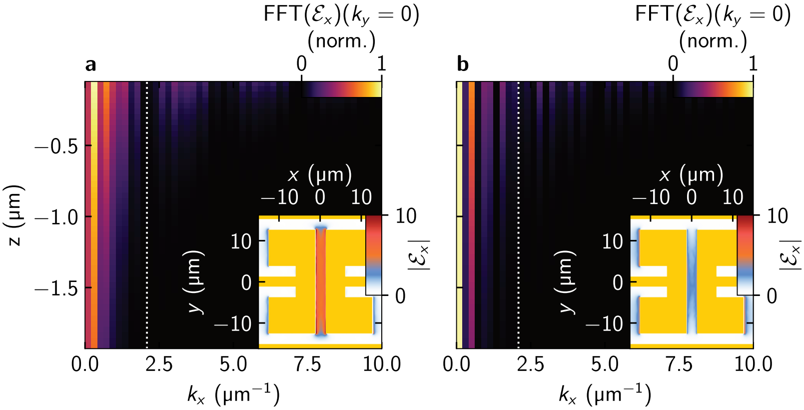

Figure 5.7 | Analysis of magneto-plasmon formation. a, Amplitude components of the Fourier transform of the electric field component $\mathcal{E}_x$ for the LC mode ($j = 1$) at 0.52 THz as a function of the wave vector k_x, for $k_y = 0$, and the depth of the plane below the metasurface, z. Inset: $|\mathcal{E}_x|$ in the quantum well plane 50 nm below the resonator structure. **b**, Equivalent amplitude components for the data of the dipolar mode ($j = 2$) at 1.95 THz. Adapted from [Mor23a].

planes lying within the QW stack. Again, the $\mathcal{E}_y$ components are significantly weaker than the dominant $\mathcal{E}_x$ field enhancement and thus are neglected. As a result, we obtain the amplitudes FFT($\mathcal{E}_x$)($q_x = 0$), integrated within the respective planes, as a function of the wave vector, q_x, and the depth below the metasurface, z. Both, the spectrum for the LC and the DP resonator mode, show significant excitation of plasmon modes, whereas for the LC mode, the dominant excitation occurs for $q_x(\alpha = 1)$ (Fig. 5.7**a**). For the dipolar cavity mode, the strongest excitation is present for $q_x(\alpha = 0) = 0$ and almost no excitation at $q_x(\alpha = 1)$. Considering the effect of single-particle excitations discussed in the previous paragraph and the decay of the field amplitude for larger wave vectors, especially in planes located further away from the metasurface, we limit the magnetoplasmon mode index α to a maximum of $|\alpha| \leq \alpha_c = 10$. This choice allows us to model the coupling of the light field to each individual magnetoplasmon and account for their relative amplitudes, displayed with the discretization condition, and the cut-off wave vector in Figure 5.5.

5.3. Multi-mode coupling of multiple light and matter modes

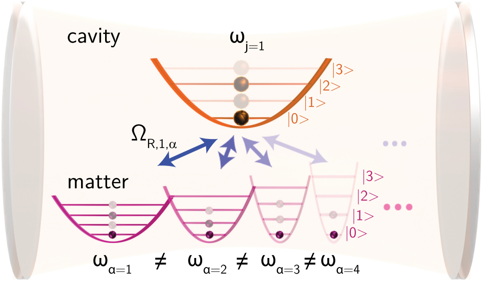

Figure 5.8 | Off-resonant multi-mode coupling. Illustration of deep-strong coupling of multiple light modes (upper parabolas) to multiple matter excitations (bottom parabolas) with vacuum Rabi frequencies $\Omega_{\mathrm{R},j,\alpha}$ under off-resonant conditions. Owing to the extremely large light-matter coupling, a significant number of virtual excitations are present (semi-transparent spheres). Adapted from [Mor23a].

As demonstrated in multiple publications [Ana09, Gü09, Tod10, Sca12, Mai14, Bay17, Mue20] and within the previous chapters of this thesis, even for USC or DSC, a single-mode model often suffices for a description of the situation. However, with rising doping densities of the QWs, this description begins to lose accuracy, necessitating the inclusion of the magnetoplasmon resonances when the plasma frequency $\omega_{\mathrm{plasma}}(q_x(\alpha_{\mathrm{c}}))$ exceeds the linewidth of the cyclotron resonance. Under such conditions, we now account for the coupling of each magnetoplasmon characterized by a frequency $\omega_{\mathrm{MP},\alpha}$ to multiple resonator modes, denoted as j (Fig. 5.8).

In order to describe the coupling arising from this extreme setting of strong, off-resonant coupling of multiple light and matter modes with highly disparate frequencies, we develop our light-matter coupling Hamiltonian (see chapter 2.1 and 3) further:

$$\hat{H} = \sum_j \hbar\omega_j \hat{a}_j^\dagger \hat{a}_j + \sum_\alpha \hbar\omega_{\mathrm{MP},\alpha} \hat{b}_\alpha^\dagger \hat{b}_\alpha + \sum_{\alpha,j} \hbar\Omega_{\mathrm{R},j,\alpha} \left(\hat{a}_j^\dagger + \hat{a}_j\right)\left(\hat{b}_\alpha^\dagger + \hat{b}_\alpha\right) + \sum_{\alpha,j} \frac{\hbar\Omega_{\mathrm{R},j,\alpha}^2}{\omega_{\mathrm{MP},\alpha}} \left(\hat{a}_j^\dagger + \hat{a}_j\right)^2 + \hat{H}_{\mathrm{ext}}. \tag{5.9}$$

Here, in addition to including multiple cavity modes j, we introduce multiple magnetoplasmon modes α, with individual vacuum Rabi frequencies $\Omega_{\mathrm{R},j,\alpha}$, which are determined based on the amplitudes of the corresponding wave vectors, as described in the previous section. These include the decay of the near-field amplitude in z-direction, accounting for the coupling to the complete QW stack. To match the experimental spectra, the entire set of $\Omega_{\mathrm{R},j,\alpha}$ is scaled by a single amplitude scaling factor that applies to all modes. For the employed butterfly resonator and planar QWs, modal overlap of the cavity modes, described in chapter 4, is minimal and thus not included in the Hamiltonian. Further, we limit ourselves to the coupling of the first two cavity modes, as these dominate the resonance spectrum up to 6 THz, whilst coupling to higher modes is observed to be minimal.

As a result of the coupling between $2|\alpha_{\mathrm{c}}| + 1 = 21$ magnetoplasmon resonances and each resonator mode, 22 light-matter hybridized modes form. Each polariton mode is a superposition of all magnetoplasmon modes and only one cavity mode, due to the nearly orthogonal nature of the cavity modes (see chapter 4). These modes are labelled with the existing cavity mode index, j, and a new index, β, to represent the 22 resulting magnetoplasmon cavity polaritons (MPPs). The magnetoplasmon polaritons are split into a lower polariton (LP) mode, denoted as $\mathrm{LP}_{j,\beta=0}$, and several upper polariton (UP) modes, denoted as $\mathrm{UP}_{j,1\leq\beta\leq\alpha_{\mathrm{c}}+1}$. This polariton spectrum of a single LP mode, but multiple UP modes is a unique feature of multi-mode coupling, where all independent magnetoplasmon modes cooperatively couple to a common cavity mode. The single LP and the set of UPs can be distinguished by their Hopfield coefficients, since the signs of their resonant cavity and anti-resonant matter fractions differ (see Fig. 5.15 for details). As a consequence, they vary in their magnetic field dependence, as shown in chapter 2 for the case of single-mode coupling and later in this chapter for multi-mode coupling. While dark modes with $\beta < 0$ are included, they do not couple to the cavity modes and will be discussed later in more detail.

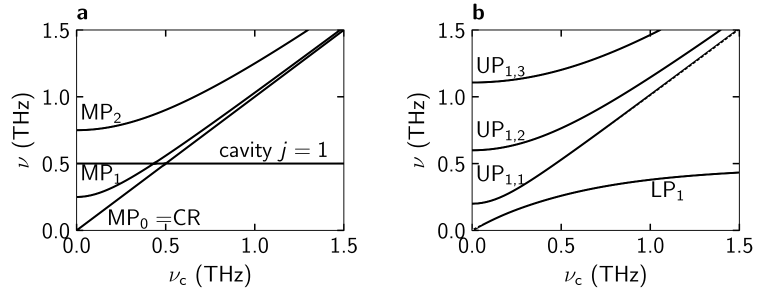

Figure 5.9 | Characteristics of multi-mode coupling. Illustration of multi-mode coupling of one cavity mode to several matter modes, $\mathrm{MP}_0 = \mathrm{CR}$, MP_1 and MP_2, as a function of the cyclotron frequency, ν_c. **a**, uncoupled modes. **b**, coupled modes comprising of one lower polariton (LP_1) and three upper polaritons ($\mathrm{UP}_{1,1}$, $\mathrm{UP}_{1,2}$ and $\mathrm{UP}_{1,3}$). Adapted from [Mor23a].

As an instructive example, we will look at the coupling of a single cavity mode $j = 1$ to three magnetoplasmons, whereas the first magnetoplasmon, MP_0, is the bare cyclotron resonance. Their bare frequencies as a function of the cyclotron resonance ν_c, without coupling, is displayed in Figure 5.9**a**. Switching the coupling on (Fig. 5.9**b**), four magnetoplasmon polariton resonances form with monotonically increasing frequencies. The LP_1 mode emerges asymptotically from below the cyclotron resonance (CR) near $\nu_\mathrm{c} = 0$ and gradually approaches the cavity frequency as ν_c becomes larger. On the other hand, the $\mathrm{UP}_{j=1,\beta}$ modes, at $\nu_\mathrm{c} = 0$, exhibit a finite frequency determined by the plasma frequencies of the constituent magnetoplasmon modes and the diamagnetic shift induced by the photon field. As ν_c increases, all UP modes bend upward and eventually converge asymptotically towards the cyclotron resonance. Remarkably, contrary to the case of single mode coupling, an upper polariton mode can exist for frequencies lower than its associated cavity frequency, specifically, $\nu_{\mathrm{UP},j,\beta} < \nu_j$. This not only eliminates the previously observed bandgap that exists in the context of single mode coupling, which is created by the diamagnetic term and separates the two polariton modes, but also serves as a unique indicator of multiple matter modes interacting with a single cavity mode.

Experimental results

For an initial experimental investigation of the effects of multi-mode coupling, we employ samples with 1, 3, 6, and 12 QWs, measured with the THz time-domain setup detailed in chapter 2.3 and used to obtain the experimental data shown in prior chapters.

In the case of a single QW (Fig. 5.10**a**), a single LP_1 mode is located below the cyclotron resonance. As ν_c increases, the LP_1 mode approaches the frequency of the bare first cavity mode at 0.52 THz. At $\nu_\mathrm{c} = 0\,\mathrm{THz}$, we observe a dense fan of partially overlapping $\mathrm{UP}_{1,\beta}$ modes, starting at a frequency of 0 THz. Among these UP modes, the most prominent one, highlighted by the uppermost semi-transparent white curve, exhibits the highest frequency at $\nu = 0.78\,\mathrm{THz}$. As ν_c increases, the entire UP mode structure bends upward in frequency, as discussed for the example, and occupies a progressively narrower spectral bandwidth between the cyclotron resonance and the highest-energy UP mode. Similarly, coupling to the second cavity mode with a frequency of $\nu_2 = 1.95\,\mathrm{THz}$ results in a LP_2 mode, represented by the lowermost dotted curve in the plot. As ν_c is increased, the LP_2 mode branches off below the cyclotron resonance and reaches a frequency of $\nu = 1.65\,\mathrm{THz}$ at $\nu_\mathrm{c} = 1.9\,\mathrm{THz}$. The ensemble of $\mathrm{UP}_{2,\beta}$ modes depicted by the upper dotted curves is dominated by a single spectral feature centred around $\nu = 2.0\,\mathrm{THz}$ for $\nu_\mathrm{c} = 0\,\mathrm{THz}$. As ν_c increases, this feature slightly shifts towards higher frequencies.

In the case of three QWs (Fig. 5.10**b**), the electronic dipole moment is enhanced, resulting in an increase in the frequency spacing of the uncoupled magnetoplasmons, $\nu_\mathrm{MP}(\alpha)$ as well as the coupled magnetoplasmon polaritons. At $\nu_\mathrm{c} = 0\,\mathrm{THz}$, the $\mathrm{UP}_{1,\beta}$ modes span a frequency range from approximately 0 to 1.0 THz, exhibiting well-separated resonances that clearly demonstrate the multi-mode nature of the coupling. The increased interaction also causes a further upward shift in the frequencies of the $\mathrm{UP}_{2,\beta}$ modes, while simultaneously lowering the frequencies of the LP_j modes.

Moving on to the 6 QW case (Fig. 5.10**c**), we observe a pronounced magnetoplasmon polariton fan with well-separated $\mathrm{UP}_{1,\beta}$ modes that extend up to 1.65 THz at $\nu_\mathrm{c} = 0\,\mathrm{THz}$. The $\mathrm{UP}_{2,\beta}$ modes reach frequencies up to 2.0 THz.

Increasing the number of QWs to 12 QWs (Fig. 5.10**d**), distinct branches of $\mathrm{UP}_{1,\beta}$ and $\mathrm{UP}_{2,\beta}$ modes at frequencies reaching up to 2.5 THz and 3.2 THz, respectively,

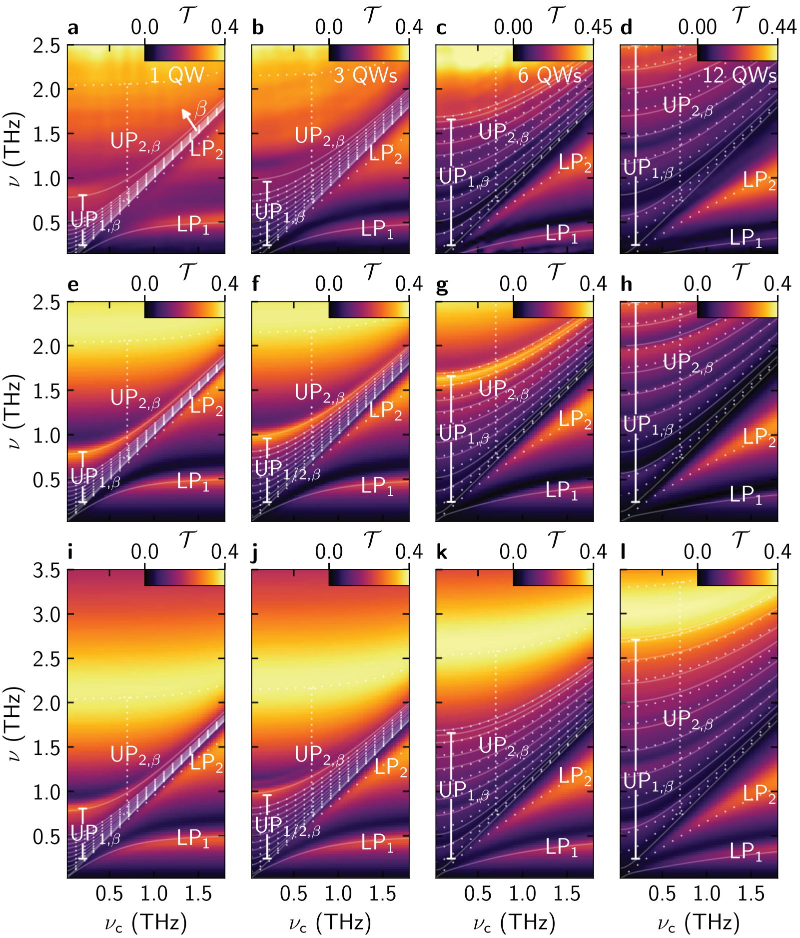

Figure 5.10 | Deep-strong multi-mode coupling. **a**, THz transmission spectra as a function of ν_c of the 1-QW structure. Continuous curves: polariton modes from the multi-mode Hopfield model for the first resonator mode (coupling strength: $\eta_1 = 0.55$). Dashed curves: polaritons linked to the higher mode ν_2 ($\eta_2 = 0.13$). **b**, Transmission of the 3-QW structure ($\eta_1 = 0.76$). **c**, Transmission of the 6-QW structure ($\eta_1 = 1.34$). **d**, Transmission of the 12-QW structure ($\eta_1 = 2.32$). **e-h**, Spectra from the time-domain quantum model. **i-l**, Spectra from the finite-element frequency-domain simulations. Adapted from [Mor23a].

are observed. Remarkably, several of these modes exhibit ultrastrong coupling simultaneously, with centre frequencies reaching up to approximately 5 times the frequency of the bare cavity mode, $\nu_{j=1} = 0.52\,\mathrm{THz}$.

Fitting and extraction of the coupling strength

To accurately assign and fit the individual, multiple resonances and investigate the nature of the coupling in detail, we use our finite-element frequency-domain simulations as well as time-domain simulations derived from the Hamiltonian. As in chapter 3, we use Heisenberg's equations of motion to derive the time evolution of each operator, calculate the temporal evolution upon excitation and, through a Fourier transform, the spectral characteristics of the coupled modes. The frequency response of the bare metasurface is effectively modelled by a superposition of cavity modes, where each cavity mode α_j with a cavity frequency ν_j contributes with a relative amplitude, phase, and damping rate carefully selected to ensure an optimal representation of the far-field response (see Fig. 5.4 and appendix D). The theoretical calculations based on these equations accurately reproduce the measured spectra (Fig. 5.10**e-h**). The matching line widths and oscillator strengths of all modes across the entire experimentally accessible spectral range confirm the theory's ability to capture the complex dynamics of the coupled modes in our system. The finite-element frequency-domain simulations (Fig. 5.10**i-l**), quantitatively match the experimental data over the complete experimentally accessible spectral range as well, without any free fitting parameter besides the doping density ρ. The excellent agreement of theory and experiment allows us to determine the set of individual coupling constants, $\Omega_{\mathrm{R},j,\alpha}$ with great precision.

In this context of multiple matter modes being off-resonantly coupled to multiple light modes with extreme coupling strengths, the concept of the anti-crossing point, which maximizes the coupling strength between a single pair of modes, loses its relevance. Especially in our multi-mode coupling scenario, an appropriate figure of merit for characterizing the system is actually the number of virtual photons $\langle N_j \rangle = \langle G | \hat{a}_j^\dagger \hat{a}_j | G \rangle$ associated with each photonic mode j, and the number of virtual matter excitations $\langle G | \hat{b}_\alpha^\dagger \hat{b}_\alpha | G \rangle$ of each magnetoplasmon mode, as both of these virtual excitations govern most of the fascinating effects of USC and DSC. When the

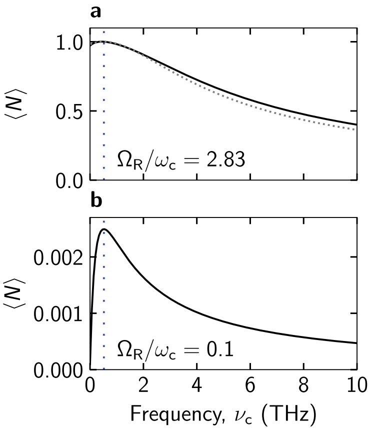

Figure 5.11 | Virtual photon population $\langle N \rangle$ as a function of detuning with the cyclotron frequency ν_c. **a**, For the structure featuring 48 QWs (black) with an equivalent single-mode coupling strength of $\Omega_R/\omega_c = 2.83$ and including all magnetoplasmons. Grey dashed line: coupling of only a single cavity and matter mode with equivalent coupling strength. Dotted blue line: $\nu_c = \nu_{cav} = 0.52\,\text{THz}$. **b**, For the single modes with a coupling strength of $\Omega_R/\omega_c = 0.1$. Adapted from [Mor23a].

coupling strength for an individual mode reaches the DSC regime, even off-resonant coupling decreases the virtual photon population only slightly, further diminishing the significance of an individual anti-crossing point. This enables the total vacuum photon population to be increased almost arbitrarily by adding electronic oscillator strength within a spectral window that can span several octaves in frequency. Let's consider a specific case to illustrate this behaviour. Suppose we have a single cavity mode with a resonance frequency of $\nu_{cav} = 0.52\,\text{THz}$ coupled to a single matter mode, with a coupling strength of $\Omega_R/\omega_c = 2.83$ (approximating the situation of the structure with 48 QWs, discussed shortly) (Fig. 5.11**a** dotted grey curve). As expected, the vacuum photon population as a function of the cyclotron frequency ν_c features a maximum at the anti-crossing point $\nu_c = \nu_{cav} = 0.52\,\text{THz}$. However, surprisingly, even with a significant detuning of ν_c from the anti-crossing point, the vacuum photon population remains above 50% of its maximum value when the modes are resonant. This behaviour is also found for the multi-mode configuration, as observed for the 48-QW structure with the same equivalent coupling strength $\Omega_R/\omega_c = 2.83$ (Fig. 5.11**a** black curve). However, the situation changes significantly for moderate coupling strengths. For a single pair of light and matter modes with $\Omega_R/\omega_c = 0.1$, a much stronger dependence of $\langle N \rangle$ on the detuning is observed (Fig. 5.11**b**). Here, reducing the cyclotron frequency to $\nu_c = 0.1\,\text{THz}$ or increasing it to $3\,\text{THz}$ already reduces the number of virtual photons to 50%. This comparison demonstrates that effective multi-mode coupling over multiple optical octaves critically relies on significant light-matter coupling strengths, as in the multi-mode configuration, at most, one magnetoplasmon mode is in resonance with the cavity mode.

For the 1-QW structure, the theory fit yields virtual photon populations of $\langle N_1 \rangle = 0.07$ and $\langle N_2 \rangle = 4 \times 10^{-3}$ for the first and second cavity mode, respectively. In comparison, if we consider the hypothetical coupling strength η of a single pair of resonant light and matter modes that would result in the same total vacuum photon number, we obtain $\eta_1 = 0.55$ and $\eta_2 = 0.13$. Increasing the number of QWs to 3, we achieve $\langle N_1 \rangle = 0.13$ and $\langle N_2 \rangle = 0.01$, resulting in $\eta_1 = 0.76$ and $\eta_2 = 0.19$. The model also successfully reproduces the transition from the merged ensemble of $\mathrm{UP}_{1,\beta}$ modes to clearly distinguishable individual magnetoplasmon polariton resonances (Fig. 5.10**e-h** and transparent lines). Similarly, for the 6-QW structure, the calculation replicates the data, and we obtain $\langle N_1 \rangle = 0.34$ and $\langle N_2 \rangle = 0.03$, resulting in $\eta_1 = 1.34$ and $\eta_2 = 0.36$. Doubling the number of QWs again to 12, the calculation results in $\langle N_1 \rangle = 0.76$, $\langle N_2 \rangle = 0.08$ and $\eta_1 = 2.32$, $\eta_2 = 0.60$, significantly surpassing previous vacuum photon population and effective coupling strength records [Bay17, Mue20].

Maximal achievable deep-strong coupling

While our structure with 12 QWs already exceeds all previous records, we push the limits of our approach further and fabricate two additional structures with up to 48 QWs. The increased number of QWs allows us to occupy almost the entire available cavity mode volume and further enhance the electronic oscillator strength. As a result, we observe deep-strongly coupled polariton modes that extend over six optical octaves and exhibit a highly structured spectrum (Fig. 5.12). While damping effects make it more difficult to identify single modes in the experimental data (Fig. 5.12**a,c**), our theoretical model (Fig. 5.12**b,d** and appendix D) makes it possible to confirm our measurements. Despite the large coupling strength, we are still able to observe the LP_1 mode at frequencies of 0.15 THz to 0.34 THz. For the sample with 24 QWs, we observe an even more structured fan of UP modes, with a single strong mode at 1.3 THz and multiple modes reaching up to 4.3 THz for $\nu_c = 0\,\mathrm{THz}$ (Fig. 5.12**a**). For the sample with 48 QWs, this trend continues, as the lower polaritons shift even

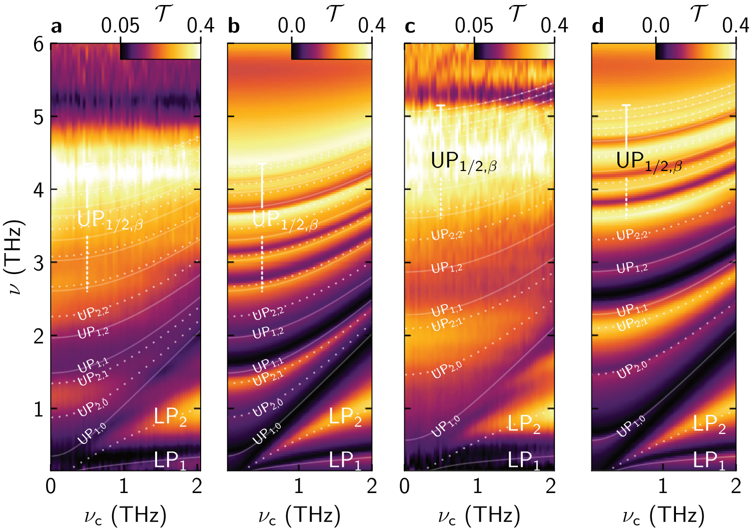

Figure 5.12 | Extremely strong, multi-octave light-matter coupling. **a**, THz magneto-transmission of the 24-QW sample as a function of ν_c. The extended Hopfield model yields coupling strengths of $\eta_1 = 2.80$ and $\eta_2 = 0.85$ for the first and second resonator mode, respectively. Calculated polariton frequencies (solid and dashed curves) with distinct resonances marked. **b**, Calculated transmission and polariton frequencies. **c**, Transmission of the 48-QW structure. Coupling strengths: $\eta_1 = 2.83$, $\eta_2 = 0.88$. **d**, Calculated transmission and identical polariton frequencies. Adapted from [Mor23a].

lower in frequency and the complete UP fan increases in frequency, now reaching frequencies above 5 THz. Our theoretical model confirms even higher than before vacuum photon populations and coupling strengths. With 24 QWs, we achieve $\langle N_1 \rangle = 0.99$, $\langle N_2 \rangle = 0.16$ and $\eta_1 = 2.80$, $\eta_2 = 0.85$. For the 48 QW structure, we reach $\langle N_1 \rangle = 1.00$, $\langle N_2 \rangle = 0.17$ and $\eta_1 = 2.83$, $\eta_2 = 0.88$. Notably, for the first time, the vacuum photon population of a single coupled optical mode reaches unity, while the combined ground state population of both modes, $\langle N \rangle = \langle N_1 \rangle + \langle N_2 \rangle = 1.17$, surpasses it. The effective, combined coupling strength of $\Omega_R^s/\omega_s = 3.19$ exceeds the values of existing structures ($\eta = 1.43$ [Bay17] and $\eta = 1.83$ [Mue20]) by almost a

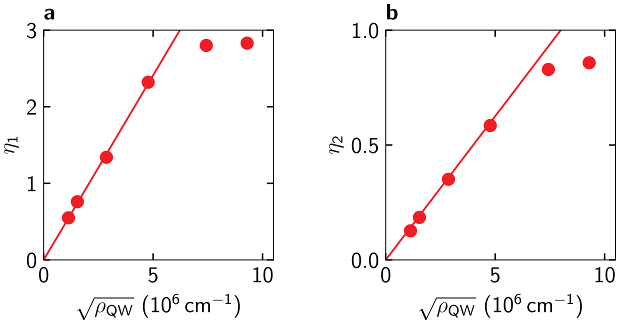

Figure 5.13 | Scaling of the coupling strength with the number of electronic oscillators. a, Equivalent coupling strength η_1 for the first cavity mode as a function of the square root of the total charge carrier density, and linear fit of the data adjusted to the first four data points. **b**, Equivalent data for the second cavity mode. Adapted from [Mor23a].

factor of 2. Here the vacuum ground state exhibits strong squeezing of the photonic mode and a highly non-classical Fock-state probability distribution (see chapter 2). Moreover, the extreme coupling also results in virtual excitations of the matter system, with a combined population of the magnetoplasmons by 1.06. These vacuum ground state properties open up exciting possibilities for wide-ranging control of transport, chemical reactions, and phase transitions by vacuum fluctuations.

According to our findings in chapter 4 and of ref. [Hag10], the coupling strength for collective excitations, such as Landau polaritons, is expected to scale with the square root of the total carrier density $\rho_{\mathrm{QW}} = \rho N_{\mathrm{QW}}$ in the quantum well stack. This scaling law holds true for the coupling of the LC and DP resonator modes for the structures with 1, 3, 6, and 12 QWs (Fig. 5.13). However, for the structures with 24 and 48 QWs, we begin to see a deviation from this ideal scaling law. This discrepancy can be attributed to the limited penetration depth of the near field into the QW stacks. As the number of QWs increases, the near field may not effectively interact with all the QWs, leading to a reduced impact on the overall coupling strength. Despite this deviation, the coupling strength still increases with the additional QWs, albeit not at the same rate.

Dynamics of the multi-mode coupled state

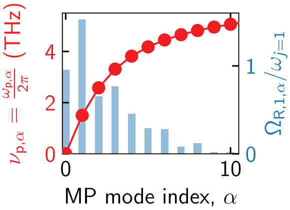

Figure 5.14 | Plasmon coupling strength. Plasmon frequency $\nu_{\mathrm{p},\alpha}$ and coupling strength $\Omega_{\mathrm{R},1,\alpha}/\omega_{j=1}$ for each magnetoplasmon mode α in the case of the 48 QW sample. Adapted from [Mor23a].

For a closer look at the nature of our deep-strongly coupled system, we restrict ourselves to the sample with 48 QWs and the most extreme coupling strengths. In this scenario, the plasmon frequencies $\nu_{\mathrm{p},\alpha}$ significantly surpass those of the cavity modes (red dots in Fig. 5.14), yielding highly non-resonant coupling. Notably, despite the off-resonant nature of this interaction, the individual coupling strengths $\Omega_{\mathrm{R},1,\alpha}/\omega_{j=1}$ reach the DSC regime (Fig. 5.14, blue bars). Since most plasmon modes are never resonant with the cavity mode to form an individual anti-crossing point, the individual coupling strength shown is calculated as if such an anti-crossing point existed by rescaling Ω_{R} according to $\Omega_{\mathrm{R}} \propto \sqrt{\omega_{\mathrm{c}}}$ (see equation 4.6).

Diagonalization of the Hamiltonian does not only yield the polariton frequencies but allows us to determine the composition of the coupled modes. The normal-mode polariton operators, denoted as $\left\{\hat{p}_{\beta,j}, \hat{p}^{\dagger}_{\beta,j}\right\}$, are expressed as

$$\hat{p}_{\beta,j} = w_{\beta,j}\hat{a}_j + \sum_{\alpha} x_{\beta,\alpha}\hat{b}_{\alpha} + y_{\beta,j}\hat{a}^{\dagger}_j + \sum_{\alpha} z_{\beta,\alpha}\hat{b}^{\dagger}_{\alpha} \tag{5.10}$$

and incorporate contributions from one cavity and all magnetoplasmon modes.

The Hopfield coefficients $(w_{\beta,j}, x_{\beta,\alpha}, y_{\beta,j}, z_{\beta,\alpha})$ represent the polariton fractions associated with the bare cavity and matter modes. The values of these Hopfield coefficients are illustrated in Figure 5.15 as a function of the magnetoplasmon index α and the polariton index β, considering a cyclotron frequency of $\nu_{\mathrm{c}} = 0.52\,\mathrm{THz}$ and the coupling to the first cavity mode $j = 1$.

Each wave vector pair $(-q_x, q_x)$ gives rise to two hybridized modes, a dark magnetoplasmon mode and a bright magnetoplasmon mode. The dark magnetoplasmons do not couple to the resonator mode, due to a vanishing net dipole moment. We

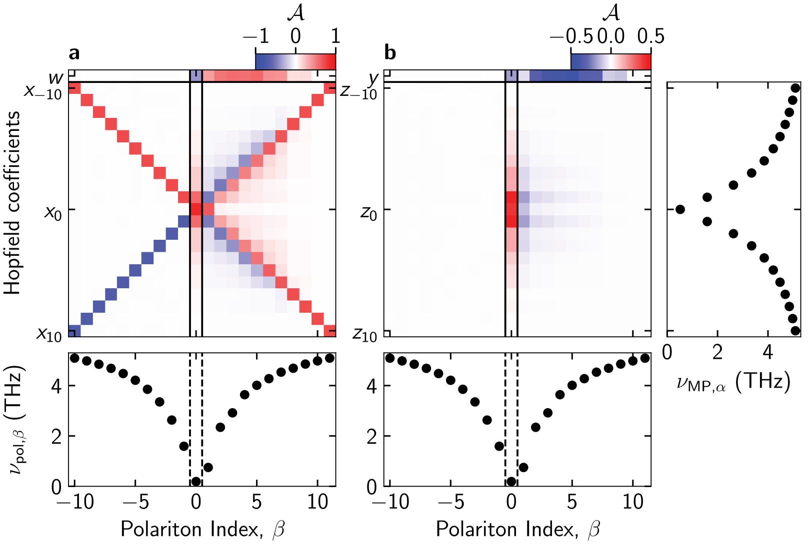

Figure 5.15 | Hopfield coefficients for the 48-QW structure. **a**, Plot of the (real-valued) Hopfield coefficients; for the lowest cavity mode, $j = 1$, and a cyclotron frequency of $\nu_c = 0.52\,\mathrm{THz}$. The right and bottom panels show the frequencies of the uncoupled magnetoplasmon and the coupled polariton modes, respectively. w: light mode, x_{-10} to x_{10}: plasmon modes. Polariton index $\beta < 0$: uncoupled magnetoplasmon modes, $\beta = 0$: lower polariton, $\beta > 0$: upper polaritons. **b**, Absolute values of the anti-resonant Hopfield coefficients. y: light mode, z_{-10} to z_{10}: plasmon modes. Adapted from [Mor23a].

assign the dark magnetoplasmon polaritons a polariton index $\beta < 0$. The nature of the dark modes is also evident in their Hopfield coefficients, as they remain solely a superposition of the two magnetoplasmons with opposite sign with $x_{-\alpha} = -x_\alpha$ and no cavity component w (Fig. 5.15**a**), nor any anti-resonant coefficients z_α or y (Fig. 5.15**b**).

In contrast, bright magnetoplasmons form the coupled magnetoplasmon polaritons with $\beta \geq 0$. These are not each a mix of the cavity mode and a single magnetoplasmon mode, but rather a superposition of the cavity mode and all magnetoplasmons at the same time. The Hopfield coefficients of the lower polariton ($\beta = 0$) feature opposite signs for the cavity components w and y compared to the matter components x_α and z_α (Fig. 5.15**a,b**). All modes of the UP fan feature an even more intricate composition of light and matter. While all anti-resonant coefficients y and z_α are negative (Fig. 5.15**b**), all resonant coefficients are positive, except for the magnetoplasmon coefficients where $\nu_{\mathrm{MP},\alpha} > \nu_{\mathrm{pol},\beta}$ (Fig. 5.15**a**). The fact, that each polariton is a mixture of multiple matter modes hallmarks the cooperative nature of the multi-mode coupling.

Multi-mode coupling time-domain dynamics

The extraordinary nature of the deep-strongly coupled multi-mode system becomes particularly apparent when examining the subcycle dynamics in the temporal domain. Therefore, we use the derived equations of motion for each operator (see this chapter and also chapter 3). The simulation allows us to analyse the microscopic polarization dynamics of each individual cavity and matter resonance. Furthermore, they allow for the quantitative fit shown in Figure 5.10 by Fourier transform.

When exciting the 48-QW sample at $\nu_\mathrm{c} = 0.52\,\mathrm{THz}$, the transmitted experimental waveform exhibits a prominent initial cycle at a time delay of $t = 0\,\mathrm{ps}$ (Fig. 5.16**a**). Starting from $t = 0.5\,\mathrm{ps}$, we observe trailing oscillations that display multiple beating patterns (indicated by arrows). These oscillations arise from the complex energy exchange occurring between multiple coupled modes. The corresponding spectrum reveals a global maximum near $2\,\mathrm{THz}$, accompanied by local maxima adjacent to it, corresponding to the magnetoplasmon polaritons modes (Fig. 5.16**a**, inset). For a deeper insight into the intricate energy exchange, we excite the system in the simulation with a short, broadband THz pulse (Fig. 5.16**b** grey waveform) and observe the response of the first cavity mode (black waveform). Here the electric field oscillates on much shorter timescales compared to the cycle duration of the uncoupled mode (grey-shaded background area) and again displays multiple beating patterns. The corresponding spectrum exhibits a total of eight local maxima with comparable amplitudes, ranging from $0.2\,\mathrm{THz}$ to as high as $4.5\,\mathrm{THz}$ (Fig. 5.16**b**, inset), corresponding to magnetoplasmon polariton modes. These features exceed the frequency of the uncoupled cavity by nearly an order of magnitude and hallmark

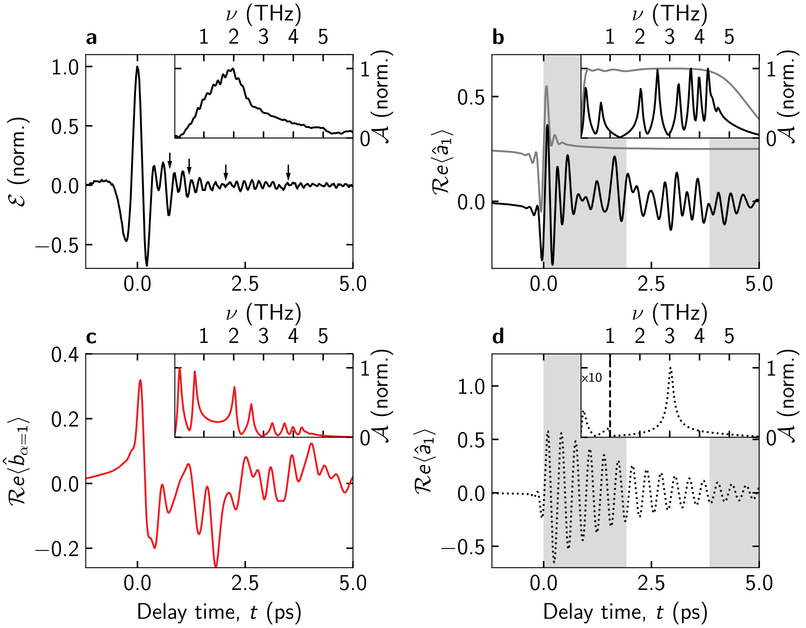

Figure 5.16 | Dynamics of extremely strong multimode coupling. a, Transmitted THz field of the 48-QW sample ($\eta_1 = 2.83$) at $\nu_c = 0.52\,\mathrm{THz}$ (black curve). Inset: spectral amplitude of the THz field. **b**, Calculated expectation value for the population of the first cavity mode $\mathcal{R}e\langle\hat{a}_1\rangle$ after excitation (black curve) by a broadband pulse (grey curve). Inset: corresponding spectra. The shading marks one oscillation period of the bare cavity mode. **c**, Calculated expectation value of the polarization of the first magnetoplasmon mode, $\mathcal{R}e\langle\hat{b}_{\alpha=1}\rangle$, and spectrum (inset). **d**, $\mathcal{R}e\langle\hat{a}_1\rangle$ for the same coupling strength as in **b**, yet only for a single pair of light and matter modes. Inset: corresponding spectrum. Adapted from [Mor23a].

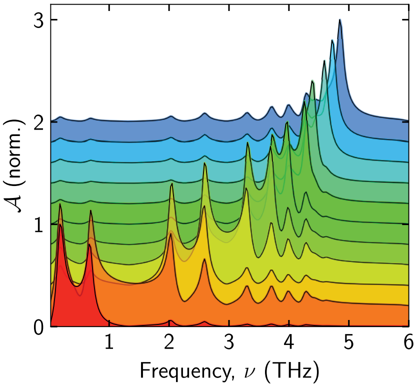

Figure 5.17 | Magnetoplasmon spectra. Calculated spectra of the expectation values of the polarization of the magnetoplasmon modes $0 \leq \alpha \leq 10$. The spectra are vertically offset by a value of 0.2, for clarity. Adapted from [Mor23a].

the remarkably strong light-matter coupling, $\Omega_{\mathrm{R},1,\alpha}$, which results in a total spectral bandwidth spanning over 6 optical octaves from as low as 0.05 THz to as high as 6 THz.

Driven by ultrastrong and deep-strong coupling, the polarization of the first magnetoplasmon polariton mode with a frequency of $\nu_{\mathrm{MP},\alpha=1} = 1.2\,\mathrm{THz}$ displays a similar intricate time-domain structure (Fig. 5.16**c**). Its spectrum reveals four significant local maxima spanning from 0.18 to 2.59 THz, accompanied by less pronounced higher-frequency maxima (Fig. 5.16**c**, inset). These dynamics are in stark contrast to the dynamics of a single pair of light-matter coupled modes, with $\Omega_{\mathrm{R}}^{\mathrm{s}}/\omega_{\mathrm{s}} = 3.19$. Here the cavity field features only the lower and upper polariton resonances, without additional features in its spectrum (Fig. 5.16**d**).

Owing to the strong coupling of multiple magnetoplasmon modes to a shared cavity mode, the magnetoplasmons influence each other, mediated by the cavity. This interaction results in strong mixing of the previously orthogonal matter modes. As a result, the dominant frequencies in their polarizations reflect the spectral characteristics of all magnetoplasmon polaritons simultaneously (Fig. 5.17). Although the spectral weight of each magnetoplasmon mode is primarily centred around its intrinsic resonance frequency, they all share the same local maxima. This is a characteristic signature of multi-mode non-resonant deep-strong light-matter coupling and the strong back-action of the cavity vacuum field on the matter system.

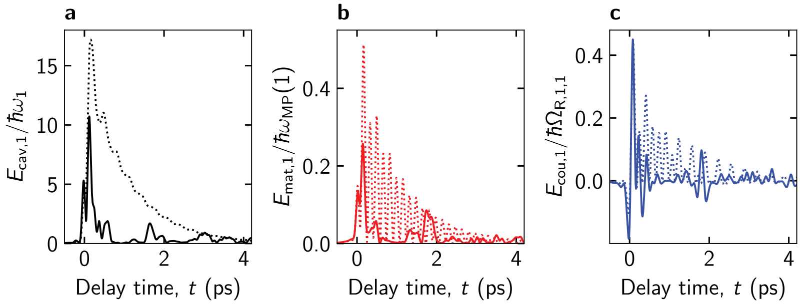

Figure 5.18 | Energy dynamics of extremely strong multimode coupling. **a**, Energy of the first cavity mode for the full calculation (solid curve) and the single-mode reference (dashed curve) as in 5.16. **b**, Energies of the first magnetoplasmon mode (solid curve) and cyclotron resonance (dashed curve) for the two cases. **c**, Corresponding coupling energies between the cavity mode and the respective matter mode. Adapted from [Mor23a].

The distinction between the single-mode and multi-mode coupling regimes becomes even more pronounced when examining the dynamics of energy redistribution (Fig. 5.18). In the case of a single pair of modes, the cavity energy $E_{\mathrm{cav},1}$, the energy of the matter system $E_{\mathrm{mat},1}$ and the energy stored in the coupling itself $E_{\mathrm{cou},1}$, all exponentially decay upon excitation (Fig. 5.18, dotted curves). During the decay, the subsystems exchange energy periodically at the rate of $\Omega_{\mathrm{R}}^{\mathrm{s}}$, resulting in an oscillatory modulation of the decaying energies. However, in our system with a large number of participating magnetoplasmon matter modes, the dynamics of all energies exhibit a much more irregular behaviour (Fig. 5.18, solid curves). A single exponential decay is no longer observable, instead the cavity energy, the energy of the first magnetoplasmon and its respective coupling energy exhibit a sharp decay after the initial rise upon excitation and a second, local maximum at $t = 1.8\,\mathrm{ps}$. Although this dynamic seems to contradict energy conservation, the energy is simply stored in the coupling of the other 20 magnetoplasmons, not displayed in the figure, highlighting the complex nature of the multi-mode coupled state.

Conclusion

Cooperative, non-resonant multi-mode coupling allows one to overcome the limitations of resonant light-matter coupling and reach record-breaking light-matter coupling strengths. To achieve this, we designed a new, highly compact resonator metasurface capable of custom-tailoring multiple plasmon resonances and optical modes, resulting in an ultrabroadband spectrum of Landau cavity polaritons spanning as much as 6 optical octaves. As a result, the vacuum ground state of the system is highly squeezed and hosts an unprecedentedly large population of 1.17 virtual photons and 1.06 virtual magnetoplasmon excitations. The equivalent coupling strength of $\Omega_{\mathrm{R}}^{\mathrm{s}}/\omega_{\mathrm{s}} = 3.19$ surpasses the previous deep-strong coupling strength records [Bay17, Mue20] almost by a factor of 2. Furthermore, the exceptionally strong coupling of multiple electronic modes to a common cavity mode allows for the hybridization of otherwise orthogonal matter states. This capability might be extended to interactions between various systems such as magnons, phonons, or Dirac electrons, enabling the mixing of these excitations. The combination of the highly non-adiabatic switching mechanism, which is also applicable to this resonator structure as presented in the next chapter 6, along with the remarkable records achieved for coupling strength and vacuum photon population, brings us closer to the exciting prospect of experimentally feasible detection of vacuum radiation from these samples.

Chapter 6

Non-adiabatic switch-off of deep-strong light-matter coupling

The interaction of vacuum fields with matter can result in extreme light-matter coupling in the deep-strong coupling regime, as exemplified in the last chapter. Its exotic ground state gives rise to many fascinating equilibrium properties, due to the strongly squeezed vacuum ground state and a non-vanishing virtual photon population. However, even more remarkable physics is anticipated to unfold on subcycle timescales, where ultrafast control of light-matter coupling opens up novel avenues to manipulate vacuum-induced effects. This offers exciting new perspectives for non-adiabatic quantum optics and might ultimately facilitate the release of Unruh-Hawking like radiation [Lib07, Gü09, Gar13]. Here, a non-adiabatic change of the vacuum ground state is postulated to transmute the virtual photon population into real photons. A faster switching process or higher coupling strengths (see chapter 2.1) will maximise the number of emitted photons. However, up to now, this regime has been limited to $\Omega_{\mathrm{R}}/\omega_{12} \leq 0.1$ [Gü09].

In the following, we delve into the fascinating dynamics that arise when electrons, initially deep-strongly coupled, are rapidly stripped of their photon dress. To this end, we combine our ultrastrongly and deep-strongly coupled sample structures with a new, subcycle switching mechanism, that, for the first time, enables controlled and complete decoupling of light and matter modes using an optical femtosecond switching pulse. Upon photoactivation of the switching element, the fundamental

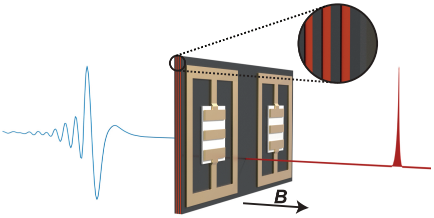

Figure 6.1 | Resonator scheme for switchable deep-strong light–matter coupling. THz resonators (gold shapes) coupled to the cyclotron resonance of 2DEGs (red layers, also see magnification), biased by the magnetic field B (black arrow), and interrogated by THz transients (blue waveform). The switch element (white patch) is photoexcited by a near-infrared femtosecond pulse (red shape). Adapted from [Hal20].

cavity mode collapses, and results in an abrupt quench of the polariton modes. This strongly subcycle breakdown is accompanied by characteristic sub-polariton-cycle oscillations — a unique signature of this novel regime characterized by extreme light-matter dynamics.

The work presented in this chapter is published as a coverstory in *Nature Photonics* [Hal20]. Additional details on the development of the switching mechanism can also be found in the PhD thesis of my co-first-author Maike Halbhuber [Hal21]. The main findings of the article are presented in the following, together with new optimizations for vacuum photon emission.

6.1. Switchable THz resonator structures

While there are established means [Has17] of electrically [Shr11, Che06], mechanically [Zhu12, Shi17] or thermally [Sin12, Kel18] activated switching mechanisms for plasmonic THz metasurfaces, only optical activation [Pad06, Che08, Kaf12, Liu15, Hu19] is capable of an ultrafast and non-adiabatic switch-off of resonator modes.

We base our switching design on the THz resonator introduced in chapter 2.5. Here, the double gap resonator enhances the vacuum field in its two central capacitive gaps (Fig. 2.7). To maximise the light-matter coupling, the QW stack is placed

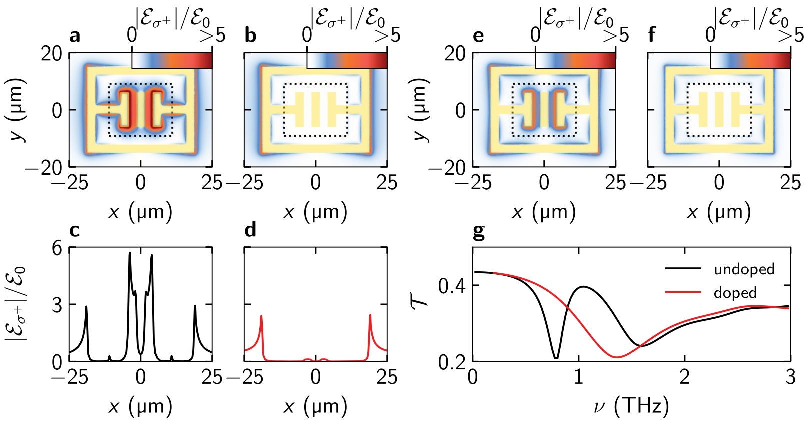

Figure 6.2 | Resonator field profiles before and after photoexcitation. **a**, Calculated enhancement of the right-circularly polarized near-field component $|\mathcal{E}_{\sigma^+}|/\mathcal{E}_0$ of the LC mode, relative to the far-field amplitude, $\mathcal{E}_0$, at a depth of $z = -200\,\mathrm{nm}$, for an undoped switching patch (dashed lines) and **b**, for a doped switching patch. **c**, Near-field enhancement in the QW plane along $y = 0$ without photoexcitation and **d**, with photoexcitation. **e,f**, Same as **a** and **b**, but for the DP mode. **g**, Transmission spectra for a doped and an undoped switching patch, respectively. Adapted from [Hal20].

directly below the resonator to maximise the overlap. Thus, changing the dielectric properties of this region will strongly influence the coupling. We make use of this fact and introduce an undoped $\mathrm{In_{0.55}Ga_{0.45}As}$ patch (dimensions: $10\,\mu\mathrm{m}\times 22\,\mu\mathrm{m}$) between the capacitive resonator region and the QWs (Fig. 6.1, white patch).

The bandgap of 0.73 eV of the semiconductor material allows for the selective excitation of charge carriers only in the switching patch using femtosecond switching pulses with a photon energy of 1.03 eV and a pulse duration of 70 fs. Full saturation of the patch with the employed pulses corresponds to a photoexcited plasma with an electron-hole pair density of $\rho_{\mathrm{switch}} = 3.5 \times 10^{18}\,\mathrm{cm^{-3}}$, rendering the patch quasi-metallic in the THz regime. We conduct finite-element frequency-domain simulations (see appendix C) to observe the influence of the photoexcited plasma on the resonator modes (Fig. 6.2). Before photoactivation, the double gap resonators feature a strong

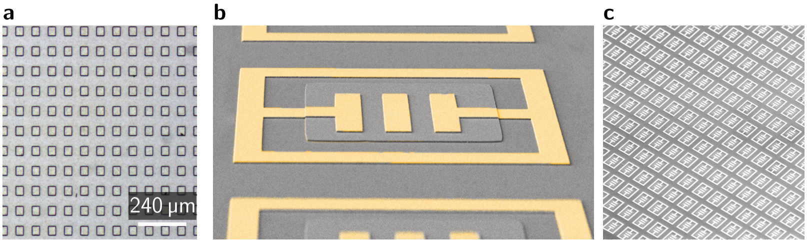

Figure 6.3 | Fabricated switchable double gap resonator metasurface. **a**, Light microscope picture of an array of InGaAs patches. **b**, Scanning electron microscope picture of a single resonator and InGaAs patch. The resonator is coloured golden for better visibility. **c**, Scanning electron microscope picture of an array of switchable double gap resonators.

field enhancement in the central two gaps (Fig. 6.2**a,c**). Upon exciting the patch (Fig. 6.2**b**, dashed lines), the field enhancement of the LC mode below the patch is reduced by 95%, whereas the near fields outside the patch stay unaffected (Fig. 6.2**b,d**). These data show that the photoexcited plasma is efficient to screen the near field in the resonator gap, thereby collapsing the LC mode, which in turn results in the collapse of the coupling between the LC resonator mode and the QW stack. While the near-field enhancement of the second mode, the DP mode, is also reduced by 95% below the patch, the near-field enhancement of the DP mode outside the patch region stays mostly unaffected (Fig. 6.2**e,f**). The simulated far-field response does not show a collapse of the DP mode, only a redshift in frequency (Fig. 6.2**g**). On the contrary, the complete collapse of the LC mode is also evident in the far field.

As a first evaluation of our concept, we employ a structure only featuring the switchable resonator structures and no QWs. Pictures of the fabricated structures are displayed in Figure 6.3. Details on the fabrication are included in the appendix A. To test the structure, we measure the instantaneous THz response of the sample during switching. To this end, the THz pulse and the switching pulse are shifted with respect to each other by a delay time, t_D, and the electro-optic detection is performed at the delay time t relative to the THz pulse (Fig. 6.4).

Upon photoexcitation, a strong pump-induced change, $\Delta\mathcal{E}$ (Fig. 6.5**a**) of the transmitted THz field, $\mathcal{E}$, emerges. Sweeping t_D probes the switching behviour of the resonator

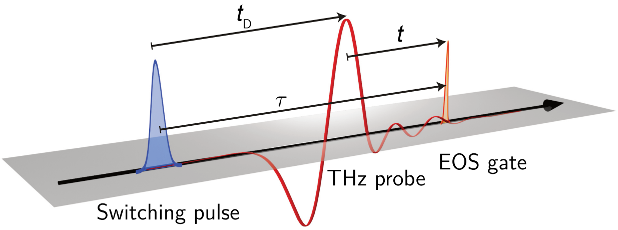

Figure 6.4 | Schematic of excitation. The switching pulse (blue pulse) is shifted with respect to the THz transient (red waveform) by a delay time t_D, and electro-optic sampling (EOS) is performed at a delay time t (orange pulse). Adapted from [Hal20].

during different phases after THz excitation and reveals a complex temporal structure along the diagonal $t = -t_D$. Interpreting such dynamics, that exhibit variations on a subcycle scale, extends beyond the scope of equilibrium or quasi-equilibrium settings where response functions change slowly compared to the duration of one oscillation cycle of light. Thus, we adopt the formalism developed by Kindt and Schmuttenmaer [Kin99] to extract the instantaneous linear response function and transform the data into a new time frame where $\tau = t + t_D$ represents a constant delay between the switching and electro-optic detection pulses (Fig. 6.4). Subsequently, the acquired time-domain data are subjected to a Fourier transform along the time axis t, while maintaining a constant value for τ (Fig. 6.5**b**). This transform allows us to extract the instantaneous switching response of the system and analyse its dynamics on a subcycle scale.

Once more, the data underscores the spectral specificity inherent to the switching concept. Notably, the primary impact is observed on the narrowband LC cavity mode at 0.8 THz, while the DP mode experiences only a marginal redshift and a slight broadening in frequency. A detailed analysis of the differential transmission $\Delta\mathcal{T} = \mathcal{T}(\tau) - \mathcal{T}(\tau = -2\,\mathrm{ps})$ of the LC mode (Fig. 6.5**c**, black curve) reveals an initial drop in transmission, which is attributed to the increased overall THz absorption caused by the presence of carriers in the switching patch. This process is reversed after the first 100s of fs from whereon the transmission monotonically increases with time. In contrast, the transmission at a reference frequency of 2.1 THz remains largely unchanged throughout the switching process (Fig. 6.5**c**, red curve).

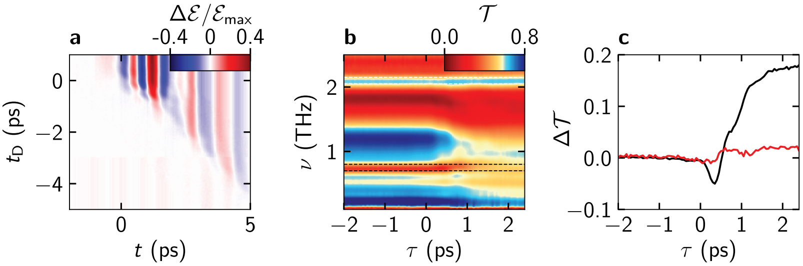

Figure 6.5 | Switching dynamics of the bare resonator. **a**, Pump-probe THz signal during femtosecond photoexcitation. The charge carrier concentration resulting from femtosecond photoexcitation is $3.5 \times 10^{18}\,\mathrm{cm}^{-3}$. **b**, Corresponding transmission spectra, in the τ-frame. **c**, Black curve: differential transmission $\Delta\mathcal{T}$ of the LC mode extracted within the frequency window outlined in panel **b** by dashed black lines. Red curve: differential transmission extracted within the frequency window outlined in panel **b** by dashed white lines, for reference. Adapted from [Hal20].

6.2. Subcycle switch-off dynamics

With a successful demonstration of our switching concept, we put it to the test with two coupled structures. The first structure S3sw, features three QWs with a doping density of $\rho = 1.75 \times 10^{12}\,\mathrm{cm}^{-2}$ per QW, coupled to the switchable double gap resonator. We characterize the sample in equilibrium before switching by measuring the THz transmission as a function of the cyclotron frequency ν_c (Fig. 6.6**a**). The spectra show the expected anticrossing, with a lower polariton (LP) branch emerging from the cyclotron resonance at low frequencies and an upper polariton (UP) resonance starting at 1.35 THz for $\nu_\mathrm{c} = 0\,\mathrm{THz}$. Here we use a single-mode Hamiltonian to reduce the complexity to the most relevant modes, as additional modes only produce minor corrections to the spectra. The analysis reveals a coupling strength of $\Omega_\mathrm{R}/\omega_\mathrm{c} = 0.57$, equivalent to a vacuum ground state population of 0.1 virtual photons. Additionally, the bare, uncoupled cyclotron resonance is visible for $\nu = \nu_\mathrm{c}$.

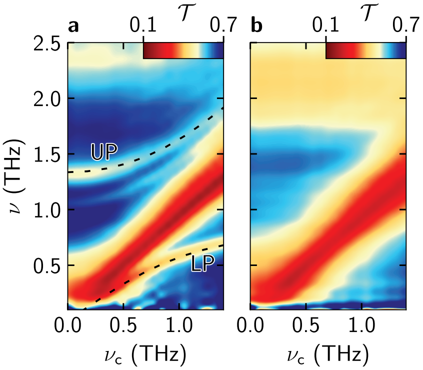

Figure 6.6 | Steady-state switching of ultrastrong coupling. **a**, THz transmission of the 3-QW sample S3sw, including the Hopfield fit for the LP and UP with a coupling strength of $\Omega_R/\omega_c = 0.57$. **b**, 2 ps after excitation of the switching patch. Adapted from [Hal20].

Steady-state spectra

Next, we record the same spectra after photodoping of the switching patch, exciting the sample 2 ps before the maximum of the THz pulse at a time delay of $t_D = 2$ ps (Fig. 6.6**b**). Here we observe several large changes, as both polariton resonances are completely absent, evidencing the full collapse of the ultrastrong coupling. As already observed for the bare resonator, the dipolar cavity mode slightly redshifts as well upon activation of the switching patch, resulting in the observed reduced transmission above 1.6 THz. Other spectral features, such as the bare cyclotron resonance, remain unaffected, showcasing the minimally invasive nature of the switching concept.

As a next step, we test the structure L6, featuring 6 QWs and characterized in equilibrium in chapter 2.6. This structure features the L-gap resonator structures (Fig. 6.7**a**), the positive resonator counterpart to the negative structure we started with in chapter 5. Likewise, this resonator features a fundamental LC mode with a frequency of $\nu_{LC} = 0.52$ THz and a higher dipolar mode with a frequency of $\nu_{DP} = 1.95$ THz. The vacuum field enhancement of the LC mode is located in two capacitive gaps, under which two InGaAs patches for switching are placed (marked by dashed lines). Our finite-element frequency-domain simulations show again a collapse of the LC mode upon doping the patches (Fig. 6.7**b**).

The steady-state transmission before switching shows an LP and UP resonance (Fig. 2.10 and 6.7**c**), with a coupling strength of $\Omega_R/\omega_c = 1.3$, equivalent to a vacuum

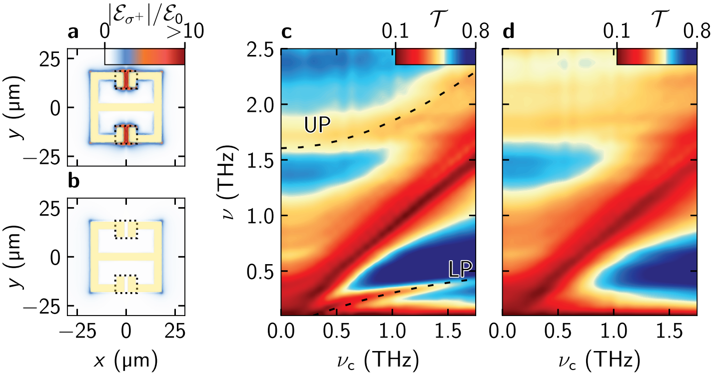

Figure 6.7 | Steady-state switching of deep-strong coupling. **a**, Electric near-field distribution of the LC mode of a L-gap resonator for $\nu = 0.52\,\mathrm{THz}$. **b**, After switching patch activation. **c**, THz transmission of the 6-QW sample L6, including the Hopfield fit for the LP and UP with a coupling strength of $\Omega_\mathrm{R}/\omega_\mathrm{c} = 1.3$. **d**, 2 ps after excitation of the switching patch. Adapted from [Hal20].

ground state population of 0.32 virtual photons. Likewise, 2 ps after photodoping the switching patches, both polariton resonances have fully vanished, while the bare cyclotron resonance remains unaffected (Fig. 6.7**d**). These data are the first demonstration of switching deep-strong coupling in general, and in particular by optical means and on an ultrafast time scale.

Subcycle dynamics

Next, we will explore how the transition from deep-strong coupling to uncoupled modes takes place on a subcycle time scale. Therefore, we photoexcite the sample S3sw at $t_\mathrm{D} = 0\,\mathrm{ps}$, where the electric field of the THz pulse has its maximum (Fig. 6.8**a**). The pump-induced change $\Delta\mathcal{E} = \mathcal{E} - \mathcal{E}_\mathrm{unswitched}$ (red curve) emerges in the first half-cycle of the oscillating field, increases in amplitude and becomes comparable to $\mathcal{E}$ during the trailing oscillations ($t > 0.5\,\mathrm{ps}$), as the polariton resonances are suppressed.

A systematic scan of $\Delta\mathcal{E}$ as a function of t_D (Fig. 6.8**b**) reveals complex switching dynamics along $t = -t_\mathrm{D}$ as the exchange of energy between light and matter is

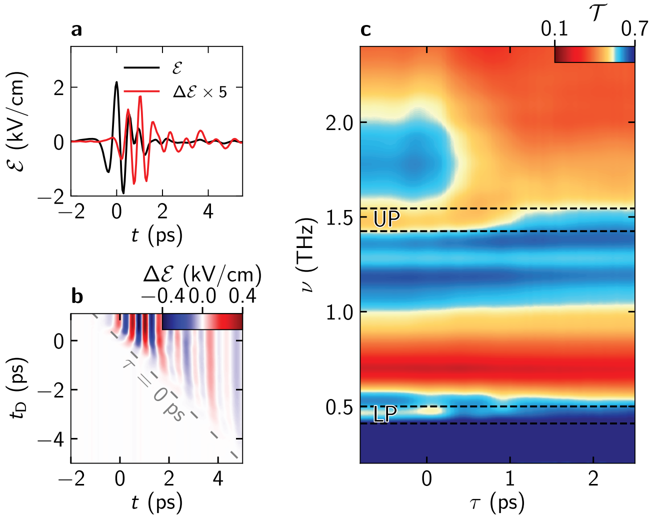

Figure 6.8 | Subcycle switching dynamics of USC. **a**, Transmitted THz transient before excitation (black curve) and pump–probe signal $\Delta\mathcal{E}$ for $t_D = 0$ ps (red curve). **b**, $\Delta\mathcal{E}$ as a function of the EOS delay time, t, and the pump–probe delay time, t_D. The grey diagonal line ($t = -t_D$) indicates a constant delay $\tau = t + t_D = 0$ ps (see **a**). **c**, Transmission spectra obtained by Fourier transform of the data in **b**, along lines of constant τ. The dashed lines indicate the FWHM of the polariton resonances centred at a frequency of 0.48 THz and 1.49 THz. Adapted from [Hal20].

interrupted in various phases of the polariton oscillations.

To extract the instantaneous transmission spectra, we transform the data into the τ-time frame and perform a Fourier transform along t. The evolution of these spectra now shows the transition from the light-matter coupled state to the decoupled state, with subcycle resolution (Fig. 6.8**c**). The data reveals that both polaritons display complex switch-off dynamics featuring multiple oscillation components. The change in transmission, $\Delta\mathcal{T}$ for the lower polariton resonance (Fig. 6.9**a**, solid black curve and circles) reveals an initial short increase of transmission for delay times $\tau < 0$ ps, followed by a sharp minimum at $\tau \approx 0$ ps. These dynamics are followed by a rapid increase in transmission and multiple further oscillations before the transmission

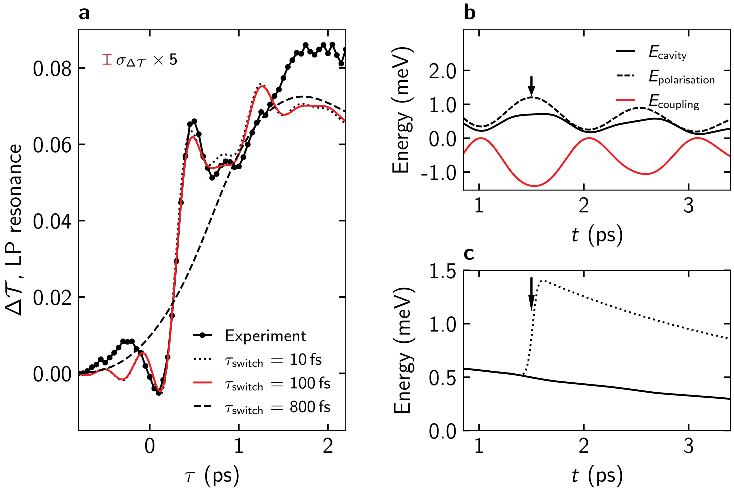

Figure 6.9 | Sub-polariton-cycle switching oscillations. a, Differential transmission $\Delta\mathcal{T}$ of the LP (solid black curve and circles) extracted within the highlighted spectral range in Figure 6.8 and calculation for a switching time of 100 fs (red curve). Dotted and dashed curves: calculations of $\Delta\mathcal{T}$ for switching times of 10 fs, and 800 fs, respectively. The error bar indicates the standard deviation of the experimental signal, multiplied by 5. **b**, Energy of the cavity (solid black curve), polarization energy (dashed black curve) and coupling energy (red curve) when only the LP is excited. The black arrow marks a local extremum of these energies. **c**, Decay of the total energy without switching (solid black curve) and for switching when the coupling energy is minimized (dotted black curve). Adapted from [Hal20].

reaches its final value. The frequency response of the oscillations contains components that exceed the frequency of the LP resonance several times.

In order to explain the high-frequency oscillatory dynamics in the response function, observed for the rapid deactivation of light-matter coupling, we will expand the time-domain simulations described in chapters 3 and 5 to include the dynamical switch-off process of the resonator by introducing a set of time-dependent parameters.

With Heisenberg's equation of motion and a mean-field treatment we obtain for the equilibrium state,

$$\frac{d}{dt}\alpha_{\mathrm{LC}} = -i\omega_{\mathrm{LC}}\alpha_{\mathrm{LC}} - \gamma_{\mathrm{LC}}\alpha_{\mathrm{LC}} - i\Omega_{\mathrm{R}}\left[\beta\left(t\right) + \beta^{*}\left(t\right)\right] - 2iD\left[\alpha_{\mathrm{LC}}\left(t\right) + \alpha^{*}_{\mathrm{LC}}\left(t\right)\right] \\ + \kappa_{\mathrm{LC}}\mathcal{E}_{\mathrm{ext}}\left(t\right), \tag{6.1}$$

$$\frac{d}{dt}\alpha_{\mathrm{DP}} = -i\omega_{\mathrm{DP}}\alpha_{\mathrm{DP}} - \gamma_{\mathrm{DP}}\alpha_{\mathrm{DP}} + \kappa_{\mathrm{DP}}\mathcal{E}_{\mathrm{ext}}\left(t\right), \tag{6.2}$$

$$\frac{d}{dt}\beta = -i\omega_{\mathrm{c}}\beta - \gamma_{\mathrm{c}}\beta - i\Omega_{\mathrm{R}}\left[\alpha_{\mathrm{LC}}\left(t\right) + \alpha^{*}_{\mathrm{LC}}\left(t\right)\right], \tag{6.3}$$

with the damping terms γ_{j} and γ_{c} for the cavity and matter modes, respectively, as well as a scaling factor for each cavity mode's coupling to the external field by κ_{j}. $D = \frac{\Omega_{\mathrm{R}}^2}{\omega_{\mathrm{c}}}$ represents the diamagnetic term. Coupling to the second cavity mode is omitted here, as it is negligibly small.

As the switching mechanism is based on the screening of the electric near field by the charge carrier plasma generated through optical excitation, we have to take the plasma generation dynamics into account. The femtosecond excitation pulses have a FWHM duration of 70 fs and create a plasma with a carrier density of $\rho_{\mathrm{switch}} = 3.5 \times 10^{18}\,\mathrm{cm}^3$. This results in a (3D) plasma frequency of $\nu_{\mathrm{p}} = 80\,\mathrm{THz}$, and a build-up of screening within $t_c = \nu_{\mathrm{p}}^{-1} = 12.5\,\mathrm{fs}$ [Hub01]. Thus, it is safe to assume, that the near field will collapse within approximately the duration of the switching pulse.

We introduce the decoupling mechanism into the differential equations by a set of time-dependent parameters (table 6.1), which start at their equilibrium value, X^{i}, transitioning to their value after switching, X^{f}. We parametrize this transition by a switching time τ_{switch}, leading to

$$X\left(t + t_{\mathrm{D}}\right) = X^{\mathrm{i}} + \frac{\left(X^{\mathrm{f}} - X^{\mathrm{i}}\right)}{2}\left(1 + \frac{2}{\sqrt{\pi}}\int_{0}^{t+t_{\mathrm{D}}} e^{-\left(\frac{\sqrt{4\ln 2}}{\tau_{\mathrm{switch}}}\left(t'_{\mathrm{D}}\right)\right)^2} \mathrm{d}t'_{\mathrm{D}}\right). \tag{6.4}$$

The switching process collapses the vacuum Rabi frequency $\Omega_{\mathrm{R}}(t + t_{\mathrm{D}})$ to 0 and changes the damping parameters, $\gamma_{\mathrm{j}}\left(t + t_{\mathrm{D}}\right)$, as well as the coupling to the external field, $\kappa_{\mathrm{j}}\left(t + t_{\mathrm{D}}\right)$. For the best fit, we reduce the coupling to the external field of the LC mode by 50%. Activation of the switching patch also shifts the frequency of the DP resonator mode, which is added to the simulation, as well as an increase in

$\mathbf{X(t+t_D)}$	**initial value** X^{i}	**final value** X^{f}
$\Omega_{\mathrm{R}}/\omega_{\mathrm{c}}$	0.57	0.0
ν_{DP} (THz)	2.2	1.8
γ_{DP} (THz)	$0.20 \cdot 2\pi$	$0.30 \cdot 2\pi$
κ_{LC}	0.25	0.13
κ_{DP}	1.0	1.5

Table 6.1: Parameters used for the USC switch-off model.

far-field coupling by 50%. All variable parameters are listed with their respective initial and final values in table 6.1.

The theoretical calculations closely capture the dynamics observed in the experimental data (Fig. 6.9, red curve). This includes the initial reduced transmission, the subsequent steep rise, and the local reduction between $\tau = 0.5\,\mathrm{ps}$ and $1.1\,\mathrm{ps}$. The calculated dynamic for $\tau > 1.5\,\mathrm{ps}$ deviates slightly from the experimental curve, as potential changes in higher resonator modes are not fully included in the model. Changes in the damping, frequency or far-field coupling of these higher resonator modes could in principle alter the dynamics, but are not accounted for here for simplicity. However, the model displays the impact of τ_{switch} on the observed dynamics. The transition dynamics match only for a sufficiently fast switching time of $\tau_{\mathrm{switch}} \leq 100\,\mathrm{fs}$ (Fig. 6.9, black curve), whereas for larger switching times the oscillations vanish and the transitions resembles a more adiabatic transition from initial to the final transmission coefficient. This change of the dynamics allows us to quantify an upper bound of the switching time of $\tau_{\mathrm{switch}} = 100\,\mathrm{fs}$, which corresponds to just 5% of the LP mode oscillation period, clearly evidencing the strong non-adiabatic character of the switch-off process.

Energy dynamics

Our theory also allows us to investigate the internal energy dynamics of the ultra-strongly couple state, responsible for the observed subcycle oscillations. Due to the extremely strong coupling in the USC regime, energy is periodically exchanged not only between the cavity and the matter mode, but a sizeable part can also be stored in the coupling mechanism itself. This coupling energy, E_{coupling}, is proportional to the in-phase quadratures of the cavity field and the polarisation and can exceed their individual energies, E_{cavity} and $E_{\text{polarisation}}$, respectively. The mean-field energies are given by

$$\langle E_{\text{coupling}}\rangle = \hbar\Omega_{\mathrm{R}}\left(\alpha_{\mathrm{LC}} + \alpha_{\mathrm{LC}}^{*}\right)\left(\beta + \beta^{*}\right), \tag{6.5}$$

$$\langle E_{\text{cavity}}\rangle = \hbar\omega_{\mathrm{LC}}|\alpha_{\mathrm{LC}}|^{2} + \hbar D\left(\alpha_{\mathrm{LC}} + \alpha_{\mathrm{LC}}^{*}\right)^{2}, \tag{6.6}$$

$$\langle E_{\text{polarisation}}\rangle = \hbar\omega_{\mathrm{c}}|\beta|^{2}. \tag{6.7}$$

When the fast switching process switches off the transfer of energy, the subsequent dynamics of the uncoupled cavity and electronic polarization are determined by the instantaneous field amplitudes at the moment of switching. As the energy is exchanged with the rate of Ω_{R}, which can oscillate at a faster rate than a single polariton oscillation cycle in the USC or DSC regime, the observed response function also exhibits rapid oscillations.

The influence of the exact switching time during the energy exchange oscillation cycle on the observed dynamics can be demonstrated with an instructive example: When we excite the lower polariton mode with a coherent THz field ($\hat{p}_{\mathrm{LP}} = Ae^{i\omega t}$), the mean-field expectation values are given by $\alpha_{\mathrm{LC}} = w_{\mathrm{LP}}Ae^{i\omega t} - y_{\mathrm{LP}}Ae^{-i\omega t}$, and $\beta = x_{\mathrm{LP}}Ae^{i\omega t} - z_{\mathrm{LP}}Ae^{-i\omega t}$. The Hopfield coefficients then dictate that the field quadratures have opposite phases and $\left(\alpha_{\mathrm{LC}} + \alpha_{\mathrm{LC}}^{*}\right)\left(\beta + \beta^{*}\right) < 0$. Thus, $\langle E_{\text{cavity}}\rangle$ and $\langle E_{\text{polarisation}}\rangle$ oscillate in phase, while $\langle E_{\text{coupling}}\rangle$ oscillates out of phase and is negative (Fig. 6.9**b**). Due to the ultrastrong coupling, the magnitude of $\langle E_{\text{coupling}}\rangle$ is comparable to the other energy components of the system.

In the absence of switching, the total energy decays exponentially over time (Fig. 6.9**c**, black line). In the case of switching, the energy oscillations result in two different scenarios: if the switching happens at a local minimum of $\langle E_{\text{coupling}}\rangle$ (black arrow in Fig. 6.9**c**), the negative energy of the coupling mechanism is removed due to the collapse of the coupling, and consequently the overall energy in the system is increased (dotted curve in in Fig. 6.9**c**). If the switch-off occurs at a local maximum of $\langle E_{\text{coupling}}\rangle$, the overall energy is decreased, as $\langle E_{\text{cavity}}\rangle$ also collapses and subsequently the overall energy of the system is decreased. As the state of the system oscillates between these two extrema, this causes the observed oscillations in the response function.

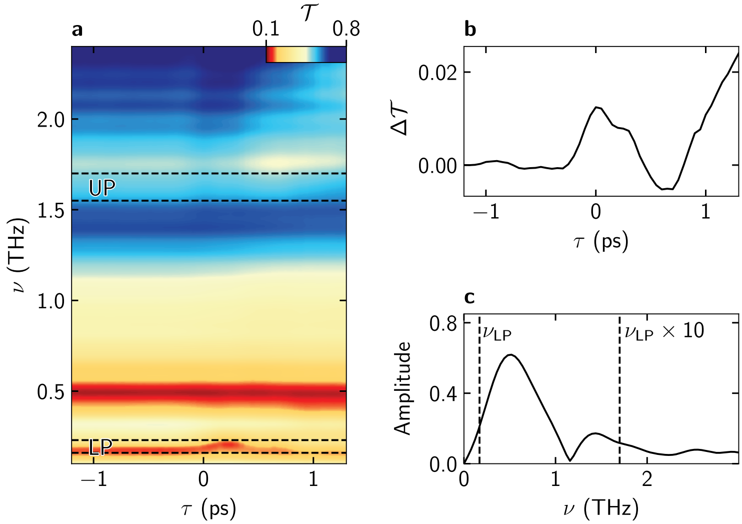

Figure 6.10 | Subcycle switching dynamics of DSC. a, Transmission spectra of the 6-QW structure as a function of pump-probe delay time, τ, at the anti-crossing point. The dashed lines mark the frequency windows of the lower and upper polariton resonances at 0.17 THz and 1.62 THz, respectively. **b**, Differential transmission $\Delta\mathcal{T}$ at the UP frequency. **c**, Spectrum of the switching dynamics of the lower polariton. Vertical dashed lines indicate the resonance frequency of the LP, ν_{LP}, and $10 \times \nu_{\mathrm{LP}}$, for reference. Adapted from [Hal20].

Subcycle dynamics of DSC switch-off

Similar switch-off dynamics can be observed for the deep-strongly coupled sample L6 (Fig. 6.10**a**). Here again, both polariton resonances are switched off on a strongly subcycle scale (Fig. 6.10**b,c**). The differential transmission at the upper polariton (Fig. 6.10**b**) exhibits a short-lived increase, which then reverses to a decrease, followed by a subsequent steep increase approaching its final value. This behaviour is similar to what was observed in sample S3sw, yet the transmission change at the frequency of the lower polariton resonance shows even more extreme oscillations which contain frequency components exceeding the LP frequency by an order of magnitude (Fig. 6.10**c**). Here, the 100 fs switch-off time corresponds to only 2% of the oscillation period of the lower polariton mode, showcasing again the strongly non-adiabatic nature of the process.

Further discussions of the energy dynamics and the error estimation can be found in [Hal20, Hal21].

6.3. Switching the compact resonator array

In order to maximise the density of virtual photons that can be emitted during a non-adiabatic switch-off of the coupling, in chapter 5, we developed a new maximally compact resonator design (butterfly) with over one virtual photon, per resonator. Yet, to release these virtual photons, we need to combine the resonator structure with the switching design demonstrated in this chapter.

To continue maximising the virtual photon output of the structure, we go one step further in optimizing the switching mechanism. As the light-matter coupling takes place in the region of the strongest field enhancement, upon switching off the coupling, the virtual photon emission is expected to originate from there as well. Thus, the photodoped switching patches in this region will impair the emission of the released photons into the far field, as the patch will reflect or absorb them. To remove this obstacle, we redesigned the placement of the switching patches for the maximally compact butterfly resonator. Here, the switching patches no longer directly “disable” the capacitive gap, but are replaced by stripes parallel to the gold stripes in x-direction (Fig. 6.11**a,b**, dashed lines). Upon photodoping the stripes “short” the resonators in y-direction and, according to finite-element frequency-domain simulations, also result in a collapse of the LC mode. The strong near-field enhancement of the fundamental LC resonator mode in the capacitive gap (Fig. 6.11**a** and **c**, black curve) is reduced by 92% by activating the switching stripes (Fig. 6.11**b** and **c**, red curve). The collapse of the LC mode is also evident in the far-field response of the resonator array (Fig. 6.11**d**). Here, the pronounced transmission maximum at the resonance frequency of the LC mode is absent in the transmission data after switching. Contrary to previous resonators, here also the higher DP mode is significantly reduced in amplitude by 38% and experiences a resonance frequency blue shift by 58%. This behaviour is actually beneficial, as

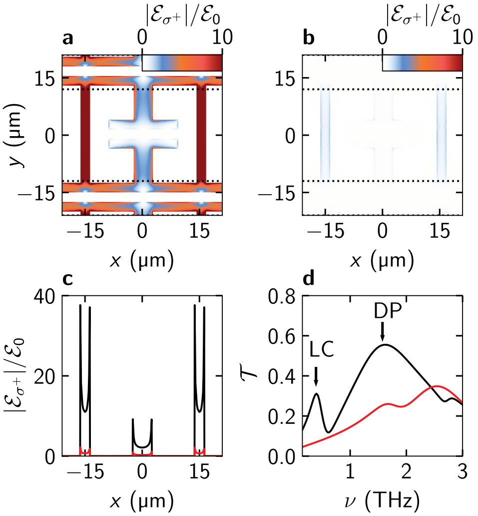

Figure 6.11 | Butterfly resonator field profiles before and after photoexcitation. **a**, Calculated enhancement of the right-circularly polarized near-field component $|\mathcal{E}_{\sigma^+}|/\mathcal{E}_0$ of the LC mode, relative to the far-field amplitude, $\mathcal{E}_0$, at a depth of $z = -200\,\text{nm}$, for an undoped switching layer and **b**, for a doped switching layer. **c**, Near-field enhancement in the QW plane along $y = 0$ without photoexcitation (black curve) and with photoexcitation (red curve). **d**, Transmission spectra for a doped and an undoped switching patch, respectively.

for the highest achieved vacuum photon numbers, the coupling to the DP mode contributes a significant number of virtual photons.

We put this enhanced switching concept to the test and fabricated a structure with the switchable butterfly metasurface (Fig. 6.12). The recorded instantaneous response of the bare resonator as a function of the delay time τ is displayed in Figure 6.13**a**. After photoexcitation ($\tau > 0\,\text{ps}$), the overall transmission of the sample is slightly reduced, whereas the LC and DP mode display a rapid and drastic reduction in transmission and vanish into the background transmission (Fig. 6.13**b**,**c**). The switch-off dynamics happen on the same time scale as for the double gap resonator (see Fig. 6.5), demonstrating that placing the switching patch in the field enhancement gap of

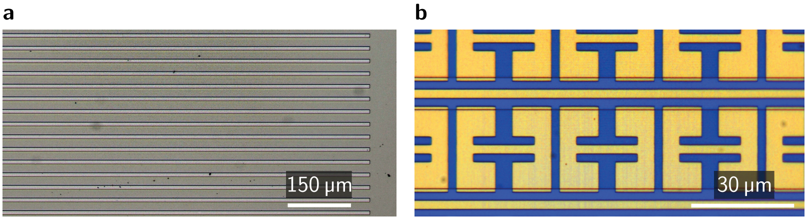

Figure 6.12 | Fabricated switchable butterfly metasurface. **a**, Light microscope picture of InGaAs stripes for the resonators. **b**, Picture of the finished metasurface array including the switching stripes.

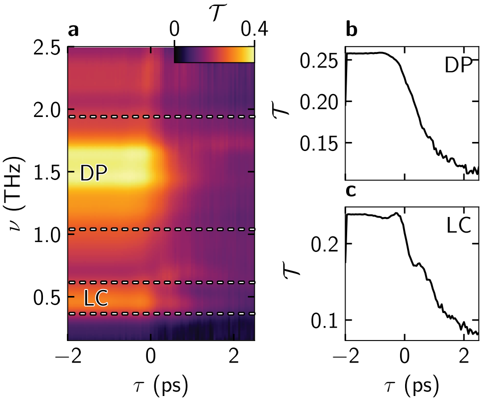

Figure 6.13 | Switching dynamics of the bare butterfly resonator. **a**, Transmission spectra as a function of pump-probe delay time, τ. The dashed lines mark the frequency windows of the LC and DP cavity mode, respectively. **b**, Transmission of the DP mode extracted within the frequency window outlined in panel **a** by dashed lines. **c**, Transmission of the LC mode, respectively.

the resonator is not necessary for an ultrafast switch-off of the resonator near-field enhancement.

We test whether this switching concept can successfully switch-off light-matter coupling by conducting finite-element frequency-domain simulations of a sample featuring one QW with and without doping the InGaAs stripes. Without free charge carriers in the stripes (Fig. 6.14**a**), we observe the lower polariton resonances of the LC and DP cavity mode, as well as their corresponding upper polariton fans. Upon introducing free carriers into the stripes with a doping density of $\rho_{\text{switch}} = 3.5 \times 10^{18}\,\text{cm}^{-3}$ (Fig. 6.14**b**), both the LP mode and the entire UP fan of the LC mode are absent. This signifies a complete breakdown of the coupling of the

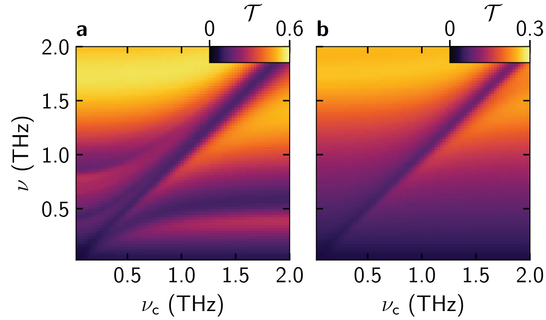

Figure 6.14 | Simulated switching of a structure with a single QW coupled to the maximally compacted resonator. **a**, Calculated THz transmission of the sample, as a function of ν_c. **b**, THz transmission after excitation of the switching patch.

LC mode. Meanwhile, the LP and the multiple UP modes of the dipolar cavity mode exhibit an upward shift in frequency and a reduction in intensity. This outcome aligns with our expectations, considering that simulating the unmodified resonator reveals an elevated frequency for the bare dipolar mode alongside diminished intensity.

These results demonstrate the capability of the improved switching concept to fully switch off coupled structures featuring the maximally compact butterfly resonator design, while not hindering potential photon emission from the region with the strongest LC mode field enhancement.

Conclusion

Our switching design for deep-strong light-matter coupling adds time as a new control parameter for cavity-QED, allowing us to switch off the coupling at a speed more than ten times faster than the oscillation cycle of the lower polariton mode. This rapid subcycle process is evidenced by oscillations in the optical response function, which our newly developed quantum theory links to a novel coherent energy transfer mechanism through which the switching pulse liberates energy trapped in the coupling mechanism.

Combining the mechanism with the maximally compact butterfly resonator structures, featuring over one whole virtual photon per resonator array, the switch-off is expected to release the population of the vacuum ground state, analogous to the concept of Unruh-Hawking radiation observed in black holes [Haw74, Haw75, Unr76, Lib07, Gü09, Gar13]. Since the resonator array can be easily fabricated to a size of 0.5 cm by 0.5 cm, we can expect to see on the order of 25,000 emitted photons per switching event. Using a laser system with a repetition rate of 1 MHz, this corresponds to $2.5 \cdot 10^{10}$ expected photons per second. Furthermore, the non-adiabatic control possibilities provide a platform to explore non-adiabatic quantum optics, ultrafast vacuum-modified transport [Org15, Bar18, PB19, Val21, App22] or chemistry [Hut12, Chi16, Her16, Tho19, Dun22, Sch22] and cavity-mediated phase transitions, including superconductivity [Sch19], on demand, without the requirement of THz illumination or direct excitation of matter.

Chapter 7

Conclusion

The fact that the vacuum is not empty, but rather populated by omnipresent fluctuations, has redefined our physical understanding of the world and sprouted a multitude of exciting new fields of physics [Mil13].

Light-matter coupling allows us to harness these powerful vacuum fluctuations, shape them and utilize them to tailor quantum systems. In this thesis, multiple new regimes of ultrastrong and deep-strong light-matter coupling have been pioneered, allowing for record coupling strengths and unprecedented control of the extreme interaction of light and matter on the nanoscale and subcycle timescales [Hal20, Mor21, Cor23, Mor23a, Mor23b]. These pioneering steps could ultimately pave the way towards the detection of radiation arising directly from the quantum vacuum fluctuations themselves. Here, these accomplishments have been facilitated by the highly tunable and capable platform of the coupling between the cyclotron resonances of a two-dimensional electron gas hosted in QWs and subwavelength-confined THz modes of planar plasmonic resonator structures.

First, we entered a new regime at the interface of strong-field physics and vacuum photonics, where the vacuum Rabi frequency, $\Omega_{\mathrm{R}}^{\mathrm{vac}}$, the Rabi frequency of the external coherent driving field, $\Omega_{\mathrm{R}}^{\mathrm{coh}}$, and the carrier frequency of light, ω_0, all become comparable. In this nonperturbative setting, subcycle nonlinearities up to eight-wave mixing occur, revealing mixing between the orthogonal polariton eigenstates of the system and creating new nonlinearities inaccessible by linear spectroscopy. This opens up a path to tailoring novel quantum states and nonlinearities to enhance ground-state instabilities and drive phase transitions. Such nonlinear optical control may even facilitate novel quantum devices harnessing parametric nonlinearities for coherent light sources or squeezed quantum states of light [Rid13].

Next, by lateral confinement of the quantum wells, we open up a previously unexplored parameter space for tailoring ultrastrong light-matter coupling. Generally, light-matter interaction is fundamentally governed by the spatial overlap of the vacuum electric field of the resonator mode and the polarization field of the matter excitation. So far, most investigations focused purely on maximising the overlap to achieve the maximum coupling strength. Yet, the large design space accessible by subwavelength control of the shape and overlap of modes is often not fully taken advantage of. Spatial structuring of the quantum wells allows us to manipulate the coupling as well as overlap between multiple matter and cavity modes, similar to tailoring of selection rules in classical optics. Here, our changes in the overlap, on the order of 85%, are demonstrated to have a significant impact on the characteristics of the polariton modes, affecting polariton frequencies, magnetic field dependence, and spatial field distribution. Control of these parameters and the mutual couplings between modes as well as their dispersion, is highly relevant for nanophotonic applications, especially in multi-mode settings, where the suppression or enhancement of individual interactions opens up new possibilities.

Leveraging the concept of multi-mode coupling further facilitated reaching new record coupling strengths. Here, a newly designed, maximally compact resonator metasurface that custom-tailors multiple plasmon resonances as well as optical modes allows us to exploit the cooperative dipole moments of multiple, highly non-resonant magnetoplasmon modes. The novel multi-mode coupling results in an ultrabroadband spectrum of Landau magneto-cavity polaritons, spanning a bandwidth of as much as 6 optical octaves. This extreme interaction features a vacuum ground state hosting a record population of 1.17 virtual photons and 1.06 virtual magnetoplasmon excitations, equivalent to an effective light-matter coupling strength of $\Omega_{\mathrm{R}}^{\mathrm{s}}/\omega_{\mathrm{s}} = 3.19$ – almost twice as much as all previously achieved records [Bay17, Mue20]. The almost threefold boost of the number of virtual excitations per resonator and the increase in resonator density will especially benefit the envisioned detection of vacuum radiation [Lib07, Gü09, Gar13, Hal20]. This extreme limit of light-matter interaction, combined with multi-mode coupling, even facilitates the hybridization of otherwise non-interacting bosonic matter modes, purely through the vacuum field of the common cavity mode. This principle can be applied to interactions between a variety of systems such as magnons, phonons or Dirac electrons, including the mixing of entirely different excitations, offering exciting possibilities with novel mixed states of matter.

An equally important breakthrough for the detection of vacuum radiation is the development of a strongly non-adiabatic switch-off mechanism for deep-strong coupling. Here, selective photodoping of a tailored, local switching element collapses the cavity field quasi-instantaneously and decouples light and matter. This rapid quench of the vacuum ground state is accompanied by strong polarisation oscillations, confirming the quasi-instantaneous nature of the switch-off on timescales ten times faster than a cycle of light. These subcycle dynamics originate in the periodic energy transfer between the systems and the coupling, offering the potential for energy transfer out of the coupling mechanism and the release of the virtual photon population from the deep-strongly coupled vacuum ground state. This quasi-instantaneous control of deep-strong light-matter coupling serves as an ideal platform for exploring more non-adiabatic effects in cavity-QED or designing all-optically controlled filters and modulators with tailor-made response functions.

Perspectives

The new subcycle control strategies and the exploration of new domains of light-matter coupling introduce fundamentally fresh avenues for sculpting the interaction between light and matter. Particularly compelling is the prospect of merging the nanoscale and subcycle temporal control schemes with the achieved record-breaking levels of coupling strength, as this synergy could uncover even more intriguing effects of cavity-QED. One particularly exciting prospect for cavity-QED is the detection of Unruh-Hawking-like radiation arising from the squeezed quantum vacuum. Here, the remarkable records achieved for coupling strength and vacuum photon population, combined with the developed quasi-instantaneous switch-off mechanism, pave the way for the detection of vacuum photon emission from these samples. This measurement would constitute the most direct validation of the presence of vacuum fluctuations to date. To bring this concept to fruition, we already refined the switching mechanism for the maximally compact resonator array and optimized photon emission. Further we developed an experimental setup with maximized collection efficiency of vacuum photons, enhancements in thermal radiation management and employing highly sensitive, single-shot electro-optic correlation spectroscopy [BC19].

Looking ahead, the presented capabilities are not limited to the coupling of the cyclotron resonance to planar cavities, but can be universally employed for a wide variety of coupled systems, such as e.g. intersubband polaritons, where precise control of the coupling is vital for achieving inversionless lasing. Here, stimulated coherent polariton-polariton scattering of intersubband polaritons in dispersive cavities is the first prerequisite to reach this goal. This significant accomplishment is depicted in [Kno22]. While not extensively covered in this thesis, it underlines the significance of understanding and recording ultrafast dynamics. Doing so allows for further optimizations of the coupled system on the nanoscale and subcycle timescales, which is expected to enable gain, condensation, and the realization of inversionless lasing of the polaritons.

Moreover, the novel techniques outlined in this study can be applied to e.g. vibrational modes of molecules, lattice vibrations of Josephson plasmons or Dirac electrons, or even can be used to mix entirely different excitations. These opportunities bring exciting prospects to quantum computing, where the ability to tailor light-matter coupling within quantum systems with both ultrafast temporal and subwavelength precision could further accelerate and simplify quantum information processing [FK19, FD19]. In addition, dynamic control with subwavelength precision of the coupling could be used to trigger chemical reactions without the need for a photocatalyst [Hut12, Chi16, Her16, Tho19, Dun22, Sch22], manipulate vacuum-modified transport [Org15, Bar18, PB19, Val21, App22] and cavity-mediated phase transitions, including superconductivity [Sch19], on demand, without the requirement of THz illumination or direct excitation of matter.

Ultimately, all of these exciting prospects share one common feature - they are made possible merely by shaping the quantum vacuum.

Appendix A

Sample structure preparation

The gold resonator structures are processed onto the bare QW or GaAs samples with electron-beam lithography (EBL) and subsequent wet-chemical processing. In a first step, a layer of positive electron beam resist (CSAR 6200.13) is applied to the surface of the sample. Subsequently the desired geometry is structured on the sample surface using EBL. Here the parts of the sample which should be covered in gold are exposed to the electron beam in 2x2 mm arrays with an area dose of 60 µCcm^{-2}. The exposed areas are removed by developing the sample for 80 s in AR600 546. Subsequent thermal deposition of 10 nm of Ti aids with the adhesion of the subsequently deposited gold layer of a thickness of 100 nm. The remaining resist and surplus gold are removed using Remover PG.

Additionally, for the switchable samples extra fabrications steps need to take place. To fabricate the patches, the QW stacks are capped by an $In_{0.55}Ga_{0.45}As$ layer with a thickness of 100 nm. The InGaAs layer features an energy gap of 0.73 eV and is grown with an intentionally defect-rich crystal structure which still shows photoconductivity but does not allow for a cyclotron resonance to form. The switching patches are also structured by electron-beam lithography and wet-chemical etching. Here a negative resist (ARN 7500.18) is exposed with a dose of 110 µCcm^{-2}. Etching of the InGaAs is performed in citric acid for 60 s. To eliminate two-photon absorption of the switching pulse in the substrate, the sample is glued to a sapphire substrate with a thickness of 500 µm, which allows for the removal of the GaAs substrate.

Appendix **B**

Sample structure overview

name	**resonator**	**n_{QW}**	ρ
S1	double gap	1	$6.3 \times 10^{11}\,\mathrm{cm}^{-2}$
S6	double gap	6	$1.75 \times 10^{12}\,\mathrm{cm}^{-2}$
S3unstr	double gap	3	$1.0 \times 10^{12}\,\mathrm{cm}^{-2}$
S3str	double gap	3	$1.0 \times 10^{12}\,\mathrm{cm}^{-2}$
S3pat	-	3	$1.0 \times 10^{12}\,\mathrm{cm}^{-2}$
Str6	-	6	$1.15 \times 10^{12}\,\mathrm{cm}^{-2}$
BF1	butterfly	1	$1.28 \times 10^{12}\,\mathrm{cm}^{-2}$
BF3	butterfly	3	$7.90 \times 10^{11}\,\mathrm{cm}^{-2}$
BF6	butterfly	6	$1.37 \times 10^{12}\,\mathrm{cm}^{-2}$
BF12	butterfly	12	$1.90 \times 10^{12}\,\mathrm{cm}^{-2}$
BF24	butterfly	24	$2.30 \times 10^{12}\,\mathrm{cm}^{-2}$
BF48	butterfly	48	$1.80 \times 10^{12}\,\mathrm{cm}^{-2}$
S3sw	double gap	3	$1.75 \times 10^{12}\,\mathrm{cm}^{-2}$
L6	L-gap	6	$1.75 \times 10^{12}\,\mathrm{cm}^{-2}$

Table B.1: Parameters for all structures featuring QWs.

Appendix C

Finite-element frequency-domain simulations

In order to design and validate our sample structures, as well as get a deeper insight into the microscopic functionality of the resonators and coupled systems, we employ finite-element frequency-domain (FEFD) simulations using COMSOL Multiphysics. Following the implementation of [Bay17], we solve Maxwell's equations classically. This gives us a parameter free theory, which cannot only predict the behaviour of the bare resonator structures, but also the response of coupled structures, even in the DSC regime. This is possible, as both, light and matter, are treated together and thus the reshaping of the cavity modes by the matter system is considered adequately.

Here we define a simulation volume, which contains the desired three-dimensional geometry of the nanostructures with their individual dielectric response (Fig. C.1**a**). After discretization to a mesh (Fig. C.1**b**), the program solves Maxwell's equations on this mesh for a fixed frequency. The calculation yields the 3D response of the structures including the spatially resolved near-field distribution as well as the far-field transmission, without any free fit parameters.

For implementing the structures, we follow [Bay17] and choose a dielectric constant of $\epsilon_{\mathrm{Au}} = 10^5 + 10^5 i$ for the gold metamaterial. The magnetically invariant GaAs

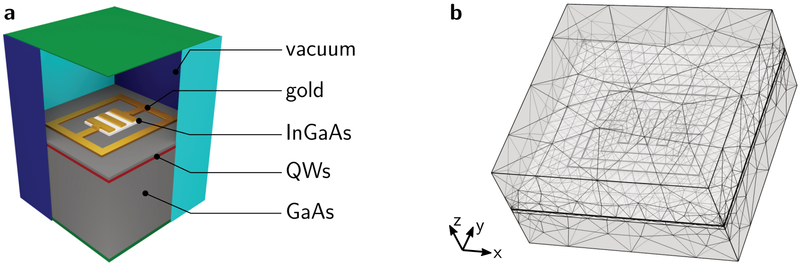

Figure C.1 | Finite-element frequency-domain simulations. a, Schematic overview of the simulation volume including all different implemented materials. **b**, Example of a mesh used to solve Maxwell's equation on.

substrate layers are implemented by the dielectric function

$$\epsilon_{\mathrm{GaAs}}(\omega) = \epsilon_{\infty} \frac{\omega_{\mathrm{LO}}^2 - \omega^2 + i\gamma_{\mathrm{LO}}\omega}{\omega_{\mathrm{TO}}^2 - \omega^2 + i\gamma_{\mathrm{TO}}\omega}, \tag{C.1}$$

where we include the optical phonons of GaAs to improve the accuracy of the calculation for higher THz frequencies and use $\epsilon_{\infty} = 10.87$ [Loc05], $\omega_{\mathrm{LO}}/2\pi = 8.839\,\mathrm{THz}$, $\omega_{\mathrm{TO}}/2\pi = 8.124\,\mathrm{THz}$, $\gamma_{\mathrm{LO}} = 0.0225\,\mathrm{THz}$ and $\gamma_{\mathrm{TO}} = 0.0255\,\mathrm{THz}$ [Irm96]. The QWs feature an anisotropic dielectric response, which is implemented as a tensor function $\underline{\epsilon}(\mathbf{r}, \omega_c, \omega)$, which depends on the direction $\mathbf{r}$, the cyclotron frequency, ω_{c}, and the frequency of the THz field, ω.

$$\underline{\epsilon} = \begin{pmatrix} \epsilon_{xx} & i\epsilon_{xy} & 0 \\ -i\epsilon_{xy} & \epsilon_{xx} & 0 \\ 0 & 0 & \epsilon_{\mathrm{GaAs}} \end{pmatrix}. \tag{C.2}$$

Here, the components $\epsilon_{xx} = \epsilon_{\mathrm{GaAs}} - \frac{\omega_{\mathrm{p}}^2(\omega + i\kappa)}{\omega[(\omega+i\kappa)^2 - \omega_{\mathrm{c}}^2]}$ and $\epsilon_{xy} = \frac{\omega_{\mathrm{p}}^2 \omega_{\mathrm{c}}}{\omega[(\omega+i\kappa)^2 - \omega_{\mathrm{c}}^2]}$ with $\omega_{\mathrm{p}} = \sqrt{\frac{\rho e^2}{\epsilon_0 m^*}}$ describe the gyrotropic nature of two-dimensional polarization response of the cyclotron resonance in x- and y-direction. In z-direction, we employ the background dielectric constant of GaAs, since the small thickness of the QW inhibits a plasma response in our frequency regime. The scattering rate of $\kappa = 0.3\,\mathrm{THz}$ is set to match the experimentally observed typical cyclotron line width. Additionally, to reduce the numerical complexity of modelling several quantum wells and the corresponding barriers between them, we employ an effective medium for the complete quantum well stack with an effective dielectric tensor.

We account for the array character of our structure by implementing a single unit cell and using periodic boundary conditions in x- and y-directions. The resulting far-field calculations are calculated with an algorithm developed by Stratton and Chu [Str39] and predict experimental results across the entire spectral range with high accuracy.

Switching patches

To include the effect of the switching patches into the simulations and guide the design of the switching concept itself, we use the Drude model with different charge carrier densities for the unswitched and switched state to account for the photoexcitation. The (3D) plasma frequency is given by

$$\omega_{\mathrm{p}} = \sqrt{\frac{\rho_{\mathrm{switch}} e^2}{\epsilon_0 m_{\mathrm{InGaAs}}}}. \tag{C.3}$$

Here, $m_{\mathrm{InGaAs}} = 0.04\, m_{\mathrm{e}}$ denotes the effective mass of conduction band electrons in InGaAs, m_{e} is the free electron mass, ρ_{switch} is the electron charge carrier density, ϵ_0 is the vacuum permittivity, and e is the elementary charge. In the experiment, we achieve saturation of the switching effect. Therefore we assume a density of photoexcited carriers of $\rho_{\mathrm{switch}} = 3.5 \times 10^{18}\,\mathrm{cm}^{-3}$, corresponding to the total density of states of InGaAs within the bandwidth of our switching pulse. As a result, we obtain a plasma frequency of $\nu_{\mathrm{p}} = \omega_{\mathrm{p}}/2\pi = 80\,\mathrm{THz}$. The dielectric function of the plasma is then given by

$$\epsilon_{\mathrm{InGaAs}}(\omega) = \epsilon_{\mathrm{InGaAs}}(\infty) - \frac{\omega_{\mathrm{p}}^2 \tau_{\mathrm{s}}^2}{\omega^2 \tau_{\mathrm{s}}^2 + i\omega\tau_{\mathrm{s}}}, \tag{C.4}$$

with a scattering time of $\tau_{\mathrm{s}} = 1 \times 10^{-13}\,\mathrm{s}$, and $\epsilon_{\mathrm{InGaAs}}(\infty) = 13.7$.

Appendix D

Time-domain simulations of the compact resonator array

Frequency response of the maximally compact resonator structure

In order to accurately simulate the coupled spectra of the samples with the maximally compact resonator structure, we first need to identify the individual modes of the bare resonator structure. Then we derive again the equations of motion for each operator using Heisenberg's equation of motion.

We characterize the complex frequency response of the metasurface by a superposition of cavity fields, denoted as α_j. Each cavity field α_j is associated with a specific custom frequency ν_j and contributes with a relative amplitude A_j, phase ϕ_j, and damping rate γ_j carefully chosen to optimize the representation of the far-field response obtained from our finite-element frequency-domain calculations. By implementing a total of five oscillators with the parameters provided in Table D.1, we successfully reproduce the finite-element frequency-domain results, as demonstrated in Figure D.1**a**. The frequency response of each individual oscillator is displayed in Figure D.1**b**.

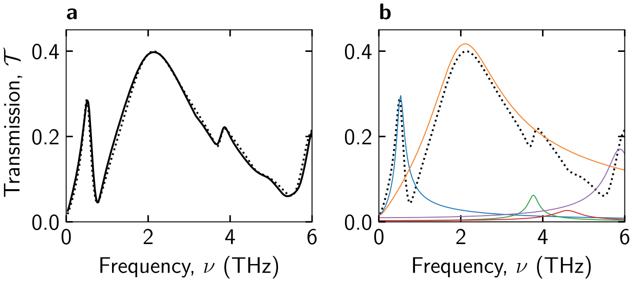

Figure D.1 | Far-field transmission of the bare metasurface, **a**, calculated by the finite-element frequency-domain method (solid curve) and transmission obtained from the harmonic oscillator representation of our time-domain simulations (dotted curve). **b**, with the simulation of each individual oscillator (coloured curves) Adapted from [Mor23a].

Mode index j	ν_j **(THz)**	γ_j **(THz)**	A_j	ϕ_j
1	0.52	0.08	2.8	0
2	1.95	0.80	44.5	-0.14 π
3	3.75	0.12	0.8	-0.25 π
4	4.60	0.30	0.9	-0.60 π
5	6.00	0.30	7.0	-0.14 π

Table D.1: Parameters for the cavity modes used to model the frequency response of the butterfly resonator structure. Adapted from [Mor23a]

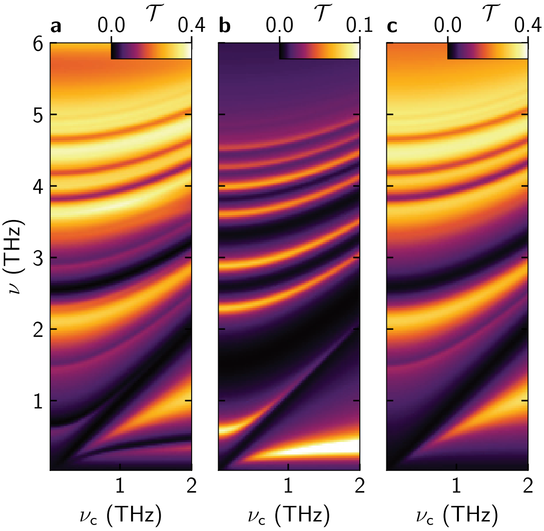

Figure D.2 | Switch-off analysis for the optical modes for the 48-QW structure. Time-domain simulation including **a**, all modes, **b**, only the first and **c**, only the second optical mode of the resonator structure. Adapted from [Mor23a].

Mode selective simulations of the 48 QW sample

Using our time-domain quantum model, we investigate the individual contributions of each optical mode to the transmission spectrum of the structure. This is achieved through a switch-off analysis, where we selectively disable specific modes and observe the resulting impact on the far-field response. In particular, we focus on the contributions of the two most significant cavity modes, $j = 1$ and $j = 2$, and plot them separately in Figure D.2. This allows us to distinguish the magnetoplasmon polaritons of both cavity modes and to obtain a highly accurate fit to the experimental data.

Appendix E

Ultrastrong coupling of the cyclotron transition in the general multimode case

The following theory describes in detail the general case of coupling the cyclotron resonance of a 2DEG to multiple modes of a planar metasurface resonator in more detail than in chapter 2.1 and chapter 4. The theory was developed by Erika Cortese and Simone De Liberato and is also published in again a shorter form in [Cor23].

E.1. Light-matter Hamiltonian in Coulomb gauge

Let us consider the Hamiltonian describing a two-dimensional electron gas (2DEG) of N electrons of charge $-e$ and effective mass m^* interacting with a resonator photonic field in the Coulomb gauge

$$\hat{H} = \int d\mathbf{r} \left[\frac{\epsilon_0 \hat{\mathbf{E}}_\perp(\mathbf{r})^2}{2} + \frac{\hat{\mathbf{B}}(\mathbf{r})^2}{2\mu_0} \right] + \sum_{l=1}^{N} \frac{\left(\hat{\mathbf{p}}_l + e\hat{\mathbf{A}}\left(\mathbf{r}_l\right)\right)^2}{2m^*} + V(\mathbf{r}), \tag{E.1}$$

expressed in terms of the electric and magnetic field vectors $\hat{\mathbf{E}}(\mathbf{r})$ and $\hat{\mathbf{B}}(\mathbf{r})$, the potential vector $\hat{\mathbf{A}}(\mathbf{r})$ and the Coulomb potential $V(\mathbf{r})$.
The first term represents the energy of the transverse fields $\hat{\mathbf{B}}(\mathbf{r})$ and $\hat{\mathbf{E}}_\perp(\mathbf{r}) = -\frac{\hat{\mathbf{\Pi}}(\mathbf{r})}{\epsilon_0}$, where $\hat{\mathbf{\Pi}}(\mathbf{r})$ is the conjugate momentum of the vector potential, which satisfies the commutation relation $\left[\hat{\mathbf{A}}(\mathbf{r}), \hat{\mathbf{\Pi}}\left(\mathbf{r}'\right)\right] = \hbar\delta^T\left(\mathbf{r} - \mathbf{r}'\right)$.

We now consider the following approximations: first, we neglect the degrees of freedom of charges in the dielectric background, although considering their effect by substituting the vacuum dielectric permittivity ϵ_0 with the one of medium $\epsilon_0\epsilon(\mathbf{r})$, taken isotropic and non dispersive; then, thanks to Kohn's theorem [Koh61], we can neglect the Coulomb electron-electron interactions, since it has been demonstrated that they have no effect on the cyclotron resonance we are investigating (for low excitation fields) [Maa16]. (Here we would also already deviate for introducing the (magneto-)plasmons discussed in chapter 5.)

If, for sake of simplicity, we consider a z-dependent background dielectric permittivity, for the electromagnetic field Hamiltonian we obtain

$$\hat{H}_{\mathrm{EM}} = \int d\mathbf{r} \left[\frac{\epsilon_0\epsilon(z)\hat{\mathbf{E}}_\perp(\mathbf{r})^2}{2} + \frac{\hat{\mathbf{B}}(\mathbf{r})^2}{2\mu_0} \right] . \tag{E.2}$$

By expressing the fields in terms of the potential vector $\hat{\mathbf{A}}(\mathbf{r})$, such that

$$\hat{\mathbf{B}}(\mathbf{r}) = \nabla \times \hat{\mathbf{A}}(\mathbf{r}), \tag{E.3}$$

$$\hat{\mathbf{E}}_\perp(\mathbf{r}) = -\frac{\partial}{\partial t}\hat{\mathbf{A}}(\mathbf{r}), \tag{E.4}$$

we can express the electromagnetic Hamiltonian as

$$\hat{H}_{\mathrm{EM}} = \int d\mathbf{r} \left[\frac{\epsilon_0\epsilon(z)}{2} \left(\frac{\partial}{\partial t}\hat{\mathbf{A}}(\mathbf{r}) \right)^2 + \frac{(\nabla \times \hat{\mathbf{A}}(\mathbf{r}))^2}{2\mu_0} \right] . \tag{E.5}$$

By quantizing the electromagnetic field, we obtain the vector potential operator

$$\hat{\mathbf{A}}(\mathbf{r}) = \sum_j \mathcal{C}_j \left[\mathbf{f}_j^*(\mathbf{r})\hat{a}_j^\dagger + \mathbf{f}_j(\mathbf{r})\hat{a}_j \right] , \tag{E.6}$$

where the index j counts the electromagnetic modes, $\mathbf{f}_j(\mathbf{r})$ is the spatial mode shape function vector and $\mathcal{C}_j$ is a normalization factor

$$\mathcal{C}_j = (\hbar/2\epsilon_0\epsilon(z)\omega_j\mathbb{V}_j)^{\frac{1}{2}} , \tag{E.7}$$

with the mode effective volume

$$\mathbb{V}_j = \int d\mathbf{r}\, |\mathbf{f}_j(\mathbf{r})|^2 , \tag{E.8}$$

such that, calculated the fields from the vector potential (E.6) and plugged in (E.2), this is equal to

$$\hat{H}_{\rm EM} = \sum_j \hbar\omega_j \left(\hat{a}_j^\dagger \hat{a}_j + \frac{1}{2} \right) . \tag{E.9}$$

Let us focus now on the light-matter interaction. We consider a number $N_{\rm QW}$ of 2DEGs in which the electrons are distributed and free to move on the xy-plane at $z = z_{{\rm 2DEG},n}$ and that a static magnetic field $\mathbf{B_s}$ is applied along the z-direction. For simplicity, we assume that the electromagnetic field distribution along z varies slowly enough to be considered homogeneous within the stack of $N_{\rm QW}$ 2DEGs, and as such we assume that light couples equally to all of them. We can write the total Hamiltonian as

$$\hat{H} \approx \hat{H}_{\rm EM} + \sum_{l=1}^{N} \frac{\left(\hat{\pi}_l + e\hat{\mathbf{A}}\left(\mathbf{r}_{\parallel,l}\right)\right)^2}{2m^*}, \tag{E.10}$$

where $N = N_{\rm QW} \cdot \rho S$ is the total number of electrons on the $N_{\rm QW}$ surfaces S with superficial electron density $\rho, \mathbf{r}_{\parallel,l}$ is the electron coordinate on the plane $x - y$, and $\hat{\pi}_l = \hat{\mathbf{p}}_l + e\hat{\mathbf{A}}_0$ is the in-plane momentum coupling with the static vector potential A_0, such that $\mathbf{B_s} = \nabla \times \mathbf{A_0}$.

Let us introduce the bosonic lowering operator between the Landau levels with cyclotron transition frequency $\omega_{\rm c}$

$$\hat{c}_l = \frac{\hat{\pi}_{y,l} + i\hat{\pi}_{x,l}}{\sqrt{2m^*\hbar\omega_{\rm c}}}, \tag{E.11}$$

satisfying $\left[\hat{c}_l, \hat{c}_l^\dagger\right] = 1$. Then the total Hamiltonian can be rewritten as

$$\begin{aligned}
\hat{H} &= \hat{H}_{\mathrm{EM}} + \sum_{l=1}^{N} \frac{\hat{\pi}_l^2}{2m^*} + \sum_{l=1}^{N} \left[\frac{e}{m^*}\hat{\pi}_l \cdot \hat{\mathbf{A}}\left(\mathbf{r}_{\|,l}\right) + \frac{e^2}{m^*}\hat{\mathbf{A}}\left(\mathbf{r}_{\|,l}\right)^2\right] = \qquad \text{(E.12)}\\
&= \hat{H}_{\mathrm{EM}} + \sum_{l=1}^{N} \frac{\hat{\pi}_l^2}{2m^*}\\
&+ \sum_{l=1}^{N} \left[\frac{e}{m^*}\left(\hat{\pi}_{-,l}\hat{A}_+\left(\mathbf{r}_{\|,l}\right) + \hat{\pi}_{+,l}\hat{A}_-\left(\mathbf{r}_{\|,l}\right)\right) + \frac{e^2}{m^*}\hat{A}_-\left(\mathbf{r}_{\|,l}\right)\hat{A}_+\left(\mathbf{r}_{\|,l}\right)\right] = \qquad \text{(E.13)}\\
&= \hat{H}_{\mathrm{EM}} + \sum_l \hbar\omega_{\mathrm{c}}\left(\hat{c}_l^\dagger\hat{c}_l + \frac{1}{2}\right)\\
&+ \sum_l \left[\sqrt{\frac{\hbar\omega_{\mathrm{c}}e^2}{m^*}}\left(\hat{c}_l^\dagger\hat{A}_+\left(\mathbf{r}_{\|,l}\right) + \hat{c}_l\hat{A}_-\left(\mathbf{r}_{\|,l}\right)\right) + \frac{e^2}{m^*}\hat{A}_-\left(\mathbf{r}_{\|,l}\right)\hat{A}_+\left(\mathbf{r}_{\|,l}\right)\right], \qquad \text{(E.14)}
\end{aligned}$$

with $\hat{\pi}_{\pm,l} = \left(\hat{\pi}_{x,l} \mp i\hat{\pi}_{y,l}\right)/\sqrt{2}$, which means $\hat{c}_l = \hat{\pi}_{+,l}/\sqrt{m^*\hbar\omega_{\mathrm{c}}}$, and

$$\hat{A}_\pm\left(\mathbf{r}_{\|,l}\right) = \frac{\hat{A}_x\left(\mathbf{r}_{\|,l}\right) \mp i\hat{A}_y\left(\mathbf{r}_{\|,l}\right)}{\sqrt{2}}. \qquad \text{(E.15)}$$

Since we defined the vector potential as in Eq. (E.6), we can express the two components $\hat{A}_\pm\left(\mathbf{r}_{\|,l}\right)$ as

$$\hat{A}_\pm\left(\mathbf{r}_{\|,l}\right) = \sum_j \mathcal{C}_j\left(f_{j,\mp}^*\left(\mathbf{r}_{\|,l}\right)\hat{a}_j^\dagger + f_{j,\pm}\left(\mathbf{r}_{\|,l}\right)\hat{a}_j\right) \qquad \text{(E.16)}$$

with $f_{\pm,j} = \left(f_{x,j} \mp i f_{y,j}\right)/\sqrt{2}$. Since we assume real the x and y components of the field, we find $f_{\mp,j}^* = f_{\pm,j}$, so the vector potential can thus be written as

$$\hat{A}_\pm\left(\mathbf{r}_{\|,l}\right) = \sum_j \mathcal{C}_j f_{\pm,j}\left(\mathbf{r}_{\|,l}\right)\left(\hat{a}_j^\dagger + \hat{a}_j\right). \qquad \text{(E.17)}$$

Therefore, if we recall $f_j = f_{j,-}$ we can write the total Hamiltonian, as

$$\begin{aligned}\hat{H} = \hat{H}_{\mathrm{EM}} &+ \sum_l \hbar\omega_{\mathrm{c}} \left(\hat{c}_l^\dagger \hat{c}_l + \frac{1}{2}\right) \\ &+ \sqrt{\frac{\hbar\omega_{\mathrm{c}} e^2}{m^*}} \sum_l \sum_j \mathcal{C}_j \left[f_j \left(\mathbf{r}_{\parallel,l}\right) \hat{c}_l \left(\hat{a}_j^\dagger + \hat{a}_j\right) + \text{ h.c. } \right] \\ &+ \frac{e^2}{m^*} \sum_l \sum_j \sum_{j'} \mathcal{C}_j \mathcal{C}_{j'} f_j \left(\mathbf{r}_{\parallel,l}\right) f_{j'}^* \left(\mathbf{r}_{\parallel,l}\right) \left(\hat{a}_j^\dagger + \hat{a}_j\right) \left(\hat{a}_{j'}^\dagger + \hat{a}_{j'}\right). \qquad \text{(E.18)}\end{aligned}$$

E.2. General case of non-orthogonality and photons mode overlap effects

Let us focus the attention only on the third term of the Hamiltonian in Eq. (E.18), describing the interaction between the photonic modes and the cyclotron motion of the electron,

$$\hat{H}_{\mathrm{int}} = \sqrt{\frac{\hbar\omega_{\mathrm{c}} e^2}{m^*}} \sum_l \sum_j \mathcal{C}_j \left[f_j \left(\mathbf{r}_{\parallel,l}\right) \hat{c}_l \left(\hat{a}_j^\dagger + \hat{a}_j\right) + \text{ h.c. } \right]. \qquad \text{(E.19)}$$

Although we assume the orthogonality for the resonator field modes over the whole volume $V = L \times S_T$, with L and S_T are the total length and surface, if we restrict our self on the xy-plane of the 2DEGs, in principle, the photon modes cannot be orthogonal, and as such they could mix up when they couple to the collective matter modes. This aspect is the novel key point of our theory.

Let us consider the first n photonic modes, whose shape functions $f_j\left(\mathbf{r}_\parallel\right)$ can be defined in terms of a set of n mode functions ϕ_j defined orthogonal over the plane occupied by the 2DEG of area S, as

$$f_j\left(\mathbf{r}_{l,\parallel}\right) = \sum_{\mu\leq j} \alpha_{j,\mu} \phi_\mu \left(\mathbf{r}_{l,\parallel}\right) \qquad \text{(E.20)}$$

obeying the normalisation relations

$$\int_S \phi_j^* \left(\mathbf{r}_\parallel\right) \phi_\mu \left(\mathbf{r}_\parallel\right) \mathrm{d}\mathbf{r}_\parallel = \delta_{\mu,j} \qquad \text{(E.21)}$$

and

$$\sum_{l}^{N_{el}} \phi_j^* \left(\mathbf{r}_{l,\parallel}\right) \phi_\mu \left(\mathbf{r}_{l,\parallel}\right) = \rho \delta_{\mu,j}, \tag{E.22}$$

where $N_{el} = \rho S$ is the number of electrons for each 2DEG. Since the mode function has to be normalised over all the volume, whereas the function $\phi_\mu \left(\mathbf{r}_{l,\parallel}\right)$ is normalised only upon the surface S where the electrons are distributed, let us notice that the coefficient $\alpha_{j,j}$ must scale as the total area $\sqrt{S_T}$.

Let us define now a set of n collective matter modes as

$$\hat{b}_\alpha = \frac{1}{\sqrt{\rho}} \sum_{l}^{N} \phi_\alpha \left(\mathbf{r}_{l,\parallel}\right) \hat{c}_l. \tag{E.23}$$

As it is explained above, even though the two photon modes are orthogonal when integrated over all the cavity volume, this is not true if we consider the plane in which they couple to the electronic transitions. We define then a normalization factor matrix element

$$\mathcal{F}_{\alpha,j} = \sum_{l=1}^{N} f_\alpha^* \left(\mathbf{r}_{l,\parallel}\right) f_j \left(\mathbf{r}_{l,\parallel}\right), \tag{E.24}$$

which is, in general, different from zero. We can easily derive that the in-plane normalization factor for the first mode $\mathcal{F}_1 = \sum_l^N \left|f_1 \left(\mathbf{r}_{l,\parallel}\right)\right|^2 = N_{\mathrm{QW}} \rho \left|\alpha_{1,1}\right|^2$

It is clear that, if the photon modes are orthogonal over the plane, no overlap between them occurs and the matrix F of elements $\mathcal{F}_{\alpha,j}$ is diagonal.

In order to obtain the coefficients $\alpha_{\alpha,j}$, from the orthonormalization rules, we can write the relation

$$\mathcal{F}_{j,\alpha} = N_{\mathrm{QW}} \rho \sum_{\gamma \leq \min(j,\alpha)} \alpha_{j,\gamma}^* \alpha_{\alpha,\gamma}. \tag{E.25}$$

Since $\mathcal{C}_j = \left(\hbar / 2\epsilon_0 \bar{\epsilon} \omega_j \mathbb{V}_j\right)^{\frac{1}{2}}$ with $\bar{\epsilon} = \epsilon \left(z_{\mathrm{DEG},n}\right)$ is constant for all the 2DEGs, it is possible now to rewrite the interaction Hamiltonian as

$$\hat{H}_{\text{int}} = \sum_j \sqrt{\frac{\hbar^2 \omega_{\text{c}} N_{\text{QW}} \rho e^2}{2m^* \epsilon_0 \bar{\epsilon} \omega_j \mathbb{V}_j}} \sum_{\alpha \leq j} \left[\alpha_{j,\alpha} b_\alpha \left(\hat{a}_j^\dagger + \hat{a}_j \right) + \text{ h.c. } \right]. \tag{E.26}$$

The total Hamiltonian for the light-matter system becomes then

$$\hat{H} = \hat{H}_{\text{EM}} + \hat{H}_{\text{matter }} + \hat{H}_{\text{int}} + \hat{H}_{\text{dia}} \tag{E.27}$$

with

$$\hat{H}_{\text{EM}} = \sum_j \hbar \omega_j \left(\hat{a}_j^\dagger \hat{a}_j + \frac{1}{2} \right), \tag{E.28}$$

$$\hat{H}_{\text{matter }} = \sum_\alpha \hbar \omega_{\text{c}} \left(\hat{b}_\alpha^\dagger \hat{b}_\alpha + \frac{1}{2} \right), \tag{E.29}$$

$$\hat{H}_{\text{int}} = \sum_j \sum_{\alpha \leq j} \left[\left(g_{j,\alpha} b_\alpha + g_{j,\alpha}^* b_\alpha^\dagger \right) \left(\hat{a}_j^\dagger + \hat{a}_j \right) \right], \tag{E.30}$$

$$\hat{H}_{\text{dia}} = \sum_j \sum_{j'} h_{j,j'} \left(\hat{a}_j^\dagger + \hat{a}_j \right) \left(\hat{a}_{j'}^\dagger + \hat{a}_{j'} \right) \tag{E.31}$$

and with coupling parameters

$$g_{j,\alpha} = \sqrt{\frac{\hbar^2 \omega_{\text{c}} N_{\text{QW}} \rho e^2}{2m^* \epsilon_0 \bar{\epsilon} \omega_j \mathbb{V}_j}} \alpha_{j,\alpha}, \tag{E.32}$$

$$h_{j,j'} = \sum_{\gamma \leq j,j'} \frac{g_{j,\gamma}^* g_{j',\gamma}}{\hbar \omega_{\text{c}}}. \tag{E.33}$$

To arrive at the Hamiltonians used in this thesis, we define $\Omega_{\text{R},j,\alpha} = g_{j,\alpha}/(2\pi)$.

The above Hamiltonian can be diagonalised by introducing the hybrid multimode polariton operators,

$$\hat{p}_\beta = \sum_j \left(x_{j,\beta} \hat{a}_j + w_{j,\beta} \hat{b}_j + y_{j,\beta} \hat{a}_j^\dagger + z_{j,\beta} \hat{b}_j^\dagger \right) \tag{E.34}$$

in which $(x_{j,\beta}, w_{j,\beta}, y_{j,\beta}, z_{j,\beta})$ are called Hopfield coefficients, and obey the normalisation condition

$$\sum_j \left(|x_{j,\beta}|^2 + |w_{j,\beta}|^2 - |y_{j,\beta}|^2 - |z_{j,\beta}|^2 \right) = 1. \tag{E.35}$$

The dressed polariton frequencies ω_β are the eigenvalues of the $4n \times 4n$ Hopfield matrix $\mathcal{M}$ representing the Hamiltonian in (E.26), such that

$$\mathcal{M}\mathbf{v}_\beta = \omega_\beta \mathbf{v}_\beta, \tag{E.36}$$

where the eigenvectors are

$$\mathbf{v}_\beta = [x_{1,\beta}, \ldots, x_{n,\beta}, w_{1,\beta}, .., w_{n,\beta}, -y_{1,\beta}, .., -y_{n,\beta}, -z_{1,\beta}, \ldots, -z_{n,\beta},]^T . \tag{E.37}$$

Semi-analytical results for two photonic modes

To arrive at the definitions used in chapter 4, we define the overlap matrix $\mathcal{F}_{j,\mu}$ in a normalized version

$$\eta_{j,\mu} = \frac{\mathcal{F}_{j,\mu}}{\sqrt{\mathcal{F}_{\mu,\mu}\mathcal{F}_{j,j}}}, \tag{E.38}$$

which can assume values from 0 to 1 and quantifies the spatial overlap of each pair of cavity modes in the quantum well plane. Here, a diagonal matrix $\eta_{j,\mu} \propto \delta_{j,\mu}$ implies no overlap, while a full matrix implies a strong overlap.

For two photonic modes ($M = 2$) with frequencies ω_1 and ω_2 and mode volumes $\mathbb{V}_1$ and $\mathbb{V}_2$, their non-orthogonality is given by the single overlap parameter $\tilde{\eta}_{2,1}$. This results in

$$\begin{aligned} \mathcal{F}_{1,1} &= \alpha_{1,1}^2, \\ \mathcal{F}_{2,2} &= |\alpha_{2,1}|^2 + |\alpha_{2,2}|^2, \\ \mathcal{F}_{2,1} &= \alpha_{2,1}^* \alpha_{1,1}, \end{aligned} \tag{E.39}$$

which leads to

$$\begin{aligned}\alpha_{1,1} &= \sqrt{\mathcal{F}_{1,1}},\\ \alpha_{2,1} &= \frac{\mathcal{F}^*_{2,1}}{\sqrt{\mathcal{F}_{1,1}}} = \sqrt{\mathcal{F}_{2,2}}\tilde{\eta}^*_{2,1},\\ \alpha_{2,2} &= \sqrt{\mathcal{F}_{2,2} - \frac{|\mathcal{F}_{2,1}|^2}{\mathcal{F}_{1,1}}} = \sqrt{\mathcal{F}_{2,2}}\sqrt{1-|\tilde{\eta}_{2,1}|^2}.\end{aligned} \tag{E.40}$$

By defining the renormalised mode volume (or length) $\tilde{\mathbb{V}}_j = \frac{\mathbb{V}_j}{\mathcal{F}_{j,j}}$, we arrive at the expressions for the coupling strengths displayed in chapter 4.

Virtual photons in the general case

We calculate the virtual photons number in the system as $\left\langle G \left| \sum_j \hat{a}^\dagger_j \hat{a}_j \right| G \right\rangle$, where the new ground state dressed by the light-matter interaction is defined as $\hat{p}_\beta|G\rangle = 0$. By introducing the inverse Bogoliubov transformation

$$\hat{a}_j = \sum_\beta \left(x^*_{\beta,j}\hat{p}_\beta - y_{\beta,j}\hat{p}^\dagger_\beta \right), \tag{E.41}$$

we obtain

$$\begin{aligned}&\sum_j \left\langle G \left| \hat{a}^\dagger_j \hat{a}_j \right| G \right\rangle = \\ &\sum_j \langle G| \sum_\beta \sum_{\beta'} \left(x_{\beta,j}\hat{p}^\dagger_\beta - y^*_{\beta,j}\hat{p}_\beta \right) \left(x^*_{\beta',j}\hat{p}_{\beta'} - y_{\beta',j}\hat{p}^\dagger_{\beta'} \right) \\ =&\sum_j \sum_\beta |y_{\beta,j}|^2 .\end{aligned} \tag{E.42}$$

E.3. Case of complete orthogonality: no overlap effects

In the case in which the overlap between the photon modes on the 2DEG plane is negligible, our model turns to a standard decoupled modes model, which considers a one-to-one light-matter coupling between the n photon modes and respective n

collective matter modes, and which can be easily resolved by analytical methods.

We can define indeed the collective matter modes straight from the photon shape functions as

$$\hat{b}_j = \mathcal{F}_{j,j}^{-\frac{1}{2}} \sum_l f_j \left(\mathbf{r}_{l,\parallel}\right) \hat{c}_l, \tag{E.43}$$

where the normalization factor is $\mathcal{F}_{j,j}^{\frac{1}{2}} = \sqrt{N_{\mathrm{QW}}\rho} \cdot |\alpha_{j,j}|$ as in eq.(E.24) . If we call $L_j = \mathbb{V}_j / |\alpha_{j,j}|^2$ an effective length for the j-th mode, and then we define

$$g_j = \sqrt{\frac{\hbar^2 \omega_{\mathrm{c}} N_{\mathrm{QW}} \rho e^2}{2m^* \epsilon_0 \bar{\epsilon} \omega_j L_j}}, \tag{E.44}$$

$$h_j = \frac{|g_j|^2}{\omega_{\mathrm{c}}}. \tag{E.45}$$

The final Hamiltonian in eq.(E.26) thus becomes

$$\hat{H} = \sum_j \left[\hbar\omega_j \left(\hat{a}_j^\dagger \hat{a}_j + \frac{1}{2}\right) + \hbar\omega_{\mathrm{c}} \left(\hat{b}_j^\dagger \hat{b}_j + \frac{1}{2}\right) + g_j \left(\hat{b}_j + \hat{b}_j^\dagger\right) \left(\hat{a}_j^\dagger + \hat{a}_j\right) + h_j \left(\hat{a}_j^\dagger + \hat{a}_j\right)^2\right]. \tag{E.46}$$

In this case we can diagonalise the Hamiltonian of each j-th mode separately, by calculating the eigenvalues of the j-th Hopfield matrix expressed in the basis $\left[\hat{a}_j \hat{b}_j \hat{a}_j^\dagger \hat{b}_j^\dagger\right]$:

$$\mathcal{M}_j = \begin{bmatrix} \omega_j + 2h_j & g_j & 2h_j & g_j \\ g_j & \omega_{\mathrm{c}} & g_j & 0 \\ -2h_j & -g_j & -\omega_j - 2h_j & -g_j \\ -g_j & 0 & -g_j & -\omega_{\mathrm{c}} \end{bmatrix}. \tag{E.47}$$

By vanishing the determinant of the matrix $\mathcal{M}_j - \omega_j^\beta I$ with $\beta \in$ [LP, UP], we can obtain the polariton frequencies $\omega_j^{\text{LP, UP}}$ and the Hopfield-Bogoliubov transformations for the polariton operators

$$\hat{p}_{\beta,j} = x_{\beta,j} \hat{a}_j + y_{\beta,j} \hat{a}_j^\dagger + w_{\beta,j} \hat{b}_j + z_{\beta,j} \hat{b}_j^\dagger, \quad \beta \in [\text{LP, UP}]. \tag{E.48}$$

Virtual photons in the orthogonal case

We calculate the virtual photons number $\left\langle G \left| \sum_j \hat{a}_j^\dagger \hat{a}_j \right| G \right\rangle$ exactly as in the general case, by introducing the inverse Bogoliubov transformation

$$\hat{a}_j = \sum_{\beta \in \mathrm{LP,\ UP}} \left(x^*_{\beta,j} \hat{p}_{\beta,j} - y_{\beta,j} \hat{p}^\dagger_{\beta,j} \right) . \tag{E.49}$$

By performing the average in the ground state, we obtain

$$\begin{aligned} &\sum_j \left\langle G \left| \hat{a}_j^\dagger \hat{a}_j \right| G \right\rangle = \\ &\sum_j \langle G| \sum_\beta \sum_{\beta'} \left(x_{\beta,j} \hat{p}^\dagger_{\beta,j} - y^*_{\beta,j} \hat{p}_{\beta,j} \right) \left(x^*_{\beta',j} \hat{p}_{\beta',j} - y_{\beta',j} \hat{p}^\dagger_{\beta',j'} \right) \\ =&\sum_j \left(\left| y_{\mathrm{LP},j} \right|^2 + \left| y_{\mathrm{UP},j} \right|^2 \right) . \end{aligned} \tag{E.50}$$

Appendix F

Publications

Publications in peer review journals

- **J. Mornhinweg**, L. Diebel, M. Halbhuber, J. Riepl, E. Cortese, S. De Liberato, D. Bougeard, R. Huber and C. Lange
  Sculpting ultrastrong light-matter coupling through spatial matter structuring
  submitted

- **J. Mornhinweg**, L. Diebel, M. Halbhuber, M. Prager, J. Riepl, T. Inzenhofer, D. Bougeard, R. Huber and C. Lange
  Mode-multiplexing deep-strong light-matter coupling
  submitted, preprint available at arxiv.org/abs/2309.06915

- E. Cortese, **J. Mornhinweg**, R. Huber, C. Lange and S. De Liberato
  Real-space nanophotonic field manipulation using non-perturbative light–matter coupling
  Optica **10**, 11-19 (2023)

- M. Knorr, J. M. Manceau, **J. Mornhinweg**, J. Nespolo, G. Biasiol, N. L. Tran, M. Malerba, P. Goulain, X. Lafosse, M. Jeannin, M. Stefinger, I. Carusotto, C. Lange, R. Colombelli and R. Huber
  Intersubband polariton-polariton scattering in a dispersive microcavity
  Physical Review Letters **128**, 247401 (2022)

- **J. Mornhinweg**, M. Halbhuber, C. Ciuti, D. Bougeard, R. Huber and C. Lange
  Tailored Subcycle Nonlinearities of Ultrastrong Light-Matter Coupling
  Physical Review Letters **126**, 177404 (2021)

- M. Halbhuber*, **J. Mornhinweg***, V. Zeller, C. Ciuti, D. Bougeard, R. Huber and C. Lange (*: these authors contributed equally)
  Non-adiabatic stripping of a cavity field from electrons in the deep-strong coupling regime
  Nature Photonics **14**, 675-679 (2020) **(Coverstory)**

- P. Steinleitner, P. Merkl, P. Nagler, **J. Mornhinweg**, C. Schüller, T. Korn, A. Chernikov and R. Huber
  Direct Observation of Ultrafast Exciton Formation in a Monolayer of WSe2
  Nano Letters **17**, 1455-1460 (2017)

Reports at international conferences and workshops as presenting author

- **J. Mornhinweg**, M. Halbhuber, L. Diebel, V. Zeller, J. Riepl, D. Bougeard, R. Huber and C. Lange
  Multi-Octave Deep-Strong Light-Matter Coupling of Multiple Modes
  CLEO/Europe-EQEC 2023, Munich, Germany (June 26 - 30, 2023)

- **J. Mornhinweg**, L. Diebel, M. Halbhuber, M. Prager, J. Riepl, T. Inzenhofer, D. Bougeard, R. Huber and C. Lange
  Multi-mode-mixing deep-strong light-matter interaction
  X Ultrafast Dynamics and Metastability & Ultrafast Bandgap Photonics 2023, Hersonissos, Crete, Greece (June 4 - 10, 2023), **(invited talk)**

- **J. Mornhinweg**, M. Halbhuber, L. Diebel, V. Zeller, J. Riepl, D. Bougeard, R. Huber and C. Lange
  Multi-Octave, Multi-Mode Deep-Strong Light-Matter Interaction
  Conference on Lasers and Electro-Optics (CLEO) 2023, San Jose, United States (May 7 -12, 2023)

- **J. Mornhinweg**, M. Halbhuber, L. Diebel, V. Zeller, J. Riepl, C. Ciuti, D. Bougeard, R. Huber and C. Lange
  Ultrafast subcycle dynamics of deep-strong light-matter coupling
  DPG-Meeting 2022 of the Condensed Matter Section, Regensburg, Germany (September 4 - 9, 2022), **(invited talk)**

- **J. Mornhinweg**, M. Halbhuber, C. Ciuti, D. Bougeard, R. Huber and C. Lange
  Nonlinear Subcycle Dynamics of Ultrastrong Light-Matter Interaction
  47th International Conference on Infrared, Millimeter and Terahertz Waves (IRMMW-THz), Delft, Netherlands (August 28 - September 9, 2022)

- **J. Mornhinweg**, M. Halbhuber, C. Ciuti, D. Bougeard, R. Huber and C. Lange
  Nonlinear Subcycle Dynamics of Ultrastrong Light-Matter Coupling
  International Conference on Ultrafast Phenomena, Montreal, Canada (July 18 - 22, 2022)

- **J. Mornhinweg**, M. Halbhuber, C. Ciuti, D. Bougeard, R. Huber and C. Lange
  Subcycle Nonlinearities of Ultrastrong Light-Matter Coupling
  9th International Conference on Optical Terahertz Science and Technology (OTST 2022), Budapest, Hungary (June 19 - 24, 2022)

- **J. Mornhinweg**, M. Halbhuber, V. Zeller, C. Ciuti, D. Bougeard, R. Huber and C. Lange
  Non-Adiabatic Switch-off of Deep-Strong Light-Matter Coupling
  VII Ultrafast Dynamics and Metastability & Ultrafast Bandgap Photonics 2022, Hersonissos, Crete, Greece (June 6 - 10, 2022), **(invited talk)**

- **J. Mornhinweg**, M. Halbhuber, V. Zeller, C. Ciuti, D. Bougeard, C. Lange and R. Huber
  Subcycle Dynamics of Ultrastrong Light-Matter Coupling
  Zoom Workshop QED with strongly correlated quantum materials, Dresden, Germany (virtual) (May 19 - 21, 2021), **(invited talk)**

- **J. Mornhinweg**, M. Halbhuber, V. Zeller, C. Ciuti, D. Bougeard, R. Huber and C. Lange
  Extremely Non-adiabatic Switch-off of Deep-strong Light-Matter Coupling
  CLEO/Europe-EQEC 2021, Munich, Germany (virtual) (June 20 - 24, 2021)

- M. Halbhuber, **J. Mornhinweg**, V. Zeller, C. Ciuti, D. Bougeard, C. Lange and R. Huber
  Extremely Non-Adiabatic Switch-Off of Deep-Strong Light-Matter Coupling
  Conference on Lasers and Electro-Optics (CLEO) 2021, San Jose, United States (virtual) (May 9 -14, 2021)

- **J. Mornhinweg**, M. Halbhuber, C. Ciuti, D. Bougeard, R. Huber and C. Lange
  Non-perturbative Subcycle Nonlinearities of Ultrastrong Light-Matter Coupling
  Conference on Lasers and Electro-Optics (CLEO) 2021, San Jose, United States (virtual) (May 9 - 14, 2021)

- **J. Mornhinweg**, M. Halbhuber, V. Zeller, C. Ciuti, D. Bougeard, R. Huber and C. Lange
  Extremely Non-Adiabatic Switching of Deep-Strong Light-Matter Coupling
  The 22nd International Conference on Ultrafast Phenomena (UP2020), Shanghai, China (virtual) (November 16 - 19, 2020)

- **J. Mornhinweg**, M. Halbhuber, V. Zeller, C. Ciuti, D. Bougeard, R. Huber and C. Lange
  Quasi-instantaneous switch-off of deep-strong light-matter coupling
  9th International Workshop on Terahertz Technology and Applications, Kaiserslautern, Germany (March 3 -4, 2020)

Conference proceedings

- **J. Mornhinweg**, L. Diebel, M. Halbhuber, V. Zeller, J. Riepl, T. Inzenhofer, D. Bougeard, R. Huber and C. Lange
  Multi-Octave Deep-Strong Light-Matter Coupling of Multiple Modes
  Conference on Lasers and Electro-Optics/Europe (CLEO/Europe 2023) and European Quantum Electronics Conference (EQEC 2023), Technical Digest Series (Optica Publishing Group, 2023), paper eg.4.3

- **J. Mornhinweg**, L. Diebel, M. Halbhuber, M. Prager, J. Riepl, T. Inzenhofer, D. Bougeard, R. Huber and C. Lange
  Multi-mode-mixing deep-strong light-matter interaction
  X Ultrafast Dynamics and Metastability & Ultrafast Bandgap Photonics 2023 Abstract Proceedings, page 111

- **J. Mornhinweg**, M. Halbhuber, L. Diebel, V. Zeller, J. Riepl, D. Bougeard, R. Huber and C. Lange
  Multi-Octave, Multi-Mode Deep-Strong Light-Matter Interaction
  CLEO 2023, Technical Digest Series (Optica Publishing Group, 2023), paper FW3N.3

- **J. Mornhinweg**, M. Halbhuber, L. Diebel, V. Zeller, J. Riepl, C. Ciuti., D. Bougeard, R. Huber and C. Lange
  Ultrafast subcycle dynamics of deep-strong light-matter coupling
  DPG-Meeting 2022 of the Condensed Matter Section, HL 40.5

- **J. Mornhinweg**, M. Halbhuber, C. Ciuti, D. Bougeard, R. Huber and C. Lange
  Nonlinear Subcycle Dynamics of Ultrastrong Light-Matter Interaction
  47th International Conference on Infrared, Millimeter and Terahertz Waves (IRMMW-THz), We-PM1-2

- **J. Mornhinweg**, M. Halbhuber, C. Ciuti, D. Bougeard, R. Huber and C. Lange
  Nonlinear Subcycle Dynamics of Ultrastrong Light-Matter Coupling
  The International Conference on Ultrafast Phenomena (UP) 2022, Technical Digest Series (Optica Publishing Group, 2022), paper Th3A.2

- M. Knorr, J.-M. Manceau, **J. Mornhinweg**, J. Nespolo, G. Biasiol, N.L. Tran, M. Malerba, P. Goulain, X. Lafosse, I. Carusotto, C. Lange, R. Colombelli and R. Huber
  Ultrafast Non-Collinear Pump-Probe Spectroscopy of Intersubband Polariton-Polariton Scattering
  Conference on Lasers and Electro-Optics, OSA Technical Digest (Optica Publishing Group, 2022), paper FTu5B.2

- E. Cortese, **J. Mornhinweg**, C. Lange and S. De Liberato
  Real-space nanophotonic field manipulation using Landau polaritons
  Conference on Lasers and Electro-Optics, OSA Technical Digest (Optica Publishing Group, 2022), paper JW3B.164

- **J. Mornhinweg**, M. Halbhuber, C. Ciuti, D. Bougeard, R. Huber and C. Lange
  Subcycle Nonlinearities of Ultrastrong Light-Matter Coupling
  9th International Conference on Optical Terahertz Science and Technology (OTST 2022), paper O-53

- **J. Mornhinweg**, M. Halbhuber, V. Zeller, C. Ciuti, D. Bougeard, R. Huber and C. Lange
  Non-Adiabatic Switch-off of Deep-Strong Light-Matter Coupling
  VII Ultrafast Dynamics and Metastability & Ultrafast Bandgap Photonics 2021, paper IX4

- **J. Mornhinweg**, M. Halbhuber, V. Zeller, C. Ciuti, D. Bougeard, C. Lange and R. Huber
  Subcycle Dynamics of Ultrastrong Light-Matter Coupling
  Zoom Workshop QED with strongly correlated quantum materials

- **J. Mornhinweg**, M. Halbhuber, V. Zeller, C. Ciuti, D. Bougeard, R. Huber and C. Lange
  Extremely Non-adiabatic Switch-off of Deep-strong Light-Matter Coupling
  2021 Conference on Lasers and Electro-Optics Europe and European Quantum Electronics Conference, OSA Technical Digest (Optica Publishing Group, 2021), paper eg.4.1

- Maike Halbhuber, **J. Mornhinweg**, V. Zeller, C. Ciuti, D. Bougeard, C. Lange and R. Huber
  Extremely Non-Adiabatic Switch-Off of Deep-Strong Light-Matter Coupling
  Conference on Lasers and Electro-Optics, OSA Technical Digest (Optica Publishing Group, 2021), paper FW2Q.1

- **J. Mornhinweg**, M. Halbhuber, C. Ciuti, D. Bougeard, R. Huber and C. Lange
  Non-perturbative Subcycle Nonlinearities of Ultrastrong Light-Matter Coupling
  Conference on Lasers and Electro-Optics, OSA Technical Digest (Optica Publishing Group, 2021), paper FTh4L.3

- C. Lange, **J. Mornhinweg**, M. Halbhuber, V. Zeller, C. Ciuti, D. Bougeard and R. Huber
  Non-adiabatic switch-off and subcycle nonlinearities of deep-strong light-matter coupling
  JSAP Annual Meetings Extended Abstracts The 68th JSAP Spring Meeting 2021, page 75

- **J. Mornhinweg**, M. Halbhuber, V. Zeller, C. Ciuti, D. Bougeard, R. Huber and C. Lange
  Extremely Non-Adiabatic Switching of Deep-Strong Light-Matter Coupling
  The 22nd International Conference on Ultrafast Phenomena 2020, OSA Technical Digest (Optica Publishing Group, 2020), paper W3B.2

- **J. Mornhinweg**, M. Halbhuber, V. Zeller, C. Ciuti, D. Bougeard, R. Huber and C. Lange
  Quasi-instantaneous switch-off of deep-strong light-matter coupling
  9th International Workshop on Terahertz Technology and Applications, poster 29

Awards

- EPS-QEOD Travel Grant Student Award
  Multi-Octave Deep-Strong Light-Matter Coupling of Multiple Modes
  CLEO/Europe-EQEC 2023, Munich, Germany (June 26 - 30, 2023)

- First place of the “Best Student Presentation Award”
  Nonlinear Subcycle Dynamics of Ultrastrong Light-Matter Interaction
  47th International Conference on Infrared, Millimeter and Terahertz Waves (IRMMW-THz), Delft, Netherlands (August 28 - September 9, 2022)

Bibliography

[All83] S. J. Allen, H. L. Störmer, and J. C. M. Hwang, *Dimensional resonance of the two-dimensional electron gas in selectively doped GaAs/AlGaAs heterostructures*, Physical Review B **28**, 4875–4877 (1983).

[Ana09] A. A. Anappara, S. De Liberato, A. Tredicucci, C. Ciuti, G. Biasiol, L. Sorba, and F. Beltram, *Signatures of the ultrastrong light-matter coupling regime*, Physical Review B **79**, 201303 (2009).

[App22] F. Appugliese, J. Enkner, G. L. Paravicini-Bagliani, M. Beck, C. Reichl, W. Wegscheider, G. Scalari, C. Ciuti, and J. Faist, *Breakdown of topological protection by cavity vacuum fields in the integer quantum Hall effect*, Science (New York, N.Y.) **375**, 1030–1034 (2022).

[Bac92] W. H. Backes, F. M. Peeters, F. Brosens, and J. T. Devreese, *Dispersion of longitudinal plasmons for a quasi-two-dimensional electron gas*, Physical Review B **45**, 8437–8442 (1992).

[Bai17] S. Baierl, *Nichtlineare Spinkontrolle mitultrakurzen THz-Feldern*, PhD thesis, University of Regensburg (2017).

[Bak13] A. Baksic, P. Nataf, and C. Ciuti, *Superradiant phase transitions with three-level systems*, Physical Review A **87**, 023813 (2013).

[Bal21] M. Balasubrahmaniyam, C. Genet, and T. Schwartz, *Coupling and decoupling of polaritonic states in multimode cavities*, Physical Review B **103**, L241407 (2021).

[Bar18] N. Bartolo and C. Ciuti, *Vacuum-dressed cavity magnetotransport of a two-dimensional electron gas*, Physical Review B **98**, 205301 (2018).

[Bas21] D. N. Basov, A. Asenjo-Garcia, P. J. Schuck, X. Zhu, and A. Rubio, *Polariton panorama*, Nanophotonics **10**, 549–577 (2021).

[Bay17] A. Bayer, M. Pozimski, S. Schambeck, D. Schuh, R. Huber, D. Bougeard, and C. Lange, *Terahertz Light–Matter Interaction beyond Unity Coupling Strength*, Nano Letters **17**, 6340–6344 (2017).

[BB79] I. Bialynicki-Birula and K. Rza żewski, *No-go theorem concerning the superradiant phase transition in atomic systems*, Physical Review A **19**, 301–303 (1979).

[BC19] I.-C. Benea-Chelmus, F. F. Settembrini, G. Scalari, and J. Faist, *Electric field correlation measurements on the electromagnetic vacuum state*, Nature **568**, 202–206 (2019).

[Bon17] I. V. Bondarev and V. M. Shalaev, *Universal features of the optical properties of ultrathin plasmonic films*, Optical Materials Express **7**, 3731–3740 (2017).

[Bor23] M. Borsch, M. Meierhofer, R. Huber, and M. Kira, *Lightwave electronics in condensed matter*, Nature Reviews Materials, 1–20 (2023).

[Boy08] R. W. Boyd, *Nonlinear Optics*, 3. ed., Elsevier, Acad. Press, Amsterdam.

[Bro17] S. Brodbeck, S. De Liberato, M. Amthor, M. Klaas, M. Kamp, L. Worschech, C. Schneider, and S. Höfling, *Experimental Verification of the Very Strong Coupling Regime in a GaAs Quantum Well Microcavity*, Physical Review Letters **119**, 027401 (2017).

[Car13] I. Carusotto and C. Ciuti, *Quantum fluids of light*, Reviews of Modern Physics **85**, 299–366 (2013).

[Cas48] H. B. G. Casimir, *On the Attraction Between Two Perfectly Conducting Plates*, Indag. Math. **10**, 261–263 (1948).

[Che06] H.-T. Chen, W. J. Padilla, J. M. O. Zide, A. C. Gossard, A. J. Taylor, and R. D. Averitt, *Active terahertz metamaterial devices*, Nature **444**, 597–600 (2006).

[Che07] H.-T. Chen, J. F. O'Hara, A. J. Taylor, R. D. Averitt, C. Highstrete, M. Lee, and W. J. Padilla, *Complementary planar terahertz metamaterials*, Optics Express **15**, 1084–1095 (2007).

[Che08] H.-T. Chen, J. F. O'Hara, A. K. Azad, A. J. Taylor, R. D. Averitt, D. B. Shrekenhamer, and W. J. Padilla, *Experimental demonstration of frequency-agile terahertz metamaterials*, Nature Photonics **2**, 295–298 (2008).

[Che16] H.-T. Chen, A. J. Taylor, and N. Yu, *A review of metasurfaces: physics and applications*, Reports on Progress in Physics **79**, 076401 (2016).

[Chi01] A. H. Chin, O. G. Calderón, and J. Kono, *Extreme Midinfrared Nonlinear Optics in Semiconductors*, Physical Review Letters **86**, 3292–3295 (2001).

[Chi16] R. Chikkaraddy, B. de Nijs, F. Benz, S. J. Barrow, O. A. Scherman, E. Rosta, A. Demetriadou, P. Fox, O. Hess, and J. J. Baumberg, *Single-molecule strong coupling at room temperature in plasmonic nanocavities*, Nature **535**, 127–130 (2016).

[Ciu05] C. Ciuti, G. Bastard, and I. Carusotto, *Quantum vacuum properties of the intersubband cavity polariton field*, Physical Review B **72**, 115303 (2005).

[Cor07] P. B. Corkum and F. Krausz, *Attosecond science*, Nature Physics **3**, 381–387 (2007).

[Cor21] E. Cortese, N.-L. Tran, J.-M. Manceau, A. Bousseksou, I. Carusotto, G. Biasiol, R. Colombelli, and S. De Liberato, *Excitons bound by photon exchange*, Nature Physics **17**, 31–35 (2021).

[Cor23] E. Cortese, J. Mornhinweg, R. Huber, C. Lange, and S. De Liberato, *Real-space nanophotonic field manipulation using non-perturbative light–matter coupling*, Optica **10**, 11–19 (2023).

[Dem90] T. Demel, D. Heitmann, P. Grambow, and K. Ploog, *Nonlocal dynamic response and level crossings in quantum-dot structures*, Physical Review Letters **64**, 788–791 (1990).

[Den10] H. Deng, H. Haug, and Y. Yamamoto, *Exciton-polariton Bose-Einstein condensation*, Reviews of Modern Physics **82**, 1489–1537 (2010).

[Dic54] R. H. Dicke, *Coherence in Spontaneous Radiation Processes*, Physical Review **93**, 99–110 (1954).

[Die20] L. Diebel, *Jenseits ultrastarker Licht-Materie-Kopplung: Subzyklen-Kontrollevon Vakuumfeldern in neuartigen THz-Resonatoren*, master's thesis, University of Regensburg (2020).

[Dir27] P. A. M. Dirac and N. H. D. Bohr, *The quantum theory of the emission and absorption of radiation*, Proceedings of the Royal Society of London. Series A, Containing Papers of a Mathematical and Physical Character **114**, 243-265 (1927).

[DL14] S. De Liberato, *Light-Matter Decoupling in the Deep Strong Coupling Regime: The Breakdown of the Purcell Effect*, Physical Review Letters **112**, 016401 (2014).

[DL17] S. De Liberato, *Virtual photons in the ground state of a dissipative system*, Nature Communications **8**, 1465 (2017).

[Dun22] A. D. Dunkelberger, B. S. Simpkins, I. Vurgaftman, and J. C. Owrutsky, *Vibration-Cavity Polariton Chemistry and Dynamics*, Annual Review of Physical Chemistry **73**, 429–451 (2022).

[Dys49] F. J. Dyson, *The Radiation Theories of Tomonaga, Schwinger, and Feynman*, Physical Review **75**, 486–502 (1949).

[Egu75] A. Eguiluz, T. K. Lee, J. J. Quinn, and K. W. Chiu, *Interface excitations in metal-insulator-semiconductor structures*, Physical Review B **11**, 4989–4993 (1975).

[Ein16] A. Einstein, *Strahlungs-Emission und Absorption nach der Quantentheorie*, Deutsche Physikalische Gesellschaft **18**, 318–323 (1916).

[FD19] P. Forn-Díaz, L. Lamata, E. Rico, J. Kono, and E. Solano, *Ultrastrong coupling regimes of light-matter interaction*, Reviews of Modern Physics **91**, 025005 (2019).

[Fed16] S. Fedortchenko, S. Huppert, A. Vasanelli, Y. Todorov, C. Sirtori, C. Ciuti, A. Keller, T. Coudreau, and P. Milman, *Output squeezed radiation from dispersive ultrastrong light-matter coupling*, Physical Review A **94**, 013821 (2016).

[Fel14] S. Felicetti, G. Romero, D. Rossini, R. Fazio, and E. Solano, *Photon transfer in ultrastrongly coupled three-cavity arrays*, Physical Review A **89**, 013853 (2014).

[Fet86] A. L. Fetter, *Magnetoplasmons in a two-dimensional electron fluid: Disk geometry*, Physical Review B **33**, 5221–5227 (1986).

[FK19] A. Frisk Kockum, A. Miranowicz, S. De Liberato, S. Savasta, and F. Nori, *Ultrastrong coupling between light and matter*, Nature Reviews Physics **1**, 19–40 (2019).

[Gar13] L. Garziano, A. Ridolfo, R. Stassi, O. Di Stefano, and S. Savasta, *Switching on and off of ultrastrong light-matter interaction: Photon statistics of quantum vacuum radiation*, Physical Review A **88**, 063829 (2013).

[Gar17] L. Garziano, A. Ridolfo, S. De Liberato, and S. Savasta, *Cavity QED in the Ultrastrong Coupling Regime: Photon Bunching from the Emission of Individual Dressed Qubits*, ACS Photonics **4**, 2345–2351 (2017).

[Gen17] P. Genevet, F. Capasso, F. Aieta, M. Khorasaninejad, and R. Devlin, *Recent advances in planar optics: from plasmonic to dielectric metasurfaces*, Optica **4**, 139–152 (2017).

[Gha98] H. F. Ghaemi, T. Thio, D. E. Grupp, T. W. Ebbesen, and H. J. Lezec, *Surface plasmons enhance optical transmission through subwavelength holes*, Physical Review B **58**, 6779–6782 (1998).

[Gla85] D. C. Glattli, E. Y. Andrei, G. Deville, J. Poitrenaud, and F. I. B. Williams, *Dynamical Hall Effect in a Two-Dimensional Classical Plasma*, Physical Review Letters **54**, 1710–1713 (1985).

[Gü09] G. Günter, A. A. Anappara, J. Hees, A. Sell, G. Biasiol, L. Sorba, S. De Liberato, C. Ciuti, A. Tredicucci, and A. Leitenstorfer, *Sub-cycle switch-on of ultrastrong light–matter interaction*, Nature **458**, 178–181 (2009).

[Hag10] D. Hagenmüller, S. De Liberato, and C. Ciuti, *Ultrastrong coupling between a cavity resonator and the cyclotron transition of a two-dimensional electron gas in the case of an integer filling factor*, Physical Review B **81**, 235303 (2010).

[Hal20] M. Halbhuber, J. Mornhinweg, V. Zeller, C. Ciuti, D. Bougeard, R. Huber, and C. Lange, *Non-adiabatic stripping of a cavity field from electrons in the deep-strong coupling regime*, Nature photonics **14**, 675–679 (2020).

[Hal21] M. Halbhuber, *Subcycle dynamics of deep-strong light-matter coupling*, PhD thesis, University of Regensburg (2021).

[Has17] M. R. Hashemi, S. Cakmakyapan, and M. Jarrahi, *Reconfigurable metamaterials for terahertz wave manipulation*, Reports on Progress in Physics **80**, 094501 (2017).

[Haw74] S. W. Hawking, *Black hole explosions?*, Nature **248**, 30–31 (1974).

[Haw75] S. W. Hawking, *Particle creation by black holes*, Communications in Mathematical Physics **43**, 199–220 (1975).

[Hep73] K. Hepp and E. H. Lieb, *On the superradiant phase transition for molecules in a quantized radiation field: the dicke maser model*, Annals of Physics **76**, 360–404 (1973).

[Her16] F. Herrera and F. C. Spano, *Cavity-Controlled Chemistry in Molecular Ensembles*, Physical Review Letters **116**, 238301 (2016).

[Hoh15] M. Hohenleutner, F. Langer, O. Schubert, M. Knorr, U. Huttner, S. W. Koch, M. Kira, and R. Huber, *Real-time observation of interfering crystal electrons in high-harmonic generation*, Nature **523**, 572–575 (2015).

[Hop58] J. J. Hopfield, *Theory of the Contribution of Excitons to the Complex Dielectric Constant of Crystals*, Physical Review **112**, 1555–1567 (1958).

[Hu19] Y. Hu, T. Jiang, J. Zhou, H. Hao, H. Sun, H. Ouyang, M. Tong, Y. Tang, H. Li, J. You, X. Zheng, Z. Xu, and X. Cheng, *Ultrafast Terahertz Frequency and Phase Tuning by All-Optical Molecularization of Metasurfaces*, Advanced Optical Materials **7**, 1901050 (2019).

[Hua91] D. Huang and G. Gumbs, *Tunneling and anticrossing of edge magnetoplasmons in a quantum-dot superlattice*, Physical Review B **43**, 12039–12041 (1991).

[Hub01] R. Huber, F. Tauser, A. Brodschelm, M. Bichler, G. Abstreiter, and A. Leitenstorfer, *How many-particle interactions develop after ultrafast excitation of an electron–hole plasma*, Nature **414**, 286–289 (2001).

[Hut12] J. A. Hutchison, T. Schwartz, C. Genet, E. Devaux, and T. W. Ebbesen, *Modifying Chemical Landscapes by Coupling to Vacuum Fields*, Angewandte Chemie International Edition **51**, 1592–1596 (2012).

[Irm96] G. Irmer, M. Wenzel, and J. Monecke, *The temperature dependence of the LO(T) and TO(T) phonons in GaAs and InP*, physica status solidi (b) **195**, 85–95 (1996).

[Jay63] E. Jaynes and F. Cummings, *Comparison of quantum and semiclassical radiation theories with application to the beam maser*, Proceedings of the IEEE **51**, 89–109 (1963).

[Joh13] J. R. Johansson, P. D. Nation, and F. Nori, *QuTiP 2: A Python framework for the dynamics of open quantum systems*, Computer Physics Communications **184**, 1234–1240 (2013).

[Jun12] F. Junginger, B. Mayer, C. Schmidt, O. Schubert, S. Mährlein, A. Leitenstorfer, R. Huber, and A. Pashkin, *Nonperturbative Interband Response of a Bulk InSb Semiconductor Driven Off Resonantly by Terahertz Electromagnetic Few-Cycle Pulses*, Physical Review Letters **109**, 147403 (2012).

[Kaf12] M. Kafesaki, N. H. Shen, S. Tzortzakis, and C. M. Soukoulis, *Optically switchable and tunable terahertz metamaterials through photoconductivity*, Journal of Optics **14**, 114008 (2012).

[Kal83] Y. Kaluzny, P. Goy, M. Gross, J. M. Raimond, and S. Haroche, *Observation of Self-Induced Rabi Oscillations in Two-Level Atoms Excited Inside a Resonant Cavity: The Ringing Regime of Superradiance*, Physical Review Letters **51**, 1175–1178 (1983).

[Kel17a] J. Keller, C. Maissen, J. Haase, G. L. Paravicini-Bagliani, F. Valmorra, J. Palomo, J. Mangeney, J. Tignon, S. S. Dhillon, G. Scalari, and J. Faist, *Coupling Surface Plasmon Polariton Modes to Complementary THz Metasurfaces Tuned by Inter Meta-Atom Distance*, Advanced Optical Materials **5**, 1600884 (2017).

[Kel17b] J. Keller, G. Scalari, S. Cibella, C. Maissen, F. Appugliese, E. Giovine, R. Leoni, M. Beck, and J. Faist, *Few-Electron Ultrastrong Light-Matter Coupling at 300 GHz with Nanogap Hybrid LC Microcavities*, Nano Letters **17**, 7410–7415 (2017).

[Kel18] J. Keller, G. Scalari, F. Appugliese, E. Mavrona, S. Rajabali, M. J. Süess, M. Beck, and J. Faist, *High Tc Superconducting THz Metamaterial for Ultrastrong Coupling in a Magnetic Field*, ACS Photonics **5**, 3977–3983 (2018).

[Kin99] J. T. Kindt and C. A. Schmuttenmaer, *Theory for determination of the low-frequency time-dependent response function in liquids using time-resolved terahertz pulse spectroscopy*, Journal of Chemical Physics **110**, 8589–8596 (1999).

[Kno22] M. Knorr, J.-M. Manceau, J. Mornhinweg, J. Nespolo, G. Biasiol, N.-L. Tran, M. Malerba, P. Goulain, X. Lafosse, and M. Jeannin, *Intersubband* *polariton-polariton scattering in a dispersive microcavity*, Physical Review Letters **128**, 247401 (2022).

[KO17] J. C. König-Otto, Y. Wang, A. Belyanin, C. Berger, W. A. de Heer, M. Orlita, A. Pashkin, H. Schneider, M. Helm, and S. Winnerl, *Four-Wave Mixing in Landau-Quantized Graphene*, Nano Letters **17**, 2184–2188 (2017).

[Koc17] A. F. Kockum, A. Miranowicz, V. Macrì, S. Savasta, and F. Nori, *Deterministic quantum nonlinear optics with single atoms and virtual photons*, Physical Review A **95**, 063849 (2017).

[Koh61] W. Kohn, *Cyclotron Resonance and de Haas-van Alphen Oscillations of an Interacting Electron Gas*, Physical Review **123**, 1242–1244 (1961).

[Kub66] R. Kubo, *The fluctuation-dissipation theorem*, Reports on Progress in Physics **29**, 255 (1966).

[Kue09] W. Kuehn, K. Reimann, M. Woerner, and T. Elsaesser, *Phase-resolved two-dimensional spectroscopy based on collinear n-wave mixing in the ultrafast time domain*, The Journal of Chemical Physics **130**, 164503 (2009).

[Kue11] W. Kuehn, K. Reimann, M. Woerner, T. Elsaesser, R. Hey, and U. Schade, *Strong Correlation of Electronic and Lattice Excitations in GaAs/AlGaAs Semiconductor Quantum Wells Revealed by Two-Dimensional Terahertz Spectroscopy*, Physical Review Letters **107**, 067401 (2011).

[Kus01] M. S. Kushwaha, *Plasmons and magnetoplasmons in semiconductor heterostructures*, Surface Science Reports **41**, 1–416 (2001).

[Lam47] W. E. Lamb and R. C. Retherford, *Fine Structure of the Hydrogen Atom by a Microwave Method*, Physical Review **72**, 241–243 (1947).

[Lam96] A. Lambrecht, M.-T. Jaekel, and S. Reynaud, *Motion Induced Radiation from a Vibrating Cavity*, Physical Review Letters **77**, 615–618 (1996).

[Lan14] C. Lange, T. Maag, M. Hohenleutner, S. Baierl, O. Schubert, E. Edwards, D. Bougeard, G. Woltersdorf, and R. Huber, *Extremely Nonperturbative*

Nonlinearities in GaAs Driven by Atomically Strong Terahertz Fields in Gold Metamaterials, Physical Review Letters **113**, 227401 (2014).

[Lan16] F. Langer, M. Hohenleutner, C. P. Schmid, C. Poellmann, P. Nagler, T. Korn, C. Schüller, M. S. Sherwin, U. Huttner, J. T. Steiner, S. W. Koch, M. Kira, and R. Huber, *Lightwave-driven quasiparticle collisions on a subcycle timescale*, Nature **533**, 225–229 (2016).

[Lei99] A. Leitenstorfer, S. Hunsche, J. Shah, M. C. Nuss, and W. H. Knox, *Detectors and sources for ultrabroadband electro-optic sampling: Experiment and theory*, Applied Physics Letters **74**, 1516–1518 (1999).

[Li18] X. Li, M. Bamba, Q. Zhang, S. Fallahi, G. C. Gardner, W. Gao, M. Lou, K. Yoshioka, M. J. Manfra, and J. Kono, *Vacuum Bloch–Siegert shift in Landau polaritons with ultra-high cooperativity*, Nature Photonics **12**, 324–329 (2018).

[Lib07] S. D. Liberato, C. Ciuti, and I. Carusotto, *Quantum Vacuum Radiation Spectra from a Semiconductor Microcavity with a Time-Modulated Vacuum Rabi Frequency*, Physical Review Letters **98**, 103602 (2007).

[Liu15] X. Liu, H. Liu, Q. Sun, and N. Huang, *Metamaterial terahertz switch based on split-ring resonator embedded with photoconductive silicon*, Applied Optics **54**, 3478–3483 (2015).

[Loc05] D. J. Lockwood, G. Yu, and N. L. Rowell, *Optical phonon frequencies and damping in AlAs, GaP, GaAs, InP, InAs and InSb studied by oblique incidence infrared spectroscopy*, Solid State Communications **136**, 404–409 (2005).

[Maa16] T. Maag, A. Bayer, S. Baierl, M. Hohenleutner, T. Korn, C. Schüller, D. Schuh, D. Bougeard, C. Lange, R. Huber, M. Mootz, J. E. Sipe, S. W. Koch, and M. Kira, *Coherent cyclotron motion beyond Kohn's theorem*, Nature Physics **12**, 119–123 (2016).

[Mai14] C. Maissen, G. Scalari, F. Valmorra, M. Beck, J. Faist, S. Cibella, R. Leoni, C. Reichl, C. Charpentier, and W. Wegscheider, *Ultrastrong coupling in* *the near field of complementary split-ring resonators*, Physical Review B **90**, 205309 (2014).

[Mak21] T. Makihara, K. Hayashida, G. T. Noe II, X. Li, N. Marquez Peraca, X. Ma, Z. Jin, W. Ren, G. Ma, I. Katayama, J. Takeda, H. Nojiri, D. Turchinovich, S. Cao, M. Bamba, and J. Kono, *Ultrastrong magnon–magnon coupling dominated by antiresonant interactions*, Nature Communications **12**, 3115 (2021).

[Mas85] D. B. Mast, A. J. Dahm, and A. L. Fetter, *Observation of Bulk and Edge Magnetoplasmons in a Two-Dimensional Electron Fluid*, Physical Review Letters **54**, 1706–1709 (1985).

[Mic81] A. A. Michelson, *The relative motion of the Earth and of the luminiferous ether*, American Journal of Science **s3-22**, 120–129 (1881).

[Mil13] P. W. Milonni, *The Quantum Vacuum: An Introduction to Quantum Electrodynamics*, Academic Press (2013).

[Moo70] G. T. Moore, *Quantum Theory of the Electromagnetic Field in a Variable-Length One-Dimensional Cavity*, Journal of Mathematical Physics **11**, 2679-2691 (1970).

[Mor21] J. Mornhinweg, M. Halbhuber, C. Ciuti, D. Bougeard, R. Huber, and C. Lange, *Tailored subcycle nonlinearities of ultrastrong light-matter coupling*, Physical Review Letters **126**, 177404 (2021).

[Mor23a] J. Mornhinweg, L. Diebel, M. Halbhuber, M. Prager, J. Riepl, T. Inzenhofer, D. Bougeard, R. Huber, and C. Lange, *Mode-multiplexing deep-strong light-matter coupling*, (submitted), Preprint available at arxiv.org/abs/2309.06915 (2023).

[Mor23b] J. Mornhinweg, L. Diebel, M. Halbhuber, J. Riepl, E. Cortese, S. De Liberato, D. Bougeard, R. Huber, and C. Lange, *Sculpting ultrastrong light-matter coupling through spatial matter structuring*, (submitted) (2023).

[Mue20] N. S. Mueller, Y. Okamura, B. G. M. Vieira, S. Juergensen, H. Lange, E. B. Barros, F. Schulz, and S. Reich, *Deep strong light–matter coupling in plasmonic nanoparticle crystals*, Nature **583**, 780–784 (2020).

[Mur20] V. M. Muravev and I. V. Kukushkin, *Collective plasma excitations in two-dimensional electron systems*, Physics-Uspekhi **63**, 975 (2020).

[Mü01] O. D. Mücke, T. Tritschler, M. Wegener, U. Morgner, and F. X. Kärtner, *Signatures of Carrier-Wave Rabi Flopping in GaAs*, Physical Review Letters **87**, 057401 (2001).

[Nah96] A. Nahata, A. S. Weling, and T. F. Heinz, *A wideband coherent terahertz spectroscopy system using optical rectification and electro-optic sampling*, Applied Physics Letters **69**, 2321–2323 (1996).

[New18] I. Newton, *Opticks: Or, A Treatise of the Reflections, Refractions, Inflexions and Colours of Light. The Second Edition, with Additions*, The Newton Project, online Catalouge entry NATP00051 (1718).

[Org15] E. Orgiu, J. George, J. A. Hutchison, E. Devaux, J. F. Dayen, B. Doudin, F. Stellacci, C. Genet, J. Schachenmayer, C. Genes, G. Pupillo, P. Samorì, and T. W. Ebbesen, *Conductivity in organic semiconductors hybridized with the vacuum field*, Nature Materials **14**, 1123–1129 (2015).

[Pad06] W. J. Padilla, A. J. Taylor, C. Highstrete, M. Lee, and R. D. Averitt, *Dynamical Electric and Magnetic Metamaterial Response at Terahertz Frequencies*, Physical Review Letters **96**, 107401 (2006).

[PB19] G. L. Paravicini-Bagliani, F. Appugliese, E. Richter, F. Valmorra, J. Keller, M. Beck, N. Bartolo, C. Rössler, T. Ihn, K. Ensslin, C. Ciuti, G. Scalari, and J. Faist, *Magneto-transport controlled by Landau polariton states*, Nature Physics **15**, 186–190 (2019).

[Pel21] D. Peller, C. Roelcke, L. Z. Kastner, T. Buchner, A. Neef, J. Hayes, F. Bonafé, D. Sidler, M. Ruggenthaler, A. Rubio, R. Huber, and J. Repp, *Quantitative sampling of atomic-scale electromagnetic waveforms*, Nature Photonics **15**, 143–147 (2021).

[Pen99] J. Pendry, A. Holden, D. Robbins, and W. Stewart, *Magnetism from conductors and enhanced nonlinear phenomena*, IEEE Transactions on Microwave Theory and Techniques **47**, 2075–2084 (1999).

[Pes95] M. E. Peskin and D. V. Schroeder, *An Introduction To Quantum Field Theory*, Avalon Publishing (1995).

[Pop05] V. V. Popov, O. V. Polischuk, and M. S. Shur, *Resonant excitation of plasma oscillations in a partially gated two-dimensional electron layer*, Journal of Applied Physics **98**, 033510 (2005).

[Pur46] E. M. Purcell, *Spontaneous Emission Probabilities at Radio Frequencies, Proceedings of the American Physical Society*, Physical Review **69**, 674–674 (1946).

[Raa19] J. Raab, C. Lange, J. L. Boland, I. Laepple, M. Furthmeier, E. Dardanis, N. Dessmann, L. Li, E. H. Linfield, A. G. Davies, M. S. Vitiello, and R. Huber, *Ultrafast two-dimensional field spectroscopy of terahertz intersubband saturable absorbers*, Optics Express **27**, 2248–2257 (2019).

[Rab37] I. I. Rabi, *Space Quantization in a Gyrating Magnetic Field*, Physical Review **51**, 652–654 (1937).

[Raj21] S. Rajabali, E. Cortese, M. Beck, S. De Liberato, J. Faist, and G. Scalari, *Polaritonic nonlocality in light–matter interaction*, Nature Photonics **15**, 690–695 (2021).

[Rid12] A. Ridolfo, M. Leib, S. Savasta, and M. J. Hartmann, *Photon Blockade in the Ultrastrong Coupling Regime*, Physical Review Letters **109**, 193602 (2012).

[Rid13] A. Ridolfo, S. Savasta, and M. J. Hartmann, *Nonclassical Radiation from Thermal Cavities in the Ultrastrong Coupling Regime*, Physical Review Letters **110**, 163601 (2013).

[Rie15] C. Riek, D. V. Seletskiy, A. S. Moskalenko, J. F. Schmidt, P. Krauspe, S. Eckart, S. Eggert, G. Burkard, and A. Leitenstorfer, *Direct sampling of* *electric-field vacuum fluctuations*, Science (New York, N.Y.) **350**, 420–423 (2015).

[Rza75] K. Rzażewski, K. Wódkiewicz, and W. Żakowicz, *Phase Transitions, Two-Level Atoms, and the A^2 Term*, Physical Review Letters **35**, 432–434 (1975).

[Sca12] G. Scalari, C. Maissen, D. Turcinková, D. Hagenmüller, S. De Liberato, C. Ciuti, C. Reichl, D. Schuh, W. Wegscheider, M. Beck, and J. Faist, *Ultrastrong coupling of the cyclotron transition of a 2D electron gas to a THz metamaterial*, Science (New York, N.Y.) **335**, 1323–1326 (2012).

[Sch14] O. Schubert, M. Hohenleutner, F. Langer, B. Urbanek, C. Lange, U. Huttner, D. Golde, T. Meier, M. Kira, S. W. Koch, and R. Huber, *Sub-cycle control of terahertz high-harmonic generation by dynamical Bloch oscillations*, Nature Photonics **8**, 119–123 (2014).

[Sch19] F. Schlawin, A. Cavalleri, and D. Jaksch, *Cavity-Mediated Electron-Photon Superconductivity*, Physical Review Letters **122**, 133602 (2019).

[Sch22] F. Schlawin, D. M. Kennes, and M. A. Sentef, *Cavity quantum materials*, Applied Physics Reviews **9**, 011312 (2022).

[Shi17] K. Shih, P. Pitchappa, M. Manjappa, C. P. Ho, R. Singh, B. Yang, N. Singh, and C. Lee, *Active MEMS metamaterials for THz bandwidth control*, Applied Physics Letters **110**, 161108 (2017).

[Shr11] D. Shrekenhamer, S. Rout, A. C. Strikwerda, C. Bingham, R. D. Averitt, S. Sonkusale, and W. J. Padilla, *High speed terahertz modulation from metamaterials with embedded high electron mobility transistors*, Optics express **19**, 9968–9975 (2011).

[Sin12] R. Singh, J. Xiong, A. K. Azad, H. Yang, S. A. Trugman, Q. X. Jia, A. J. Taylor, and H.-T. Chen, *Optical tuning and ultrafast dynamics of high-temperature superconducting terahertz metamaterials*, Nanophotonics **1**, 117–123 (2012).

[Ste67] F. Stern, *Polarizability of a Two-Dimensional Electron Gas*, Physical Review Letters **18**, 546–548 (1967).

[Ste03] A. G. Stepanov, J. Hebling, and J. Kuhl, *Efficient generation of subpicosecond terahertz radiation by phase-matched optical rectification using ultrashort laser pulses with tilted pulse fronts*, Applied Physics Letters **83**, 3000 (2003).

[Str39] J. A. Stratton and L. J. Chu, *Diffraction Theory of Electromagnetic Waves*, Physical Review **56**, 99–107 (1939).

[Sun15] N. M. Sundaresan, Y. Liu, D. Sadri, L. J. Szőcs, D. L. Underwood, M. Malekakhlagh, H. E. Türeci, and A. A. Houck, *Beyond Strong Coupling in a Multimode Cavity*, Physical Review X **5**, 021035 (2015).

[Tav68] M. Tavis and F. W. Cummings, *Exact Solution for an N-Molecule—Radiation-Field Hamiltonian*, Physical Review **170**, 379–384 (1968).

[Tho19] A. Thomas, L. Lethuillier-Karl, K. Nagarajan, R. M. A. Vergauwe, J. George, T. Chervy, A. Shalabney, E. Devaux, C. Genet, J. Moran, and T. W. Ebbesen, *Tilting a ground-state reactivity landscape by vibrational strong coupling*, Science (New York, N.Y.) **363**, 615–619 (2019).

[Tod10] Y. Todorov, A. M. Andrews, R. Colombelli, S. De Liberato, C. Ciuti, P. Klang, G. Strasser, and C. Sirtori, *Ultrastrong Light-Matter Coupling Regime with Polariton Dots*, Physical Review Letters **105**, 196402 (2010).

[Tod14] Y. Todorov and C. Sirtori, *Few-Electron Ultrastrong Light-Matter Coupling in a Quantum LC Circuit*, Physical Review X **4**, 041031 (2014).

[Unr76] W. G. Unruh, *Notes on black-hole evaporation*, Physical Review D **14**, 870–892 (1976).

[Val21] F. Valmorra, K. Yoshida, L. C. Contamin, S. Messelot, S. Massabeau, M. R. Delbecq, M. C. Dartiailh, M. M. Desjardins, T. Cubaynes, Z. Leghtas, K. Hirakawa, J. Tignon, S. Dhillon, S. Balibar, J. Mangeney, A. Cottet, and T. Kontos, *Vacuum-field-induced THz transport gap in a carbon nanotube quantum dot*, Nature Communications **12**, 5490 (2021).

[Wan73] Y. K. Wang and F. T. Hioe, *Phase Transition in the Dicke Model of Superradiance*, Physical Review A **7**, 831–836 (1973).

[Wil11] C. M. Wilson, G. Johansson, A. Pourkabirian, M. Simoen, J. R. Johansson, T. Duty, F. Nori, and P. Delsing, *Observation of the dynamical Casimir effect in a superconducting circuit*, Nature **479**, 376–379 (2011).

[Wu95] Q. Wu and X. Zhang, *Free-space electro-optic sampling of terahertz beams*, Applied Physics Letters **67**, 3523–3525 (1995).

[Yos17] F. Yoshihara, T. Fuse, S. Ashhab, K. Kakuyanagi, S. Saito, and K. Semba, *Superconducting qubit–oscillator circuit beyond the ultrastrong-coupling regime*, Nature Physics **13**, 44–47 (2017).

[Yu13] N. Yu, P. Genevet, F. Aieta, M. A. Kats, R. Blanchard, G. Aoust, J.-P. Tetienne, Z. Gaburro, and F. Capasso, *Flat Optics: Controlling Wavefronts With Optical Antenna Metasurfaces*, IEEE Journal of Selected Topics in Quantum Electronics **19**, 4700423–4700423 (2013).

[Zak12] B. Zaks, R. B. Liu, and M. S. Sherwin, *Experimental observation of electron–hole recollisions*, Nature **483**, 580–583 (2012).

[Zaw94] W. Zawadzki, C. Chaubet, D. Dur, W. Knap, and A. Raymond, *Cyclotron emission study of electron masses in GaAs-GaAlAs heterostructures*, Semiconductor Science and Technology **9**, 320 (1994).

[Zhu12] W. M. Zhu, A. Q. Liu, T. Bourouina, D. P. Tsai, J. H. Teng, X. H. Zhang, G. Q. Lo, D. L. Kwong, and N. I. Zheludev, *Microelectromechanical Maltese-cross metamaterial with tunable terahertz anisotropy*, Nature Communications **3**, 1274 (2012).

Acknowledgements

This thesis and the work presented herein would not have been possible without the support of numerous people. Here I want to especially thank the following people:

- **Prof. Dr. Rupert Huber**, for being an outstanding supervisor and mentor for the last several years, guiding me through my first steps of my scientific career. I especially want to thank him for his support and advice in all aspects, not limited to improving my presentation, writing and critical thinking skills, the opportunity to share my work at several international conferences with the community, as well as always sharing his passion and curiosity for physics.
- **Prof. Dr. Christoph Lange** for being a phenomenal second supervisor, collaborator, and college. Despite the geographical distances, his consistent engagement has been invaluable. I especially want to thank him for the great guidance, advice and all the countless fruitful discussions. In a special note of appreciation, I want to thank him for taking over paying my salary for the last two years!
- **Prof. Dr. Jaroslav Fabian** and **Prof. Dr. Christian Schüller**, for examining this work as members of the Board of examiners.
- **Prof. Dr. Dominique Bougeard**, **Viola Zeller** and **Michael Prager** for providing all samples, as well as developing the structures in such a close and great collaboration.
- **Dr. Maike Halbhuber**, for being such a great college, in and out of the lab.

- **Prof. Dr. Cristiano Ciuti**, for the fantastic theory support and cooperation.
- **Prof. Dr. Simone De Liberato** and **Dr. Erika Cortese**, for the excellent collaboration and theory development.
- **Laura Diebel**, for mastering the COMSOL simulations and all the fun while sharing an office.
- **Josef Riepl**, for his great companionship in and out of the lab, as well as always having time to help and discuss.
- **Tobias Inzenhofer, Marc Aichner, Ludwig Wittmann** and **Raphael Lehner**, for being great Bachelor/project students, as well as their excellent contributions. It was a pleasure to supervise you.
- **Ulla Franzke**, for all the help whatsoever, bureaucratic, and organisational wise.
- **Martin Furthmeier**, for the constant outstanding technical support.
- **Ignaz Läpple**, for the fantastic electronic designs and support.
- **Imke Gronwald**, for the stellar support and help with e-beam lithography and the chemistry lab.
- **Prof. Dr. Ileana-Cristina Benea-Chelmus** and **Dr. Janine Keller**, for the great collaboration.
- The whole **kHz lab team**, for the excellent working atmosphere and managing to share the precious beam time without fights.
- The whole **Dortmund team**, for the great time working together, even remotely.
- Everyone of the **"Huber Buam*innen"**, for the warm welcome and the fantastic atmosphere all these years. The working environment and the constant support, as well as all the after-work events are what makes this group so special!

- **My family**, for the stellar constant support throughout my whole life and in every situation and in every imaginable way. Without all of you, I would have not made it this far!

extra special thanks go to
Josef Riepl and Filippo Velli
for proofreading this thesis!